5-10-2020

A Serial Multiplexed Approach to Immunolabeling Brain Tissue for Electron Microscopy

Peter Tiley
peter.tiley@uconn.edu

A Serial Multiplexed Approach to Immunolabeling Brain Tissue for Electron Microscopy

Peter Tiley

B.S., University of Connecticut, 2018

A Thesis

Submitted in Partial Fulfillment of the

Requirements for the Degree of

Master of Science

At the

University of Connecticut

2020

2020

APPROVAL PAGE

Masters of Science Thesis

A Serial Multiplexed Approach to Immunolabeling Brain Tissue for Electron Microscopy

Presented by

Peter Tiley, B.S.

Major Advisor_____

Linnaea E. Ostroff

Associate Advisor_____

Alexander C. Jackson

Associate Advisor_____

Joseph J. Loturco

University of Connecticut

2020

Acknowledgements

Committee Members
Dr. Linnaea Ostroff, Ph.D.
Dr. Alexander Jackson, Ph.D.
Dr. Joseph LoTurco, Ph.D.

Ostroff Lab (Current)
Zachary Deane
Janeth Perez-Garza, M.S.
Gianna Raimondi
Jairo Orea
Alison Chase
Ethan Gasteyer

Ostroff Lab (Former)
Justin Woolridge
Valerie Kress

Electron Microscopy Lab
Dr. Maritza Abril, Ph.D.
Dr. Xuanhao Sun, Ph.D.

Advanced Microscopy Facility
Dr. Chris O'Connell, Ph.D.

Institute of Materials Science
Dr. Jasna Jankovic, Ph.D.
Dr. Yuanyuan Zhu, Ph.D.

Funding
The National Institutes of Health

University of Connecticut Department of Physiology and Neurobiology

Table of Contents

Abstract

To fully understand how biological systems give rise to complex phenomena, both structural and functional knowledge of the components in the system must be acquired. In this manuscript, I explain why new methods must be developed to achieve this level of understanding with brain tissue and introduce serial multiplexing as a potential solution. I discuss how this method can lead to highly annotated volume reconstructions of brain tissue using electron and light microscopy, along with the steps required to do so. I present what our lab has found throughout the process of adapting, refining, and combining more traditional methods together to work harmoniously for achieving multiplexed labeling of brain tissue. I also discuss what methods we found to be incompatible and what our advice is for others looking to achieve similar results. I explain why electron microscopy is required to extract ultrastructural information of brain tissue such as synapses, dendritic morphology, and subcellular components. Topics including sample preservation and storage, serial sectioning, grid handling, and immunohistochemistry, among others, are also discussed. To perform immunohistochemistry on brain tissue without compromising its structural integrity in the electron microscope is a considerable challenge. This challenge is magnified when the goal is to label an unrestricted number of target proteins in a sample destined for volume reconstruction, especially considering the lack of a unified roadmap for doing so. We therefore conducted experiments to test the efficacy and reliability of established techniques throughout all processes of obtaining brain tissue for serial multiplexed electron microscopy. We also tested the efficacy and dilution requirements of antibodies across several parameters, targeting candidate proteins and molecules of interest using immunofluorescence microscopy. We draw preliminary conclusions regarding our findings and explore possible directions for the project to continue in the future. The work presented in this manuscript reflects the concerted effort of many individuals over a year and a half and was unfortunately forced to stop prematurely due to a public health crisis beyond our control.

Part 1: Introduction

1.1 Understanding Biological Systems

A fundamental goal of neuroscience is to understand the mechanisms by which the brain processes information and gives rise to subjective experiences. Biology shows that we may begin to understand the purposes of macro-scale structures by studying individual components on the micro-scale in terms of form and function. Several collaborative efforts are currently underway to achieve a better understanding of the brain, each taking a unique approach. Groups such as the Allen Institute are working towards this goal by utilizing single-cell transcriptomics to classify and map brain cells based on gene expression (Regev et al., 2017). Other groups, including the Blue Brain Project, approach this goal by focusing instead on the morphology of brain cells and the tremendous number of connections between them (Markram, 2006; Markram et al., 2015). Other methods include classifying cells based on physiological properties (Buccino et al., 2018). The single-cell transcriptomics approach affords us with rich information about exactly which proteins are expressed in a cell, thereby telling us an individual cell's function. The morphological and synaptic ultrastructure of the brain, on the other hand, allows us to see which cells interact with each other.

Both of these approaches have produced huge amounts of incredibly valuable data and have led to countless breakthroughs in neuroscience. However, they fundamentally different paths that are unable to achieve the information provided by the other. Mapping a human connectome at the ultrastructural level can indeed provide us with a vast understanding of which groups of cells communicate with others but does not provide us with the complete picture. Functional information, such as identification of excitatory or inhibitory neurotransmitters, is totally left out of this picture. This begs the question; what good is knowing the location of a synapse between cells if we are blind to the interactions take place there? The incredible diversity of cell types in the brain shows that there are fine-tuned populations responsible for specific tasks. For a complete understanding, we must combine structural and functional

information together so that we know not just which cells are communicating with each other, but what exactly is being communicated. The current methods discussed thus far cannot provide us with this information at a large enough scale, so new methods must be developed to do so. Fortunately, recent advances are beginning to pave the way for new techniques that may be able to accomplish this feat. The following manuscript explains the process involved in refining a highly scalable approach for combining structural and functional information to better understand biological systems in general and nervous tissue in particular.

1.2 Focusing on the Amygdala

An exciting area of study within neuroscience is the understanding and treatment of the mechanisms responsible for fear and anxiety disorders. To develop new and more effective therapies for these widespread conditions, the structure and function of the cells and circuits that comprise these mechanisms must be understood. At the macro scale, the brain can be divided into morphologically and functionally discrete units in the broader system that each specialize in different functions (Regev et al., 2017; Buccino et al., 2018). In humans and other complex vertebrates, the amygdala has been shown to be one such unit specialized in processing emotional information (LeDoux, 2000; Schafe & LeDoux, 2000; Boatman & Kim, 2006). Within the amygdala, further distinctions and sub-divisions can be made based on similar criteria. The lateral amygdala, abbreviated as LA, has been widely reported to be involved in Pavlovian fear conditioning and fear learning across several model organisms (Rogan et al., 1997; Maren, 2001; Ota et al., 2010; Johansen et al., 2011; Wolff et al., 2014). These are two common methods for assessing anxiety levels at the behavioral level, and they offer us a starting point from which further investigations can be done.

In Pavlovian fear conditioning, a neutral conditioned stimulus (CS) such as an auditory tone is paired with a noxious unconditioned stimulus (US) such as a shock. The subject's behavior is observed

during this process, which can take place over varying durations (Rogan & LeDoux, 1997). During fear recall, the subject's behavior is now observed in response to the CS being presented in the absence of any US. In successful fear learning experiments, the subject displays similar behavioral patterns during the recall stage that it displayed during the conditioning stage, indicating that it made an association between the CS and US (Rogan & LeDoux, 1997). Though a complete understanding remains unknown, we have learned that the LA receives inputs from parts of the thalamus and cortex (LeDoux et al., 1990; LeDoux et al., 1991; Linke et al., 2000; Linke & Schwegler, 2000; Woodson et al., 2000; Boatman & Kim, 2006; Unal et al., 2014). A more straightforward approach to understanding the mechanisms underlying fear and anxiety could be gained by first studying the types of cells in the LA at a finer level of detail.

1.3 Cell Types in the LA

To understand what types of cells are involved in processing negative emotional information in the brain, there must first be a method by which we can classify cells based on common characteristics. Classification based on structural morphology been an early method of accomplishing this ever since the Golgi stain was introduced over one hundred years ago. Further methods utilizing Nissl staining helped provide a clearer understanding of differences between cells based on morphology (McDonald, 1982a; McDonald, 1982b). As a result, distinctions could begin to be made between pyramidal shaped and non-pyramidal shaped neurons in the brain, including in the amygdala. Based on this information, rough subdivisions started to be drawn throughout the amygdala as researchers noted boundaries between homogenous groups of cells. The LA, basolateral amygdala, (BLA), and central amygdala (CeA) emerged among others as structurally discrete units within the amygdala, although naming conventions disagreed for many years (McDonald & Zaric, 2015a). This preliminary mapping of the amygdala provided a contextual framework from which further research could be performed into specific cell types and their locations within sub-regions.

Alongside RNA sequencing, immunohistochemistry (IHC) can be used to distinguish cell types based on the presence of target molecules (McDonald, 1985). IHC can be done using different methods. Some methods utilize an electron microscope (EM) to visualize chromogenic dyes with electrons, or a light microscope (LM) to visualize fluorescent dyes with photons (Roberts et al., 1982; Pelletier et al., 1984; Killingsworth et al., 2012). Using these methods, Alexander McDonald set off a cascade of research by publishing copious studies outlining the distribution of functional cell-type markers in the LA beginning in the late 1980's. Using a using a two-color immunoperoxidase staining procedure, his lab showed that many interneurons expressing γ-aminobutyric acid (GABA) in the BLA co-express a variety of large molecule neuropeptides (McDonald & Pearson, 1989). In this paper, McDonald and Pearson found that most cells expressing somatostatin (SST) and neuropeptide Y (NPY) co-express GABA. They also found that most large cells and about half of the small cells that express cholecystokinin (CCK), along with half of cells expressing vasoactive intestinal peptide (VIP), are also GABAergic (McDonald & Pearson, 1989). In the same year it was shown that SST^+ neurons in the amygdala widely co-express NPY, but not CCK or VIP (McDonald, 1989). Further research confirmed a distinction between SST^+ cells and VIP^+ cells in the BLA based on other functional markers (McDonald & Mascagni, 2002). Though it was not fully understood at the time, it is now widely accepted that GABAergic interneurons play an essential role in mediating fear information processing in the amygdala by modulating neuropeptide release (Kocorowski & Helmstetter, 2001; Chung & Moore, 2009 B; Wolff et al., 2014; Jüngling et al., 2015; Tasan et al., 2016; Krabbe et al., 2018; Rovira-Esteban et al., 2019).

Over the decades, an incomplete but steadily improving knowledge base regarding inhibitory interneurons in the amygdala began taking shape. NPY was shown to be involved in fear behavior processing in rats (Butler et al., 2012), perhaps by having an anxiogenic effect on the BLA (Rostkowski et al., 2009) or the CeA (Wood et al., 2016). In monkey amygdala, it was shown that many neurons in the BLA, some in the CeA, and very few in the LA express NPY (McDonald et al., 1995). This study also showed

that numerous cells in these three regions stained positively for expressing SST and that the number of SST^+ cells always outnumbered the number of NPY^+ cells. It was shown that while the proportion of SST^+ cells co-expressing NPY varied across amygdaloid nuclei, almost all NPY^+ cells co-express SST (McDonald et al., 1995). It was also shown that NPY^+ interneurons in the LA and BLA receive dense serotonergic innervation (Bonn et al., 2013). Most of the published literature compares colocalization of NPY with other neuropeptides such as CCK or calcitonin gene-related peptide (CGRP). CCK has been shown to be anxiolytic in both humans and other animals by facilitating GABAergic transmission via interneurons in the BLA (Chung & Moore, 2007; Chung & Moore, 2009a). CGRP, shown to be involved in nociception (Neugebauer et al., 2020), has been directly implicated in Pavlovian auditory fear conditioning (Kocorowski & Helmstetter, 2001). Additionally, $CGRP^+$ fibers have been shown to innervate the CeA by synapsing onto $GABA^+$ neurons (Yasui et al., 1991; Lu et al., 2015), suggesting a strong role for CGRP in fear and anxiety processing.

Returning to Alexander McDonald's literature, we see that SST is often co-expressed with various calcium binding proteins in addition to the neuropeptides previously discussed. In SST^+ neurons in all nuclei of the BLA, extensive colocalization was found between one of these calcium binding proteins, calbindin (CalB) (McDonald & Mascagni, 2002). In this paper, they also found that SST^+ neurons in the BLA did not co-express calretinin (CalR), nor parvalbumin (PV). Specifically, in the BLA, most SST^+ neurons co-expressed CalB, while in the LA, about two-thirds of SST^+ neurons contained significant levels of CalB labeling (McDonald & Mascagni, 2002). CalB has also been shown to be present in non-pyramidal neurons in all of the sub-nuclei in rat BLA (McDonald, 1997), making it an interesting target to study. Shifting focus to CCK, we know that CCK^+ neurons in the BLA that have large soma and thick dendrites co-express CalB, but not CalR, VIP, or PV (Mascagni & McDonald, 2003). CCK^+ neurons with small soma and thinner dendrites co-express CalR and VIP but do not significantly colocalize with CalB or PV (Mascagni & McDonald, 2003). These studies support the claim that there are distinct subpopulations of neurons

within the amygdala based on co-expression of various neuropeptides and calcium binding proteins, though a complete picture is not yet filled in.

Many cells in the BLA receive inputs from GABAergic projections (McDonald et al., 2011). The primary postsynaptic target cells of SST^+ interneurons in the BLA are cells that express calcium-calmodulin dependent protein kinase II (CamKII), some of which co-express PV (Muller et al., 2007; McDonald & Zaric, 2015a). It was shown that most cells expressing CalR and PV in the BLA of the rat also co-express GABA, but that CalR was not co-expressed with CalB or PV (McDonald & Mascagni, 2001). In the deep amygdaloid nuclei, it has been shown that almost all PV^+ cells, three-fourths of $CalB^+$ cells, and one-fourth of $CalR^+$ cells co-express GABA (Kemppainen & Pitkänen, 2000). Taking a closer look at GABA and its relationship to PV, we see that PV^+ neurons and some $CalR^+$ neurons in the BLA express the α1 subunit of the $GABA_A$ receptor (McDonald & Mascagni, 2004; Równiak et al., 2017). These discoveries, coupled with the findings discussed previously, show that studying the expression patterns of calcium binding proteins in the BLA can provide us with functional distinctions of cells. Though progress has been made, work continues to be made to discover where cells in the BLA send their GABAergic projections to (McDonald & Zaric, 2015b).

1.4 Conventional Limitations

The conventional methods used throughout the literature discussed thus far are limited in the amount of information that can be generated from a given sample. Because only two to three target molecules can often be reliably labeled at a time, the rate of knowledge generation has been limited by the speed at which dual-labeling studies can be published. This is true not only for the light level, but for the EM level as well. A transmission electron microscope (TEM) generates an image of a sample by passing a beam of electrons through the sample and onto a screen or into a camera (Briggman & Bock, 2012). The resulting monochromatic image shows electron-dense and electron-sparse regions throughout the sample as a result of heavier atoms in the sample attracting more electrons. This presents a challenge for

performing IHC, as different labeling patterns need to be distinguished based on structural cues. For instance, a diffuse labeling pattern can be used for identifying marker “A”, while a more crystalline pattern could be used to identify marker “B”. Thus, it is possible to label multiple targets using IHC with TEM and to be confident in the ability to distinguish between them (Meredith & Wouterlood, 1993). However, labeling for more than two targets introduces additional labeling patterns that quickly make distinguishing between them much more difficult to do.

When using LM to conduct IHC, a chromogenic substrates or fluorescent dyes conjugated to secondary antibodies are commonly used (Moreno-Ruiz et al., 2019). Optical visualization of the antibody and by association the target molecule is thereby achieved. However, this method of LM IHC has its limitations as well. The fluorescent dyes are imperfect in that they emit light over a broader spectrum of light than they are designed to, thereby “bleeding” into other wavelengths. If multiple targets are to be labeled, different colored fluorescent antibodies must be used to distinguish different labeling patterns. When imaging, the emitted wavelengths of light from the fluorescent antibodies must be sufficiently different from each other in order to draw any reasonable conclusions, or the labeling patterns will be too similar to tell apart. Additional fluorescent antibodies can be used, but with each new antibody the difficulty to distinguish between them increases. Because of this, the number of targets that can be labeled in each batch of IHC is limited to only a couple at a time.

New approaches are being developed to address the limitations inherent with these methods. It would be immensely powerful to have the ability to label an unrestricted number of targets in a sample as opposed to piecing together bits of information one at a time. Doing so could greatly speed up the rate of knowledge generation regarding not only fear and anxiety in the brain, but in other areas of biology as well. Up until recently, however, doing so has commonly been seen as being too difficult to attempt.

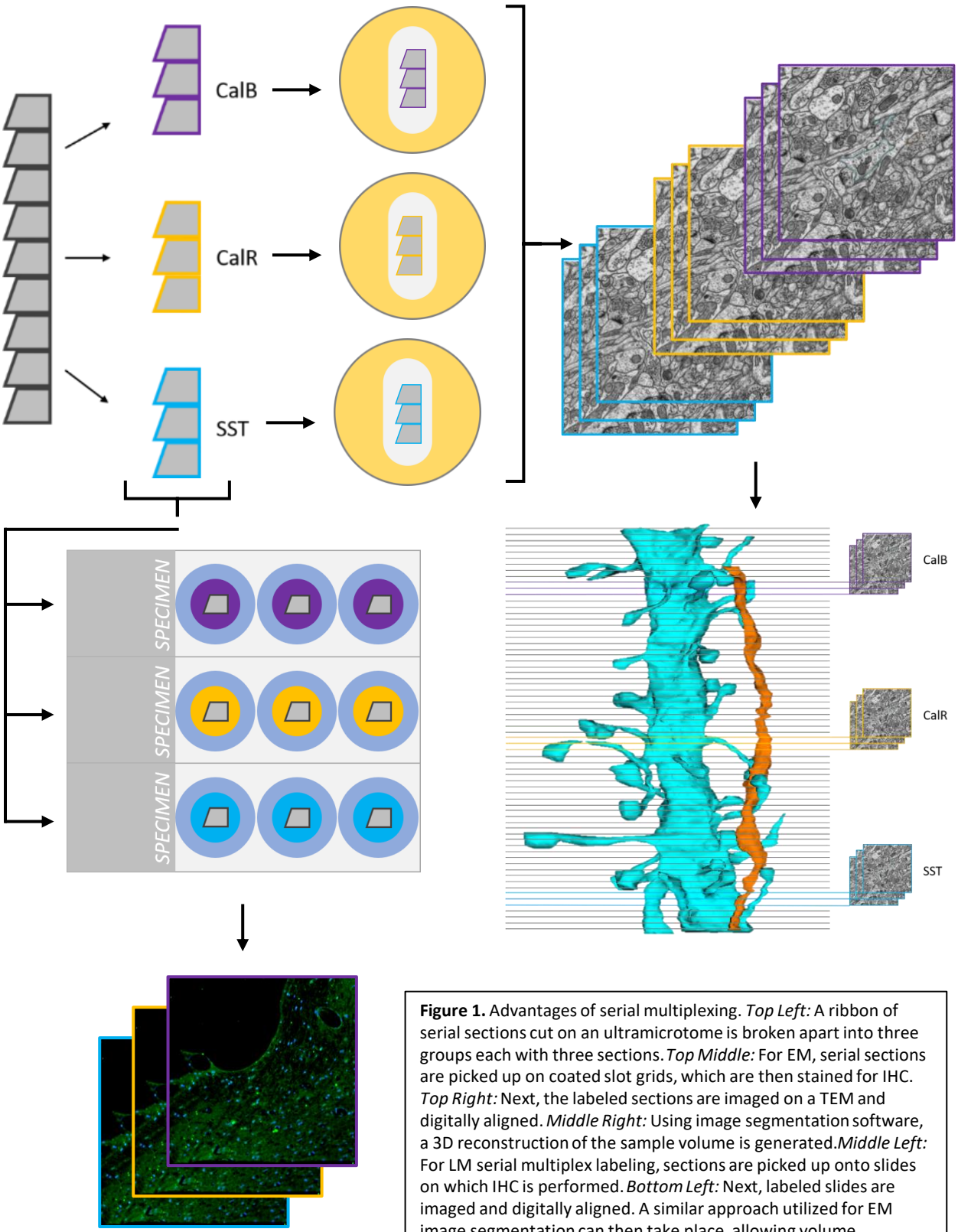

Figure 1. Advantages of serial multiplexing. *Top Left:* A ribbon of serial sections cut on an ultramicrotome is broken apart into three groups each with three sections. *Top Middle:* For EM, serial sections are picked up on coated slot grids, which are then stained for IHC. *Top Right:* Next, the labeled sections are imaged on a TEM and digitally aligned. *Middle Right:* Using image segmentation software, a 3D reconstruction of the sample volume is generated. *Middle Left:* For LM serial multiplex labeling, sections are picked up onto slides on which IHC is performed. *Bottom Left:* Next, labeled slides are imaged and digitally aligned. A similar approach utilized for EM image segmentation can then take place, allowing volume reconstruction of labeled cell bodies.

1.5 A Possible Solution

One possible solution to the limitations discussed in the previous section is the use of serial multiplexed labeling. This entails sub-sectioning a sample into thin sections that are then stained using IHC for different targets (Figure 1). By labeling physical sub-sections of a sample for different markers and overlaying the results, the same structure can be labeled with an arbitrary number of antibodies. Using LM, cell bodies can be labeled for markers and reconstructed in 3D. Using EM, individual axons and dendrites can be labeled and traced throughout neuropil, and the images can be aligned with one another. Serial multiplexed labeling was demonstrated in 2015 when researchers successfully labelled 11 different target proteins on a single biological sample using EM (Shahidi et al., 2015). In this paper, Shahidi et al. were able to section their sample thin enough so that they could align and segment their images, thereby producing a 3D reconstructed volume of their sample. Similar volume reconstruction techniques have been shown to be compatible with brain tissue (Kasthuri et al., 2015). If the methods utilized by Shahidi et al., 2015 can be adapted for use with brain tissue, perhaps we could eventually label every cell in the brain for any number of identifying markers.

In order to perform transmission electron microscopy serial multiplexed labeling of brain tissue, significant sample preparations must be made (Figure 2). Starting with a model organism, the brain must be preserved and extracted without loss of structural and functional information. This entails stopping the degradation of proteins and molecules in the cells, which is a challenge in and of itself. Once the brain is preserved and extracted, it must be stored under specific conditions so that further degradation does not take place. Next, for 3D volume reconstruction using TEM, the sample must be cut extremely thin to be visualized. This entails dehydrating the sample, staining membranes for increased contrast, and embedding in a plastic resin that is then cut using a diamond knife. The sample can then be physically cut into thin sections which must be gently picked up on metal grids without losing them. If more than two sections in a row are lost, it becomes impossible to reliably trace structures across serial sections.

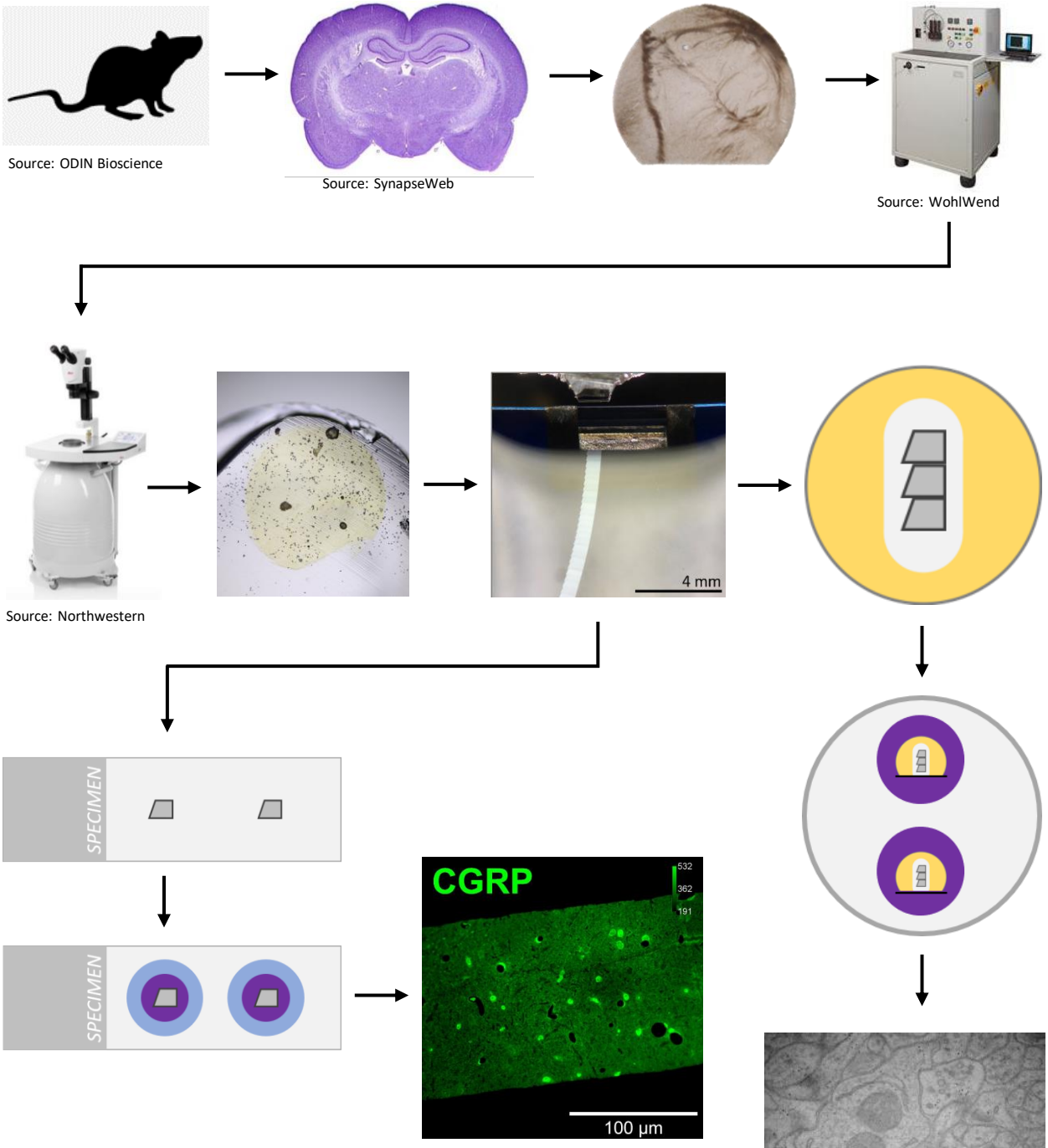

Figure 2. Overview of methods for TEM and LM Imaging of samples. Beginning in the top left; perfusion, brain dissection, post-fixation; brain blocking and vibratome sectioning; ROI micro-dissection; HPF, sample storage; substitution and infiltration; embedding and curing; trimming and ultramicrotome sectioning. To the right; section pickup on coated slot grids; IHC on grids; TEM imaging. Below; section pickup on coated slides; IHC on slides; LM imaging.

There are many protocols for all these steps, each with their own advantages and disadvantages. A commonly made compromise is the tradeoff between high-fidelity morphological and functional information. A strong fixative, such as glutaraldehyde, produces optimal morphological preservation in the TEM, but can occlude some antibody binding sites on some target antigens for IHC (Schwarz & Humbel, 1989). A gentler fixative on the other hand, such as paraformaldehyde (PFA), can preserve these sites, but is too weak to preserve membrane structure to the same degree as glutaraldehyde. Compromises must also be made with regards to embedding media. To visualize something in the TEM, the sample must be between 40 to 250 nm in thickness. To achieve this, the sample must be embedded into a plastic resin and then sectioned on an ultramicrotome using a diamond knife. Methods for embedding samples also vary widely from lab to lab and come with their own advantages and disadvantages. Epoxy resins, such as Epon, can produce some of the best-looking images in the TEM, but are not amenable to rigorous IHC protocols (Schwarz& Humbel, 1989). Acrylic resins, on the other hand, can produce embedded samples that retain much of their immunoreactivity with varying degrees of successful morphological preservation as seen in the TEM.

Given the high degree of variability amongst methods used for electron microscopy, many options exist to perform serial multiplexing. Because this technique has its own unique constraints, only some methods can be used. At present, a combined assessment of protocols does not exist for performing serial multiplexed EM, leaving the path forward unclear. This technique offers so much in terms of potential knowledge generation and is the only feasible way to obtain highly annotated volume reconstructions of brain tissue, making it too important to ignore. In what follows, we discuss what we have learned throughout the process of refining adapting and refining traditional EM methods to work for serial multiplex labeling.

Before beginning the methods testing aspect of this project, we had some hopes for what we could specifically study using this technique. Because our lab is focused on the neurobiology of fear and

anxiety, we found it interesting that we could use serial multiplexing to identify cell type markers impacted by fear conditioning experiments. One specific experiment that we could perform is to assess the distribution of calcium binding proteins CalB, CalR, and PV throughout the LA in a fear conditioned animal compared to a control condition. A plausible hypothesis would be that the levels of these proteins would be increased in the fear conditioned animal. Unfortunately, we ran out of time before we could perform this experiment, but this is something that could be done now that the methods have been worked out. Beginning with preservation and extraction of the brain, we will now shift our focus onto discussing the results from this project.

Part 2: Results

2.1 Fixative Tests

One of the first things to be decided when preparing a sample for immunoelectron microscopy is determining a protocol for tissue preservation. Aldehydes, a group of crosslinking chemical fixatives, historically serve this purpose well. The most used aldehyde fixatives in histology are formaldehyde and paraformaldehyde (PFA), which serve as protein crosslinking agents (Schwarz & Humbel, 1989). While having good tissue penetration, PFA fixes tissue in a manner that can be reversed by thoroughly rinsing the sample with water. Another popular aldehyde fixative is glutaraldehyde, which has a slower rate of penetration than PFA but results in an irreversible crosslinking fix. The larger molecular structure of glutaraldehyde along with dual aldehyde groups on either end of the molecule allow it to bind further apart molecules together (Schwarz & Humbel, 1989). PFA and glutaraldehyde are not mutually exclusive, however, and can be combined in different proportions. Other non-aldehyde fixatives exist, including osmium tetroxide which can be used to fix membranes and provide contrast (Pease & Porter, 1981). Unfortunately, due to its volatile nature, osmium is quite dangerous to work with.

PFA and glutaraldehyde have their own advantages and disadvantages. Because PFA is a reversible fixative and is gentler than glutaraldehyde, it is the better choice of the two for the purposes of performing IHC. During IHC, target proteins that are to be labeled with primary antibodies must have their binding sites available for the antibodies to bind to. The weaker fixation of PFA allows primary antibodies to easily work their way through the crosslinked protein matrix to the target proteins and their binding sites. The stronger fixation of glutaraldehyde, on the other hand, can often produce a matrix of crosslinked proteins and molecules so dense that it impairs the ability of primary antibodies to find and bind to their target proteins (Schwarz & Humbel, 1989). This is especially evident when seeking to label neuropeptides, which are frequently packaged inside large dense-core vesicles shuttled down the axon from the cell body. The added membranous layer of the dense-core vesicle provides a further barrier between the target proteins for IHC and the primary antibodies, making them inherently harder to label than smaller molecules and proteins not found within these vesicles. Thus, in terms of performing IHC, PFA appears to be the superior fixative over glutaraldehyde.

However, this distinction is premature when dealing within the context of electron microscopy. Since our goal is to be able to resolve the fine ultrastructural information of a sample of brain tissue, we must be able to clearly distinguish cell membranes to resolve cellular boundaries. To this end, a fixative for EM must be able to preserve morphological information to distinguish boundaries between cells. Using PFA alone results in subpar preservation of morphology and produces results that cannot reliably be used to determine intercellular connections. The stronger fixation of glutaraldehyde, on the other hand, produces some of the best-looking EM images and retains cellular morphology to a great extent. Thus, for EM IHC, some combination of PFA and glutaraldehyde should be used to strike a balance between preservation of morphological and immunoreactive properties of the sample. Antigen retrieval methods exist, with the goal of rescuing the ability of a target protein to be recognized by a primary antibody (Brorson, 1998; Yamashita & Okada, 2014), but these methods often come with their own disadvantages.

Though we did explore some antigen retrieval techniques, we were not able to produce reliable results and instead shifted our focus towards finding the best possible fixative for EM IHC.

The methods for preserving samples using these fixatives varies depending on the size of the sample being fixed. For small tissue samples, it is sufficient to simply place the sample in the fix and let the fix penetrate the tissue from the outside-in. For fixing brain tissue in vertebrates, however, this method is insufficient as the fixatives are unable to penetrate deep enough inside the sample. Instead, animals are transcardially perfused with the fixative, which distributes the fix throughout their own vasculature. This results in widespread distribution of the fix throughout the animal's body, allowing the fix to pass through capillary beds and achieve a level of penetration otherwise impossible. Because we are dealing with rat brain tissue, we used the perfusion method of fixation to obtain our samples for IHC and imaging.

Total Number of Samples (n=322)	PFA (n=22)	4% PFA in 0.1M Cacodylate buffer with 2mM CaCl2 & 4mM MgCl2 (n=22)
	Glutaraldehyde (n=107)	0.1% glutaraldehyde/4% PFA 0.1M PB (n=18)
		0.1% glutaraldehyde/4% PFA 0.1M PIPES (n=16)
		2.5% glutaraldehyde/4% PFA 0.1M PB (n=15)
		2.5% glutaraldehyde/4% PFA 0.1M PIPES (n=16)
		2.5% glutaraldehyde/ 4% PFA in 0.1M Cacodylate buffer with 2mM CaCl2 & 4mM MgCl2 (n=42)
	Picric Acid (n=14)	0.2% picric acid/0.5% glutaraldehyde/4% PFA 0.1M PB (n=14)
	Acrolein (n=139)	3.8% acrolein/2% PFA 0.1M PB (n=8)
		3.8% acrolein/2% PFA 0.1M PIPES with 2mM CaCl2 & 4mM MgCl2 (50mL), 2% PFA 0.1M PIPES with 2mM CaCl2 & 4mM MgCl2 (250mL) (n=89)
		1.0% acrolein/0.5% glutaraldehyde/4% PFA (n=42)
	PLP (n=8)	2% lysine/0.37% PFA/0.3% sodium periodate (n=8)
	DMS (n=16)	0.5% Dimethyl suberimidate/4% PFA in 0.1M PB (n=16)
	PBQ (n=16)	Saturated (<1%) Parabenzoquinone/4% PFA in 0.1M PB (n=16)

Table 1. Breakdown of fixatives tested. The total number of samples generated from the fixative tests (n=322) can be broken down into five categories of fix, as shown in column 2. Some of these categories had several variations tested, as shown in column 3.

Though PFA and glutaraldehyde are two of the most commonly used fixatives in histology and for EM, a wide array of more exotic and less traditional methods have been cited in the literature (Roholl et al., 1981; Bu'Lock et al., 1982; Somogyi & Takagi, 1982; Hopwood, 1985; Pieri et al., 2002). However, no large-scale comparison between fixatives in terms of morphology and immunoreactivity has been performed, resulting in an incomplete understanding of the advantages of non-traditional fixatives when compared to the more commonly used protocols. We sought to systematically test as many fixatives as we could, and to assess each one against a benchmark standard of glutaraldehyde and PFA (Table 1). A partial sample of our results can be seen in Figure 3. Please note that due to the timing of this manuscript amidst the COVID-19 pandemic and the resulting University of Connecticut shutdown, we are unable to present all of our results. Figure 3 *A* – *D* shows TEM images of PFA fixed tissue with and without glutaraldehyde. After obtaining these reference images, we acquired a new batch of tissue perfused with acrolein, as this has been shown to be a promising fixative in the past (Hopwood, 1985). We then moved on to fixatives including picric acid and dimethylsuberimidate (DMS) (Figure 4). A mixture of sodium periodate, lysine, and periodic acid (PLP) was also tested (Figure 4).

The fixatives discussed thus far were formulated in mixtures of phosphate buffer (PB) to maintain pH balance and osmolarity levels in the brain, and to avoid unnecessary shock that could produce artifacts. However, other buffers exist that we wanted to try out as well. To this end, we tested our benchmark fixative mixture of glutaraldehyde and PFA in cacodylate buffer to see any changes. Due to regulations regarding the waste disposal of cacodylate buffer, we returned to testing different fixatives in traditional PB. Having noticed some promising preliminary results from our acrolein test, we tested this again and now added a small amount of glutaraldehyde to the mixture. Next, we tested parabenzoquinone (PBQ) in PFA and PB (Figure 5) and compared this to fixation with PFA alone. Lastly, based on the results from the first PBQ test, we added a low concentration of glutaraldehyde alongside PBQ and PFA in PB. Clearly, some fixatives work better than others at preserving the structure of brain tissue.

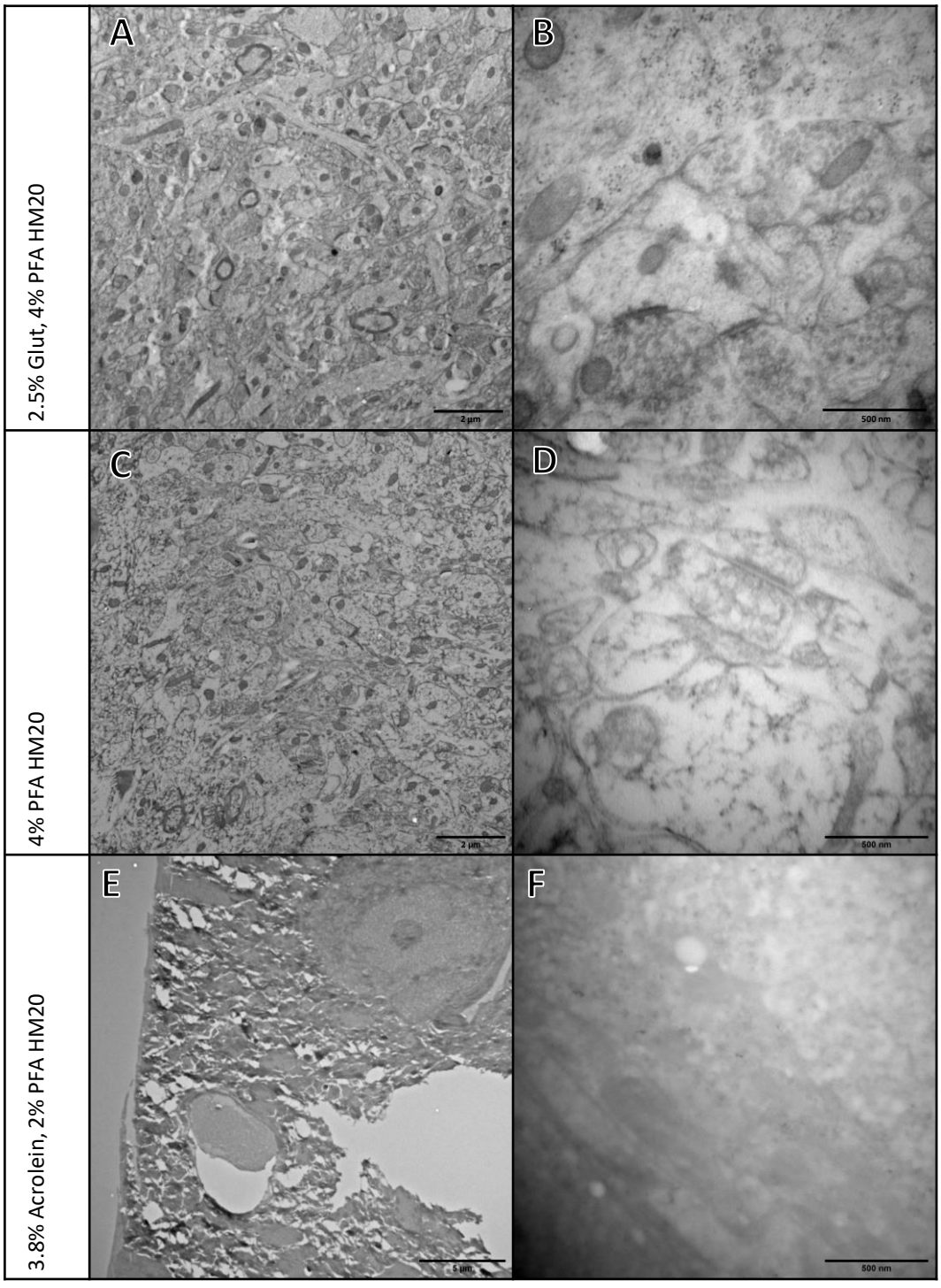

Figure 3. *A:* Low magnification TEM image of tissue fixed with 2.5% Glut and 4% PFA in HM20. *B:* High magnification TEM image of tissue from *A*. *C:* Low magnification TEM image of tissue fixed with 4% PFA in HM20. *D:* High magnification TEM image of tissue from *C*. *E:* Low magnification TEM image of tissue fixed with 3.8% acrolein and 2% PFA in HM20. *F:* High magnification TEM image of tissue from *E*.

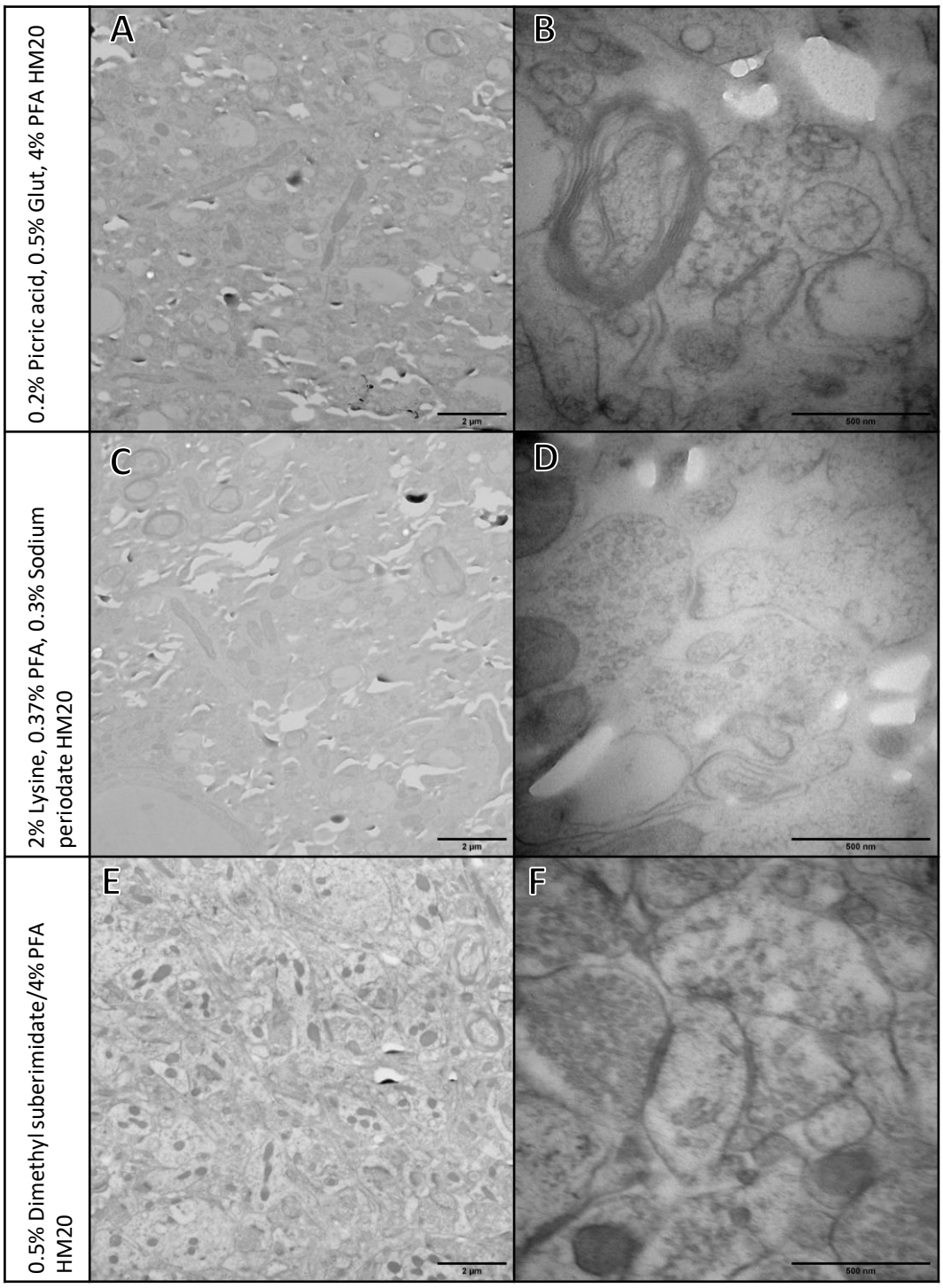

Figure 4. *A:* Low magnification TEM image of tissue fixed with 0.2% picric acid, 0.5% glutaraldehyde, and 4% PFA in HM20. *B:* High magnification TEM image of tissue from *A*. *C:* Low magnification TEM image of tissue fixed with 2% Lysine, 0.37% PFA, and 0.3% sodium periodate in HM20. *D:* High magnification TEM image of tissue from *C*. *E:* Low magnification TEM image of tissue fixed with 0.5% dimethyl suberimidate and 4% PFA in HM20. *F:* High magnification TEM image of tissue from *E*.

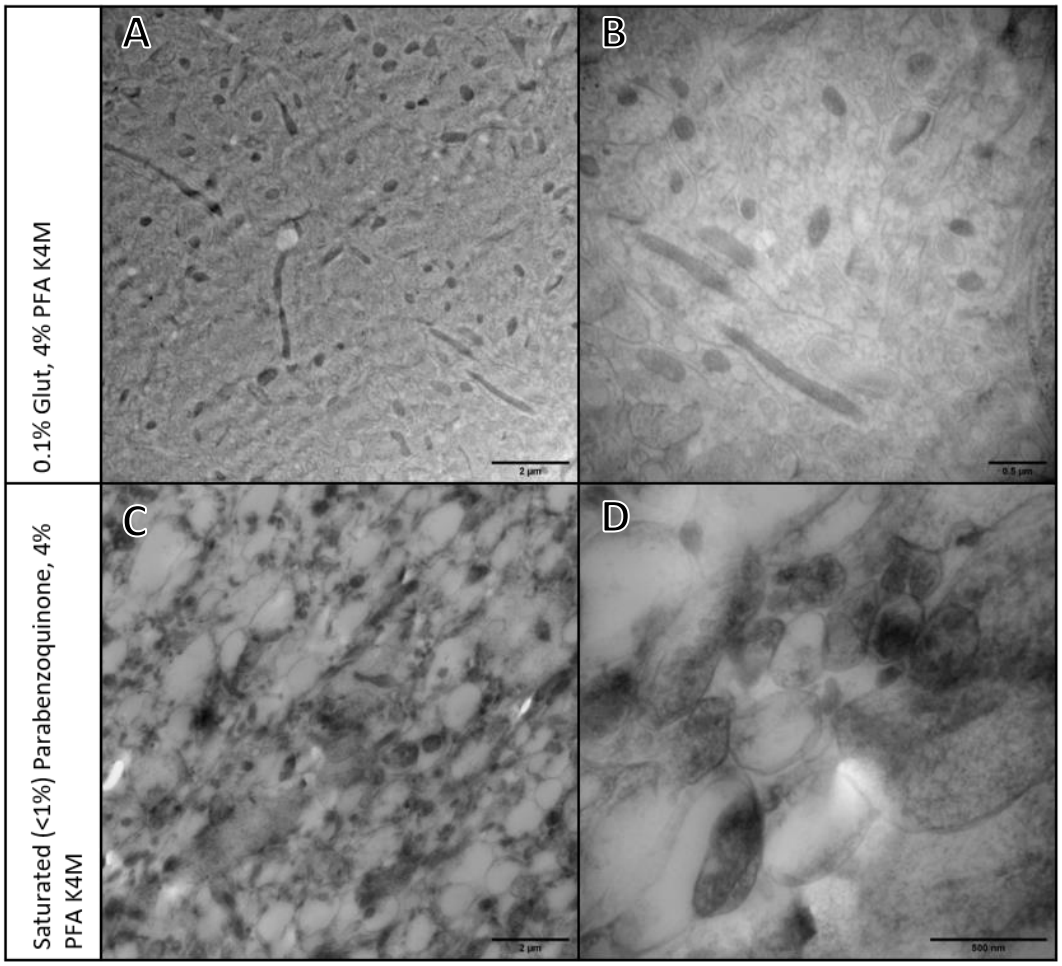

Figure 5. *A:* Low magnification TEM image of tissue fixed with 0.1% glutaraldehyde and 4% PFA in K4M. *B:* High magnification TEM image of tissue from *A*. *C:* Low magnification TEM image of tissue fixed with saturated (<1%) parabenzoquinone and 4% PFA in K4M. *D:* High magnification TEM image of tissue from *C*. Note that images of K11M-embedded tissue could not be imaged in time.

2.2 High-Pressure Freezing

Alongside testing a series of fixatives for this project, we tested several different High-Pressure Freezing (HPF) conditions. After preservation and extraction of the brain, the samples must be stored under strict conditions to prevent degradation. HPF offers a compelling solution for sample storage that has been used for TEM (McDonald, 1999; McDonald et al., 2010; Hess et al., 2018). During HPF, high pressure and with cryogenic temperatures rapidly freeze a sample of tissue, immediately stopping sample degradation (Steinbrecht, 1993; Thijssen et al., 1998; Wild et al., 2001; Buser & Walther, 2008). All our samples were preserved using HPF so that we could store them until we were ready to use them later.

The rapid freezing of the sample during HPF vitrifies water molecules into a solid but non-crystalline state. The molecules are thus frozen in place but are unable to form damaging ice crystals that puncture cell membranes and produce unusable results.

Prior to HPF, regions of interest are dissected from vibratome sections using a biopsy punch. After reference images are taken, this circular disk of tissue is then placed into a shallow metal "hat" that holds it in place inside the HPF machine. A second, flat hat is placed on top of the sample, thereby sandwiching the tissue in between. To orient our samples for further processing steps discussed later, we used a scalpel blade to cut a notch out of each sample prior to HPF. This resulted in some volume being empty and unfilled by tissue in between the two hats. Because this orientation notching procedure is a common protocol for HPF (Thijssen et al., 1998), a variety of solutions exist to fill the excess volume before freezing. At the beginning of the project, we found that many of our samples were breaking apart at some point during HPF. To test possible solutions for this, we added a coating of hydrocarbons to the insides of the hats. We started by using isooctane, which made removing the hats from each other in the post-HPF liquid nitrogen (LN_2) bath much easier than before. However, we found that samples frozen with isooctane were much more difficult to remove from the bottom hat during later processing stages.

After discovering the downsides of using isooctane for HPF, we switched to using hexadecene. Hexadecene made working with the samples during later processing stages much easier than isooctane, and we were able to safely process more samples with this adjusted method. However, hexadecene does have a downside. For an unknown reason, freezing with hexadecene makes the hats much more difficult to separate from one another in the post-HPF LN_2 bath as compared to isooctane or no filler at all. We found that this could be worked around by applying more pressure onto the top hat in the bath to force them to separate although precautions must be made in order to do this safely and to avoid damaging the sample. In addition to the hydrocarbon fillers discussed thus far, many other types of fillers can be used during HPF. We started off by using BSA as the primary filler for our samples, but this resulted in a

crust of BSA surrounding the sample under some conditions. To fix this, we tested a variety of different fillers to find the best one for our purposes. Out of BSA, Ficoll, and PVP, Ficoll performed worse than BSA and PVP performed much better. We found that by using PVP, we did not need to use any hexadecene, which streamlined our workflow considerably.

During these experiments, we learned a lot about LN_2 tanks and sample storage post-HPF. We discovered that some of the tanks we were provided with were defective in that they produced a loud clanging noise when used for HPF which would sometimes produce inadequately frozen samples. Despite contacting our supplier many times about this, they refused to acknowledge the problem. However, after some time, we noticed that we stopped receiving defective tanks. We suspect that there may have been a manufacturing issue that was sorted out that our supplier was either unaware of or did not want to acknowledge.

After HPF, samples are transferred to LN_2 where they remain until they are ready to be used later. We tested a variety of methods for post-HPF sample storage in order to find what works best for us. To save space, we stored two samples in each cryotube for most of this experiment, under the notion that we would be able to distinguish the samples from one another by referencing images taken prior to HPF. However, this turned out to be much harder than anticipated. Since many of the samples were breaking apart at various points throughout our tissue processing protocols, it became too difficult to reliably distinguish between the two samples in each cryotube. For other labs looking to build upon these protocols, we suggest storing only one sample in each tube so that the samples can be reliably traced throughout all steps of the post-HPF process.

Along the way, we also learned that reducing the volume inside the cryotubes helps with sample storage in LN_2 dewars. With less volume for the sample to move around in during storage, the number of samples that break during this time can be reduced. In addition to this preventative measure, we started adding organic solvents (acetone or ethanol) to the cryotubes prior to transferring in the sample. After

freezing the solvent in the cryotube using LN_2, the frozen sample is placed on top and then sealed with the cryotube cap. This protocol creates an even smaller volume in the tube for the sample to move around in during storage, as the frozen solvent does not leak out. An additional benefit of this is that further processing steps require the sample to be in contact with an organic solvent, so storing them in this manner removes one step in the protocol later.

2.3 Cryo-substitution

Once the samples have gone through HPF and are ready to be taken out of storage, delicate precautions must be in place. Because the water molecules have been vitrified in place by HPF, taking the samples out of LN_2 and raising the temperature will cause the molecules to form ice crystals which damage the sample (Schwarz & Humbel, 1989; Steinbrecht, 1993). The first step for post-HPF sample processing is thus to dehydrate the tissue of water molecules and to replace them with a different substance. This process, known as substitution, must be done at a temperature low enough to prevent ice crystal formation (Steinbrecht, 1993). To do this, we used an automatic freeze substitution unit (AFS) to control the temperate of the sample throughout this process. Two commonly used substitution media are the organic solvents acetone and ethanol (Schwarz & Humbel, 1989; Thijssen et al., 1998; Wild et al., 2001; Giddings, 2003). These perform well to replace water molecules in the tissue, thereby allowing the temperature of the sample to be slowly increased.

During substitution, additional compounds can be added to the acetone or ethanol to increase membrane contrast. Two commonly used agents for this purpose are uranyl acetate (UA) and tannic acid (TA) (Schwarz & Humbel, 1989; Walther & Ziegler, 2002; Giddings, 2003; Jiménez et al., 2009). UA is a radioactive, heavy metal salt that can be dissolved in acetone, ethanol, or water. The heavy metals in UA stick to membranes in the sample, adding contrast in the EM by capturing more electrons (McDonald, 2011). TA is a non-radioactive, weakly acidic polyphenol that also serves to increase membrane contrast

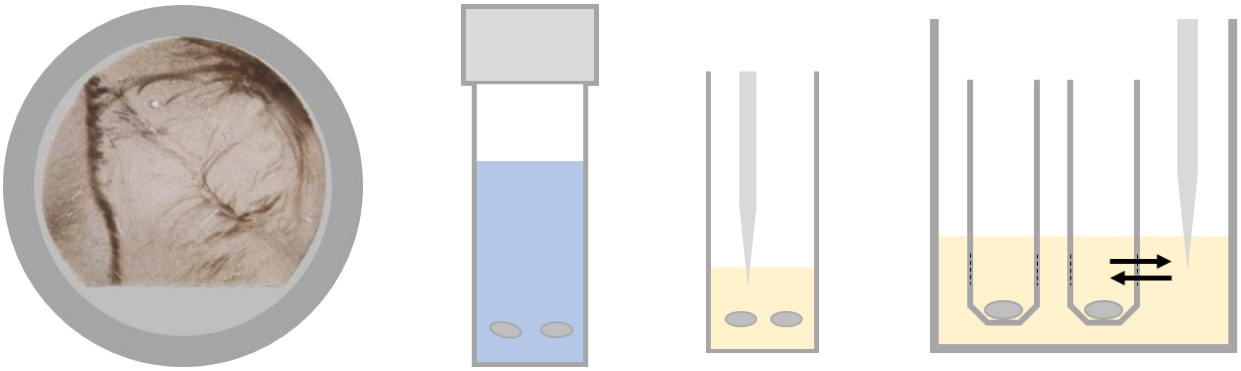

Figure 6. *Far Left:* Diagram showing positioning of micro-dissected ROI from vibratome section in bottom metal hat prior to HPF. Notch allows for orientation of the sample in the embedding stage later on. *Center Left:* Storage protocol for most of the project. Two hats are stored in each cryotube filled with LN2 in blue. *Center Right:* Cryotube substitution method. User pipets in solutions directly into the cryotube holding the samples. *Far Right:* Flow through tube substitution method. User pipets in solution into a dish which contains the flow through tubes. Solution is able to enter the tubes via perforations in the tubes slightly above the resting position of the hat.

in brain tissue (Jiménez et al., 2009). UA can produce more robust membrane staining than TA but can also precipitate out of its solution if particular care is not taken during the substitution process. TA, on the other hand, is gentler than UA and is easier to dispose of given the current regulatory climate. We wanted to determine the optimal substitution protocols for our project, so we tested several different conditions.

Several different methods exist for substituting a sample in the AFS, but they all require the substitution media to come into contact with the sample by using a pipet (Figure 6). The first method we tried was using flow-through tubes. With this method, several porous tubes each containing one sample are placed in an aluminum dish. The substitution media is introduced and removed from the dish itself and is able to enter and exit the tubes. This allows the user to have less physical contact with the sample, thereby decreasing the probability the sample will inadvertently break due to mechanical stress. Since many substitution protocols take place at cryogenic temperatures, the tissue is extremely brittle and the slightest tap of a pipet could fracture the sample. Using flow-through tubes has its downsides, however. Notably, the tissue sits in a recessed portion of the tube underneath the holes in the tube. This can result in poor substitution, as the tissue receives most of the fluid exchange only on one side. This can be

mitigated by lightly agitating the flow-through tube dish in the AFS, but this sometimes results in the tissue breaking apart due to mechanical stress.

The other main substitution method we tested used cryotubes in place of flow-through tubes. Doing so has the clear benefit of not having to transfer the sample from its storage cryotube to a different tube, which decreases the amount of stress the sample undergoes. However, this method has some downsides. Since there are no holes in cryotubes unlike flow-through tubes, substitution media must be introduced and removed via pipet directly into the cryotube (Figure 6). The currents generated by this fluid exchange tend to displace the sample and create an opaque fluid if any precipitates exist, making it hard to see what is going on. One advantage of this is that the tissue is exposed to fluid exchange on all sides, but the disadvantage is that the tissue has a higher chance of being broken apart by mechanical stresses. Since neither of these two methods were perfect, we combined the two to create a reasonable compromise.

We introduced a third method of sample handling in the AFS for substitution by using porous baskets in an aluminum dish. This method allows the user to place their pipet outside of the baskets but inside the dish in a similar fashion to flow-through tubes, reducing contact between the pipet and the sample. Unlike flow-through tubes, however, the larger size of the baskets used allows the tissue to freely move around in response to currents generated by fluid exchange. This captures the benefits of improved substitution that we found using the cryotube method. The only downside to this method is that the samples must be transferred from their storage cryotubes to the baskets, but we think that this is a small price to pay given our results. Overall, we found this method to produce the most reliable results for us. After dehydration via freeze substitution, it is now safe to bring the sample up to a warmer temperature. Depending on what resin the sample will be embedded in, this temperature will vary drastically as we will now discuss.

2.4 Resins: Infiltration and Embedding

In order to visualize something at high magnifications using TEM, the sample must be thin enough for electrons to easily pass through it. To achieve this with brain tissue, samples are infiltrated and embedded into a plastic resin which is then be sectioned incredibly thin. Protocols for resin infiltration and embedding are quite diverse and there are many different types of resin to choose from (Schwarz & Humbel, 1989; Horowitz & Woodcock, 1992; McDonald, 2014). Epoxy resins, including Epon, Araldite, and Durcupan, can be contrasted with acrylic resins such as HM20, K4M, K11M, LR White (LRW), and Methyl-Butyl methacrylate (MBA). Depending on the goals for the project, different resins may perform better than others. Because epoxy resins are hydrophobic, they are less useful for IHC than acrylic resins which tend to be more hydrophilic (Schwarz & Humbel, 1989; Giddings, 2003). Epon, however, is generally considered to produce some of the best-looking images in the TEM and is one of the easier resins to section on the microtome (Giddings, 2003). What results is an apparent tradeoff between preservation of immunoreactivity and preservation of morphology between epoxy and acrylic resins that has not been fully tested side by side.

For serial multiplex labeling, we therefore want to find the best-looking acrylic resin protocols that maintain reasonable immunoreactivity. We started by obtaining several sets of HM20-embedded samples to obtain a reference point before expanding out into more exotic resins (Figures 3 – 4). Next, we tested K4M (Figure 5) and K11M. We found that K4M and K11M produced softer blocks, which made sectioning them on the microtome much more difficult than HM20. However, we noted that K4M produced some promising IHC results in previous experiments. K4M, K11M, and HM20 are all “lowicryls” – that is, they are acrylic resins that are embedded at low temperatures. Alongside these are the non-lowicryl acrylic resins that we tested, LRW and MBA. These more acidic resins tend to dissolve cellular membranes, so they are less suitable for determining morphological information in the TEM than lowicryls are. However, since they can be infiltrated and embedded more quickly than lowicryls, they are useful for

Resin	Infiltration Method	Curing Method	Imaging Efficacy
HM20	Low temp (-55°C)	Low temp UV (-55°C → 22°C)	EM / LM
K4M	Low temp (-30°C)	Low temp UV (-30°C → 22°C)	EM / LM
K11M	Low temp (-55°C)	Low temp UV (-55°C → 22°C)	EM / LM
LRW	Room temperature (22°C) or microwave (≤ 45°C)	Oven (65°C)	LM
MBA	Room temperature (22°C) or microwave (≤ 45°C)	Low temp UV (4°C → 22°C)	LM

Table 2. Table of protocols used for resin tests.

performing immunofluorescence (IF) imaging. We found that LRW produced highly variable IF results and was more difficult to section on the microtome than the lowicryls. We only recently started testing MBA but found that this resin sectioned much easier on the microtome and shows promising IHC results as we will see later.

One of the ways we tested resins was by experimenting with different infiltration protocols. During infiltration, the organic solvent in the tissue left behind from substitution is replaced with resin using an ascending series of concentrations. Depending on the resin, infiltration temperatures and times can vary (Table 2). For lowicryls, infiltration takes place at cryogenic temperatures using the AFS and takes several hours. For the non-lowicryls, infiltration can be done under different conditions. For both LRW and MBA, we tested infiltrating samples at room temperature (RT) and in a lab microwave. Microwave infiltration takes much less time than RT infiltration, and we did not notice a major difference in quality

between the two conditions. Therefore, we would suggest using a lab microwave to speed up the infiltration procedure for non-lowicryl resins so long as sample quality is not compromised.

We performed infiltration tests for lowicryls using the different setups discussed in §2.2. Infiltration using flow-through tubes proved to be a challenge for us as the thick resins had a difficulty working their way into the tissue via the limited contact area, and we had better results using the cryotube method. We found that infiltration using the basket method allowed for better infiltration conditions while maintaining structural integrity of samples. For LRW and MBA, we tested infiltration using cryotubes and gelatin capsules. Since these were done at warmer temperatures, the issue of the brittle tissue breaking apart was largely mitigated. Overall, we found that using cryotubes produced better results than using gelatin capsules, likely due to the larger volume for fluid exchange.

After resin infiltration, samples undergo embedding and curing steps to solidify them inside a block of hardened resin. Embedding protocols vary based on the resin, so we tested a variety to find what would work best for us (Corcoran & Walker, 1990). Lowicryls are embedded at low temperatures and use UV light to cure the resin into a solid (Table 2). LRW requires heat to cure, so ovens are frequently used (McDonald, 2014). We tried curing LRW blocks using the microwave used for infiltration but did not achieve desirable results. MBA, while being infiltrated in the microwave, can be cured in the AFS using a UV lamp if kept slightly below RT. This is done to keep the resin cool, as the curing process for MBA is an exothermic reaction. Though conceptually similar, the differences in embedding techniques give rise to some interesting challenges.

A final matter to consider regarding resins is the type of embedding mold used during the curing process. The shape of the embedding mold dictates not only the shape of the block but the position of the tissue inside, so it is wise to take this into account prior to embedding. If flow-through tubes are used for substitution and infiltration, a convenient embedding mold can be used that attaches onto these tubes. An advantage of this technique is that the user does not have to move the sample from the

infiltration tube, thereby reducing the amount of physical contact made with the sample. However, we found a couple of disadvantages to embedding samples in flow-through tubes. Namely, we consistently found that using this method produced blocks that were cured to varying degrees. Despite using the same conditions for all blocks in a batch, some blocks would be more polymerized than others, and some batches were completely under-polymerized. We suspect that this could be a result of the UV lamp's position overhead the samples in the AFS chamber. Since the UV rays need to reach all the way to the bottom of the vertically positioned samples, some variability could be introduced.

For lowicryl samples infiltrated in either cryotubes or baskets, other embedding methods can be more useful. Flat-embedding molds are thinner and wider than flow-through tube embedding molds and position the samples closer to the UV lamp. We found that we had the best results for our blocks when we used flat embedding molds, perhaps due to the decreased penetration levels required of the UV rays for full polymerization. However, flat-embedding molds come with some disadvantages. Because the molds cannot attach to either cryotubes or baskets directly, samples must be physically moved their infiltration tubes into the mold, increasing the chances for sample loss due to mechanical stress. Another step required to use flat-embedding molds is to attach an Aclar cover to block out any air from interfering with the curing process. With flow-through tubes, this step is not required as the mold attaches directly to the tubes and does not allow any air in. However, with flat-embedding molds, we found that sometimes the Aclar cover would come loose during the curing process, thereby allowing air to interfere and produce improperly cured blocks.

For LRW and MBA, embedding is a more straightforward process. Gelatin capsules were used for embedding regardless of the infiltration method used. This was convenient for samples already infiltrated in gelatin capsules, as the sample did not need to be transferred to another tube. For infiltration using cryotubes, the samples must be physically transferred from the tubes to the capsules, which as we know is less than ideal. Since embedding must be done in the absence of air, we simply capped each gelatin

capsule with its corresponding top. We found that this worked most of the time, but that in some rare instances air would find its way into the capsules and the blocks would polymerize incompletely. Another problem we encountered using gelatin capsules is that the tissue becomes hard to see when it is inside the capsule. Due to the round shape of the capsule and the sample, we had great difficulty maneuvering the tissue inside the capsule and mostly had to rely on gravity for positioning.

Recently, we started testing a new method for sample orientation involving an additional embedding step. After vibratome sectioning and dissecting out the region of interest, the biopsy punch and the surrounding tissue are imaged using an upright microscope in our lab. Next, the region of interest from a single sample is micro-dissected into several thin strips. This allows us to control exactly which part of the tissue moves on for further processing, as well as results in an increased number of samples. Using methods adapted from McDonald et al., 2010, we then embed the strips of tissue in agarose. Next, the strip of tissue and surrounding agarose is dissected out using a biopsy punch, yielding a disk of agarose-embedded tissue. From here, the disk can be frozen as usual. This method has seemed to work well for us, although it does take more time to do. However, the advantages are that the precise location of interest can be embedded into a single block, removing ambiguity when sectioning and staining for IHC. As we will see in the next section, sample orientation prior to embedding has significant downstream implications.

2.5 Trimming and Sectioning

Once the sample is embedded into a block of resin, the next steps are trimming and sectioning. Prior to sectioning the block on the microtome, hand trimming with a razor blade is done to expose the tissue and to make the sectioning process easier. Depending on the shape of the block, different trimming techniques will be employed (Figure 7). For flat-embedded blocks, trimming is similar to Epon-based protocols with the goal being to remove a large portion of the resin located between the edge of the block

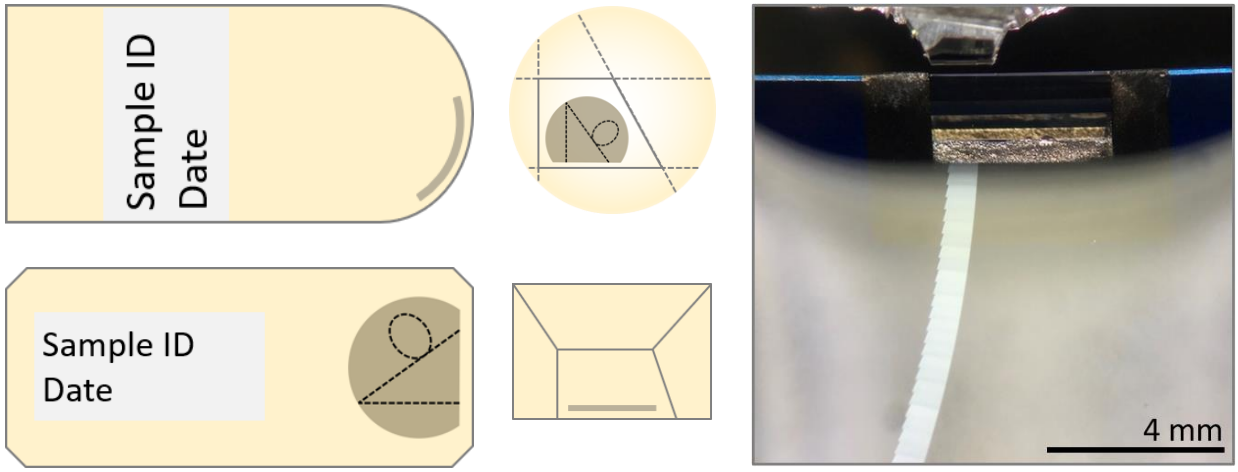

Figure 7. *Top Left:* Capsule-embedded sample viewed from above. Note that in the curing stage, the capsule is oriented vertically which causes the tissue, seen in brown, to rest against the rounded bottom. *Top Middle:* Capsule-embedded sample viewed from the perspective of the microtome knife. Dotted lines represent trimming angles cut prior to sectioning. *Bottom Left:* Flat-embedded sample viewed from above. During the curing stage, the tissue rests against the flat bottom. *Bottom Middle:* Flat-embedded sample viewed from the perspective of the microtome knife. A trapezoid is cut prior to sectioning so that the sections stick together in the boat. *Right:* View of microtome knife and sample with a ribbon of serial sections. The flat-embedded sample, seen at the top of the image, passes over the diamond knife seen directly beneath it. Trapezoidal sections float off of the edge and stick together, forming a slightly curved ribbon.

and the tissue and to create a trapezoid "face". During embedding, the tissue falls to the bottom of the mold but can be positioned by hand to be closer or further from the cutting edge. For flow-through tube and capsule embedded blocks, trimming and sectioning is a little more complicated. Because these blocks are embedded vertically, gravity pulls the tissue right up against the cutting edge of the block. The user must therefore be extremely careful not to accidentally cut through the tissue when hand trimming the block and should focus mostly on creating a flat face for sectioning.

Blocks embedded in flow-through tube molds will already have a mostly flat bottom that the tissue sits against, making the trimming process a straightforward endeavor. Capsule embedded blocks, on the other hand, have rounded bottoms that make trimming much more difficult. Because the tissue conforms to the rounded shape of the capsule, the sample is not positioned in a flat plane that can be easily maneuvered. Instead, we found that the best way to hand trim capsule embedded blocks was to

make a trapezoidal face as if the surface were flat and then carefully trim the face at an angle to produce a flat surface. This process takes some time to do, and there may be better ways to go about this step.

After hand trimming, the block is moved to the ultramicrotome for alignment and rough sectioning. Alignment of the block is critical prior to rough sectioning so that the hand-trimmed face is cut at a proper angle. For IHC, this becomes even more important. Because different areas in a sample can have different labeling patterns, it is important to know exactly where you are looking at in the sample. This proved to be a significant challenge that we did not fully consider when starting this project. After realizing this, we began to develop protocols for block alignment on the microtome. We found that if the tissue was aligned properly in the block prior to embedding, it was easiest to section the entire face of the hand-trimmed block to ensure that we captured the full length of the tissue. This was easy to do using flat embedded blocks but took much more time when using capsule embedded blocks due to their rounded bottoms. This results in the tissue being curved in three dimensions, therefore limiting the practicality of sectioning the full length of tissue each time. We found that tilting the block up and down can, in some instances, result in the full length of the tissue being sectioned. However, since all our samples were produced by HPF, the samples are not very thick and be easily cut through using this method. Because of these drawbacks, we conclude that aligning flat-embedded blocks is much easier and faster to do than aligning capsule-embedded blocks.

To resolve individual synaptic vesicles in brain tissue, the sample must be cut at a thickness of 45 to 50 nanometers. The two primary tools for sectioning are the glass knife and the diamond knife. Glass knives are relatively cheap and can be produced in the lab from specialized glass which makes them quite useful for rough trimming or for users who are not trained on other tools. Diamond knives are much more expensive and cannot be made in the lab, but they allow the trained user to section their blocks incredibly thin and produce better sections. We followed protocols adapted from Electron Microscopy Sciences when sectioning on the microtome by starting off with a glass knife for rough trimming. Rough trimming

with a glass knife produces a much flatter surface than hand trimming does and allows the user to carefully remove more resin to expose the tissue without inadvertently cutting through it. Since it can sometimes be difficult to see the tissue by eye, thick sections are sometimes taken and stained to verify the presence of the tissue. These sections can be anywhere from 100nm to 1µm in thickness and can be stained on slides using Toluidine Blue or Methylene Blue – Azure II. Next, fine trimming and sectioning using the diamond knife can take place.

For hydrophobic resins such as Epon, sectioning with a diamond knife is a relatively straightforward procedure. The highly variable conditions of acrylic resins, on the other hand, introduce several variables that must be accounted for. Parameters such as knife angle, water level, cutting speed, among others must be adjusted to the specific resin being sectioned. Softer resins require different cutting speeds and knife angles than others, and hydrophilic resins require different water levels in the knife boat. We found that the less hydrophilic acrylic resins were much easier to section than the more hydrophilic ones such as K4M and K11M. These tended to draw up water from the boat onto the face of the block during the retraction phase of the microtome, regardless of the water level. As a result, we had to pause the microtome after each pass to wipe off the face of the block with lens tissue paper to dry it off. If this is not done, the block will not cut on the next pass. A negative side effect of this is that sections come off the knife at different thickness levels. Because we must section our blocks at or below 50nm, pausing the microtome in between passes introduces a tiny amount of variability in section thickness. Therefore, we found it extremely difficult to produce reliably thin sections from more hydrophilic resins.

A possible solution to this is to make the block face as small as possible to mitigate the hydrophilic effects, but the face size is limited based on how much of the original tissue will be retained. Additionally, we noticed that as we made the face of the block smaller and smaller, sections would wrinkle up on the edge of the knife and would not cut properly. We suspect that this is due to the softer composition of acrylic resins compared to Epon which did not have this problem. Ultimately, we found that HM20 was

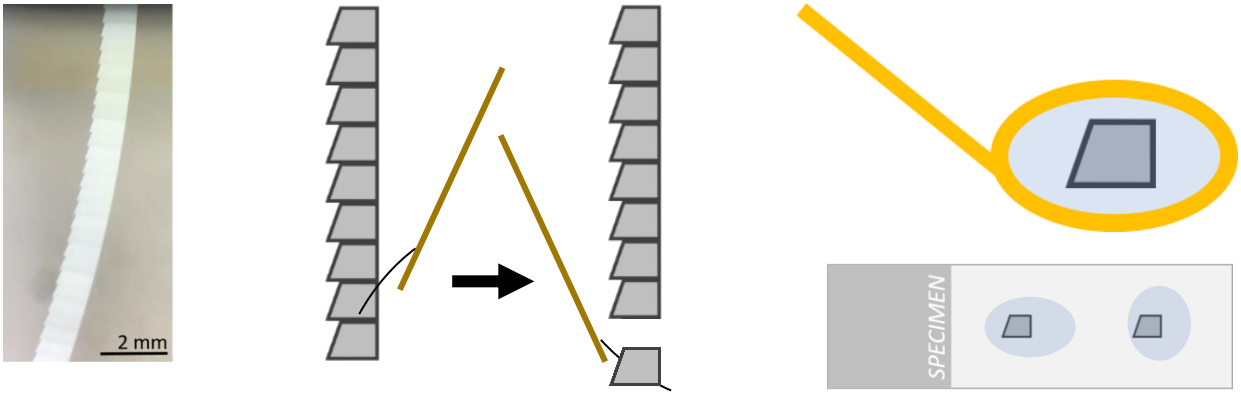

Figure 8. *Far Left:* Close-up view of serial section ribbon in knife boat. *Middle:* Schematic view of serial section ribbon and eyelash tools. After delicately breaking off a section from the ribbon, the eyelash tool can be used to drape the detached section around it in order to transfer to a slide. *Top Right:* Schematic of the perfect loop tool with an attached section. The tool forms a meniscus of water around the section when light pressure is applied to the water surface. The section and a droplet of water are then pulled up into the ring of the tool, where they can then be transferred to a slide. *Bottom Right:* Schematic showing typical distribution of sections on a subbed slide.

the easiest lowicryl to section and produced reliable results, though LRW and MBA behaved better overall. Orientation issues aside, we were able to produce reliably thin sections from LRW blocks, although the resin had a similar yet reduced affinity for becoming wet from the boat. Though we only recently started testing MBA, we found that this was the easiest resin out of all that we tested in terms of sectioning.

Once the block is cutting properly, sections float off the knife edge onto the water in the knife boat (Figure 8). From here, sections must be physically picked up onto grids for EM or transferred to slides for LM. We tested a variety of methods for transferring sections onto slides for slide mounted IHC and for test thick sections. The first method we utilized was to drape a section around an eyelash or cat whisker attached to a thin wooden dowel. This turned out to be robust at transferring sections from the boat onto slides, but had some serious limitations as discussed in §2.8. Upon discovering these disadvantages, we started using what is known as the “perfect loop”. The perfect loop works by drawing up a meniscus of water around a section when placed next to the water. This allows the section to be safely transported in a droplet of water held up by a metal loop, as opposed to being wrapped around itself in the previous

method (Figure 8). However, we found that using the perfect loop came with some time-consuming challenges that needed to be worked out.

First and foremost, the perfect loop requires a hydrophilic surface for the section and the water droplet to successfully detach from the loop. This presented an issue for us since we needed our sections to be located on positively charged "subbed" slides for IHC. This resulted in the droplet and section coming off the loop incompletely or improperly. To manage this, we raised and lowered the loop several times onto the slide, each time removing more and more of the water droplet. In doing so, however, the user introduces more chances for the droplet to burst under mechanical stress, which tends to send to the section flying out of view when this happens. Different sized perfect loops can be used to varying degrees of success, but these are limited by the size of the sections. We tested using a plasma cleaner to make our slides less hydrophobic but were not able to produce reliable results in time. Ultimately, we found that the best method for obtaining sections on slides was to use the perfect loop very carefully to avoid bursting the water droplet.

2.6 Grids and Film Casting

Sections destined for imaging on the TEM need to be picked up on small metal grids directly from the knife boat. To do so, we used metal forceps with one hand to partially submerge a grid, and an eyelash tool in the other hand to gently push the sections onto the grid. We found that the best way to collect serial sections is to use an eyelash tool in each hand to gently break off a small series of the oldest sections from the ribbon and to pick up each smaller series on a grid. If the top section can be gently attached to the partially submerged grid, the rest of the sections will adhere themselves to the grid when the grid is lifted out of the water. Another method for obtaining serial sections on grids is to start from the newest sections on the ribbon as opposed to the oldest. The newest section can be attached to a partially submerged grid which is then lifted out of the water. As the ribbon lifts as well, an eyelash tool can be

used to break the ribbon in the boat, leaving a small series attached to the grid and most of the ribbon left intact on the water. We found that people have different preferences for these two techniques and that both should be tried out.

The type of grid used to pick up sections for EM can vary depending on the goals of the project (Figure 9). Mesh and slot grids are useful in different circumstances and can be manufactured out of a variety of different metals. Mesh grids hold sections by means of an interleaving network of metal. Some mesh grids have more bars than others, allowing the user to decide what type is best for their specific purposes. These grids are straightforward to use and do not require any additional processing to make them functional but have their drawbacks. Since the metal mesh is picked up by the electron beam in the microscope, areas of tissue that are located directly above a mesh bar are not visible. To address this, some grids have a mesh more widely spaced than other. The fewer interruptions in the viewing field allow the user to see more of their sample than finer mesh grids. However, smaller or loosely held sections can fall in between the gaps created by coarser mesh grids, resulting in a tradeoff between section support and visibility.

For serial sectioning, however, mesh grids should not be used. Since there is no way to guarantee that the same field will not be occluded by the mesh on each section, slot grids must instead be used. Slot grids are solid metal grids with a slot cut out of them in the center of each grid and are usually thicker than mesh grids. Slot grids must be coated in a thin film to provide support for the sections to rest on, whereas mesh grids support the sections directly. A huge advantage of using slot grids over mesh grids is that the entire sample can be imaged in the TEM since there are not any metal bars blocking the view. Users who are doing serial section TEM can purchase slot grids pre-coated with formvar or purchase uncoated grids and cast their own films. Formvar acts as the transparent film that covers the slot and works under some conditions. However, for high-magnification imaging of brain tissue, Formvar is not a

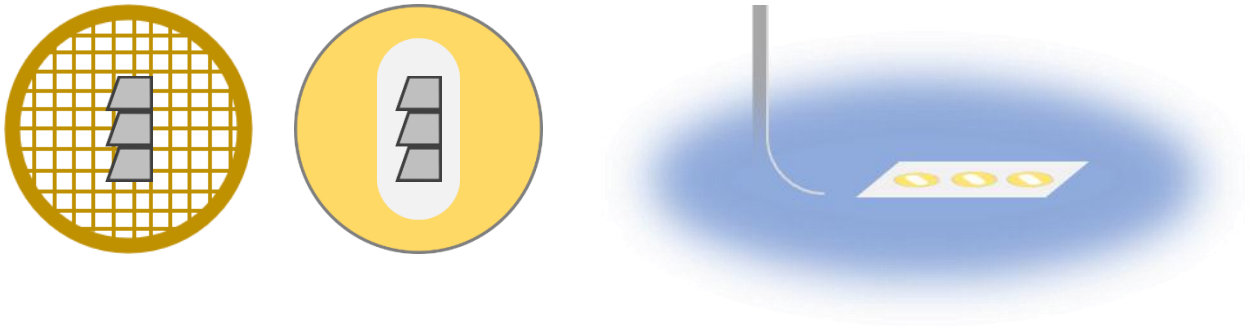

Figure 9. *Left:* A mesh grid with serial sections. Note that the mesh bars provide support for the sections but also make it impossible to image the same field across serial sections. *Middle:* A slot grid with serial sections. A transparent film covering the slot provides support for the sections and allows for serial section imaging. *Right:* Slot grid coating. Thin films (light gray) are cast onto slides (dark gray) which are then scored and submerged into a water bath. The film floats off the slide onto which uncoated slot grids are placed face down. Coated grids are then transferred to a new slide for storage.

viable option due to its subpar imaging quality (Morphew et al., 1998; Kneissler, 2003). Instead of using Formvar, the best-looking images can be taken using grids that were coated in the lab.

We tested two types of films for slot grid coatings: polystyrene and pioloform. For both films, we dissolved the solid reagent into their respective solvents at a 1% dilution, and then used a film caster to coat a glass slide with a film produced by the vapors. Next, the coated slide was scored with a razor blade, and then floated off onto a bath of RO water (Figure 9). From here, uncoated slot grids can be placed onto the floating film and gently tapped to ensure secure contact. The final step is to partially submerge another slide covered in parafilm onto the floating film to adhere the film and grids to the slide. We found that pioloform coated grids were much easier to use than polystyrene coated ones, as polystyrene grids needed to be plasma cleaned prior to section pickup. After many batches of coating grids with pioloform, we noticed that the best results came from films that easily floated off the slide onto the water. For this to happen, the slide that the film is cast on must be incredibly smooth. We found that a particular brand of slides from Fisher Scientific, called “Gold Seal”, produced the best results for us overall. However, some Gold Seal slides produced better films than others, and we were unsure why this was the case.

We began to track the date that we received the slides in the mail and discovered that newer shipments of slides tended to produce better results than older ones. However, this was not a perfect

relationship. We found out that some batches of slides would sit in a warehouse for longer periods of time than others after manufacturing and suspect that this could be the cause of the inconsistency. To resolve this, I spent some time speaking with Fisher Scientific and other vendors of Gold Seal slides to try get as much information as possible regarding the supply chain and manufacturing dates of slides. We found out that the vendors were unfortunately quite reluctant to provide us with the information we were hoping to find. However, we were able to uncover that most of the vendors all source their Gold Seal slides from the same supplier in New Hampshire. Upon calling this company and talking with a representative, I was unable to gather any additional information about the dates of manufacturing and distribution for these slides.

Considering this, we started testing alternative methods for producing the best possible films for our slides. We tested brand new, unopened Gold Seal slides against slides from an older, opened batch and on batches of slides that were kept in a desiccator over varying lengths of time (Figure 10). We also tested plain Fisher Super Frost slides, but these did not produce films that were usable in the TEM. We tried plasma cleaning plain glass slides and Gold Seal slides, using charged slides, pre-cleaning slides using different protocols, and even using silicon wafers instead of glass slides. We visited the glass blowing shop at the University of Connecticut Depot Campus to see if we could learn why the Gold Seal slides seemed to produce the best results and to see if we could recreate them ourselves. Though this turned out to be a dead end, we found that our limited testing of silicon wafers produced some decent films (Figure 10). Ultimately, we decided that there were too many uncontrollable variables for us to be entirely sure about the reasons for our mixed results. We suspect that temperature, humidity, and other factors play an important role in the film casting process and should be controlled for if possible. We settled on using a pioloform film on the newest possible Gold Seal slides that we could acquire, as this produced the most reliable results that we found.

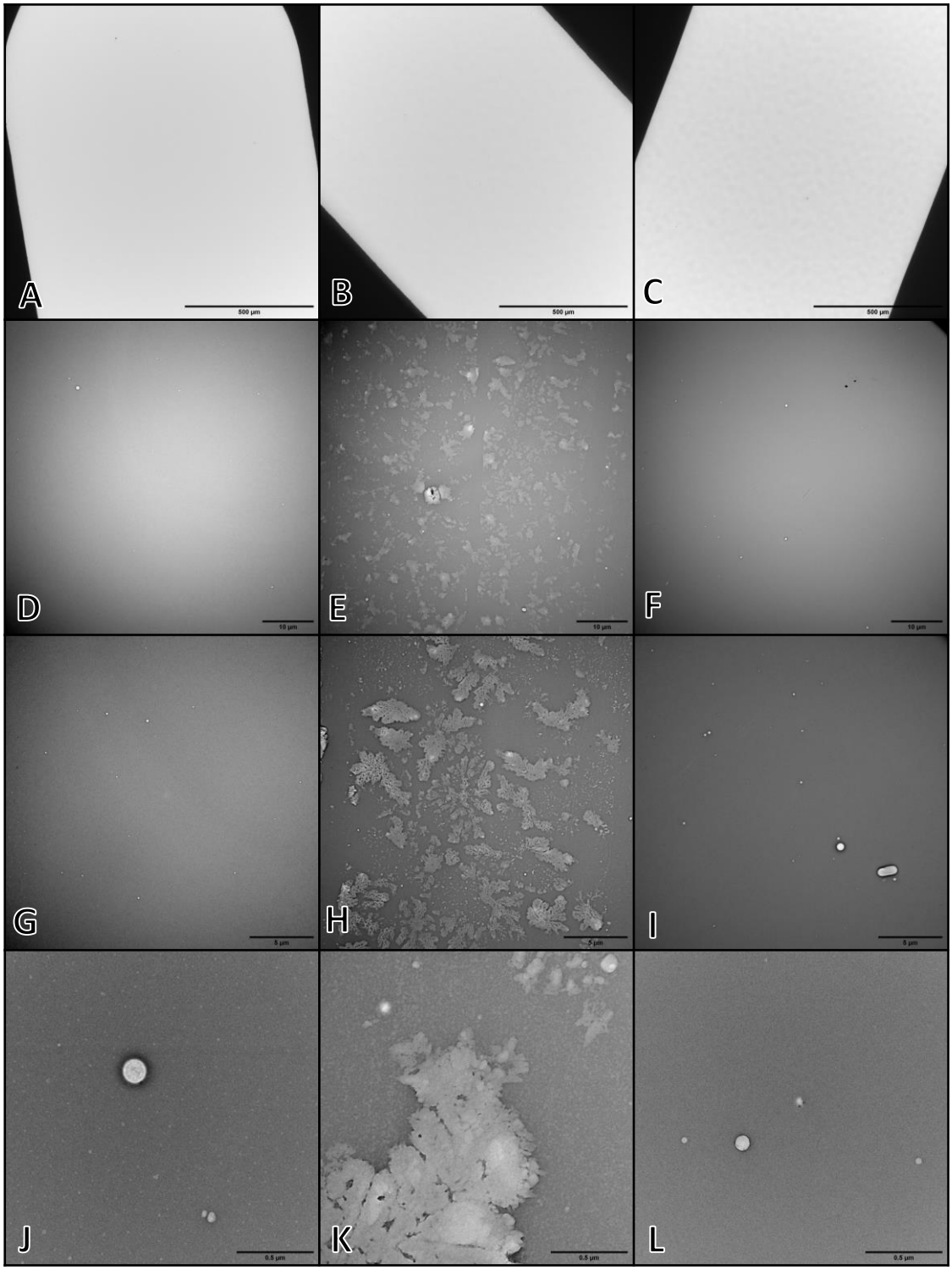

Figure 10. Testing different conditions for pioloform film casting. *A:* 100x TEM image of gold slot grid coated with pioloform cast on new silicon wafers pre-treated with N_2 gas and alconox. *B:* 2000x TEM image of grid from *A*. *C:* 5000x TEM image of grid from *A*. *D:* 50000x image of grid from *A*. *E:* 100x TEM image of gold slot grid coated with pioloform cast on newly opened GoldSeal slides. *F:* 2000x TEM image of grid from *E*. *G:* 5000x TEM image of grid from *E*. *H:* 50000x image of grid from *E*. *I:* 100x TEM image of gold slot grid coated with pioloform cast on a different batch of newly opened GoldSeal slides. *J:* 2000x TEM image of grid from *I*. *K:* 5000x TEM image of grid from *I*. *L:* 50000x image of grid from *I*.

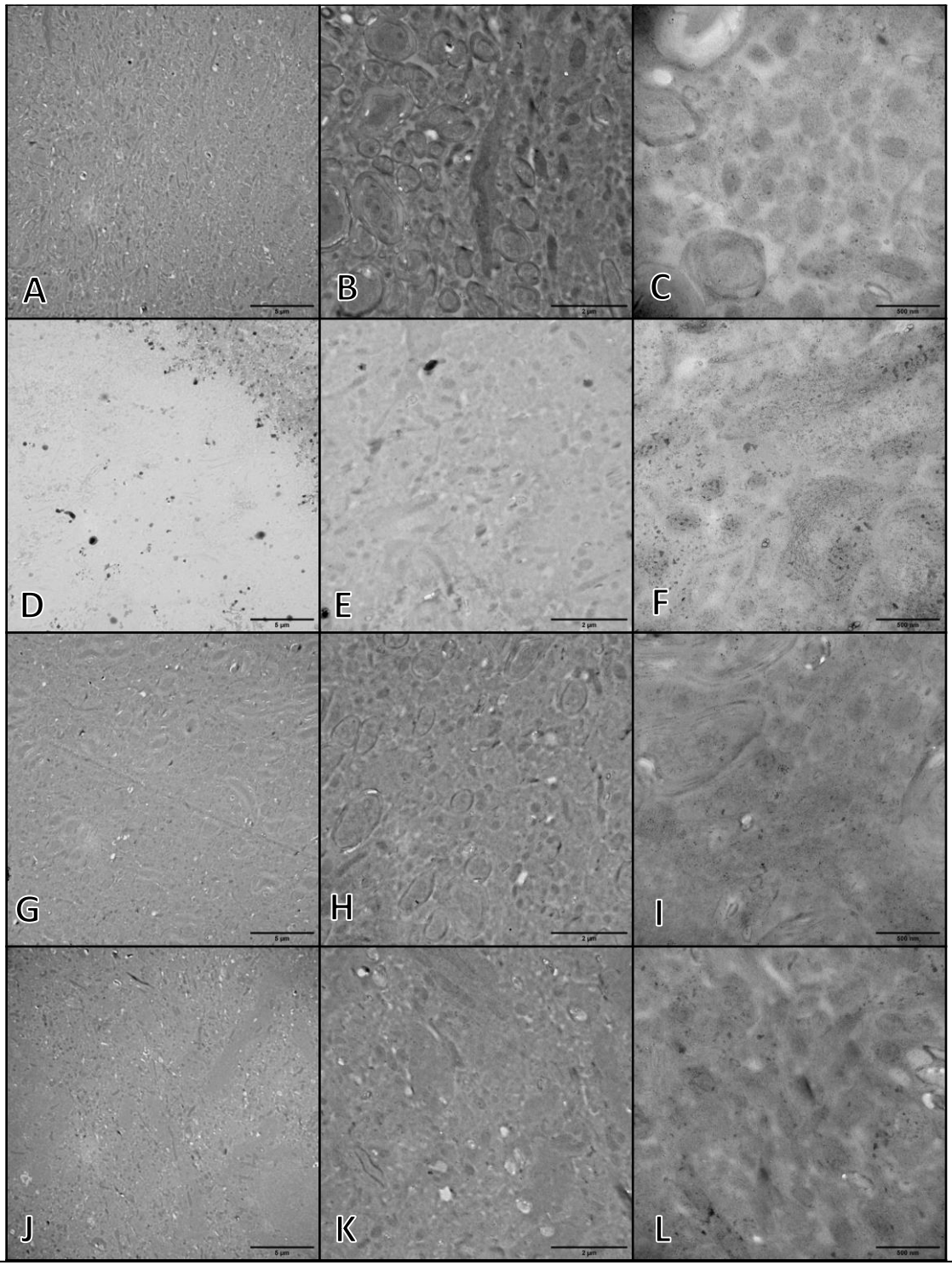

Figure 11. TEM images of glutaraldehyde-fixed TE3 tissue in HM20 on pioloform slot grids. *A:* 5000x image of section stained for GABA (1:1000) using streptavidin-conjugated quantum dots (1:200) and biotinylated secondary antibodies (1:200). *B:* 15000x image of grid from *A. C:* 50000x image of grid from *A. D:* 5000x image of a control section stained with streptavidin-conjugated quantum dots (1:200) and biotinylated secondary antibodies (1:200). *E:* 15000x image of grid from *D. F:* 50000x image of grid from *D. G:* 5000x image of section stained for GABA (1:1000) using streptavidin-conjugated quantum dots (1:200) and biotinylated secondary antibodies (1:200). *H:* 15000x image of grid from *G. I:* 50000x image of grid from *G. J:* 5000x image of a control section stained with streptavidin-conjugated quantum dots (1:200) and biotinylated secondary antibodies (1:200). *K:* 15000x image of grid from *J. L:* 50000x image of grid from *J.*

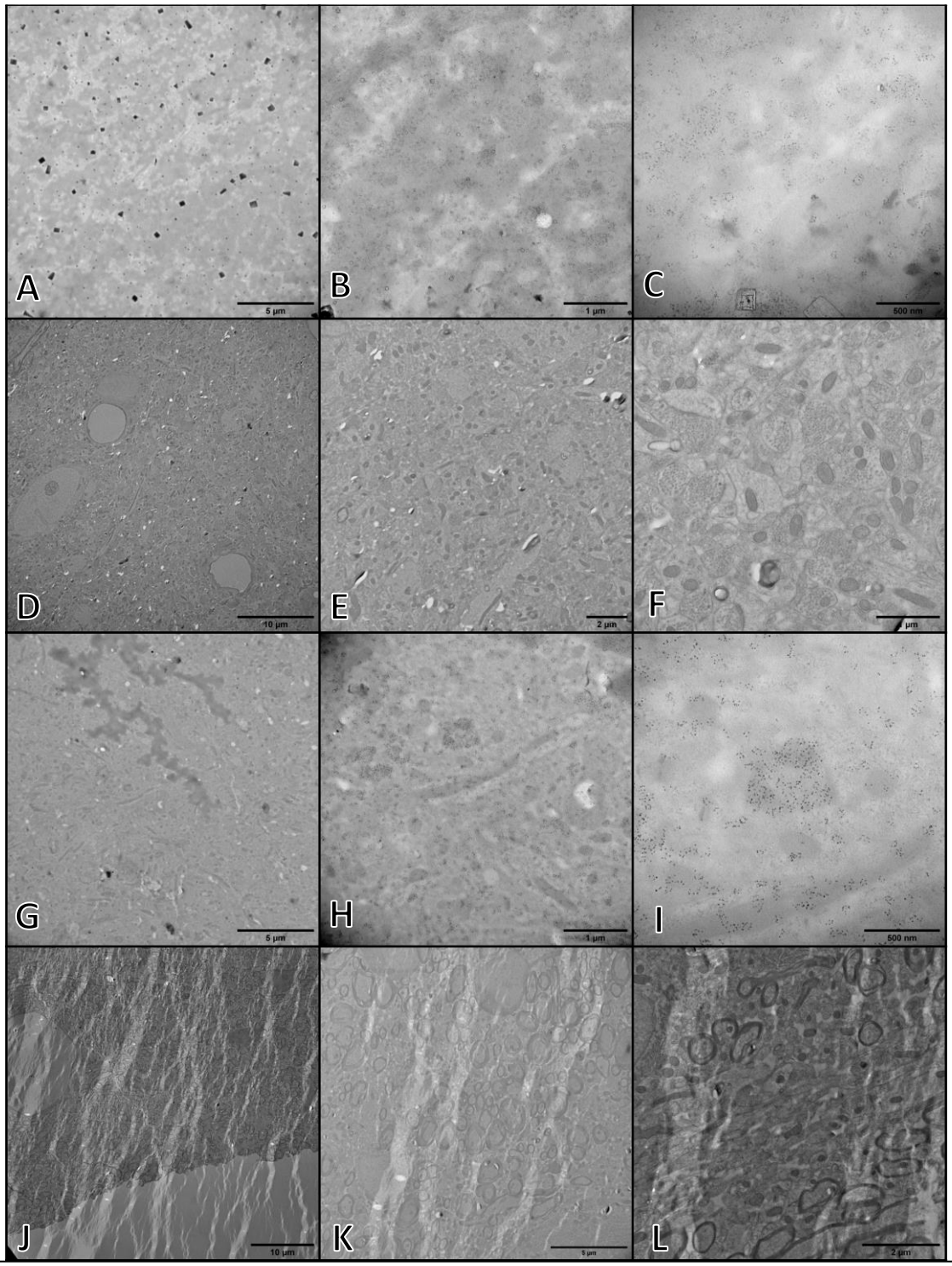

Figure 12. TEM images of glutaraldehyde-fixed TE3 tissue in HM20 on pioloform slot grids. *A:* 6000x image of section stained for GABA (1:1000) using streptavidin-conjugated quantum dots (1:200) and biotinylated secondary antibodies (1:200). *B:* 25000x image of grid from *A. C:* 50000x image of grid from *A. D:* 3000x image of a control section stained with streptavidin-conjugated quantum dots (1:200) and biotinylated secondary antibodies (1:200). *E:* 8000x image of grid from *D. F:* 25000x image of grid from *D. G:* 6000x image of section stained for GABA (1:1000) using streptavidin-conjugated quantum dots (1:200) and biotinylated secondary antibodies (1:200). *H:* 25000x image of grid from *G. I:* 50000x image of grid from *G. J:* 2500x image of a control section stained with streptavidin-conjugated quantum dots (1:200) and biotinylated secondary antibodies (1:200). *K:* 6000x image of grid from *J. L:* 15000x image of grid from *J.*

2.7 TEM IHC and Imaging

After sections are collected on grids, they can finally be stained for IHC. This is known as "post-embedding IHC", which is IHC done on tissue after it has been embedded in resin in contrast to "pre-embedding IHC". Post-embedding IHC presents a challenge in that the antibodies must work not only in the tissue but in the resin as well. Many post-embedding TEM IHC protocols use colloidal gold particles to label structures, but this has many downsides (De Roe et al., 1987; Peng et al., 1993; Morphew et al., 2008). For one, the small size of a gold particle limits the number of IgG molecules that can bind to it. Larger gold particles, on the other hand, tend to stick non-specifically to the tissue and the resin, producing unclear results (Birrell et al., 1987). Other labeling techniques utilize quantum dots (Qdots) instead of gold particles, which potentially solve some of the issues introduced with gold labeling (Nisman et al., 2004; Killingsworth et al., 2012; Szymanski et al., 2013).

Consisting of a metal core surrounded by a polymer shell, Qdots can be visualized in the TEM as well as in the LM. Although the Qdots that we used did tend to stick to our films, we found them to have better specific labeling than gold particles. To decrease the non-specific binding on our films, we added cold water fish skin gelatin (CWFSG) to our blocking, primary, and secondary incubation steps in the protocol. Although the exact mechanisms are still being worked out, gelatin has been shown to reduce non-specific binding and improve stability of Qdots (Parani et al., 2018). However, our results were inconsistent. We found that the gelatin tended to dry down on our sections and was not easily rinsed away (Figures 11 – 12). We tested different dilutions of CWFSG and heating it to warmer temperatures before adding it to the buffer but could not produce reliable results.

In addition to gelatin drying down on our samples, we noticed salts and other particulates would often show up on our grids and occlude the tissue. Because of this, we suspected that our rinses in the IHC protocol needed to be adjusted. We tried longer rinses throughout the protocol and added an additional rinse step of pure water at the very end. We noticed our grids clearing up from all the dried

down debris, but also started to notice a problem arise. As a side effect of more aggressive rinses, increased mechanical forces are applied to the grids by the rinse flowing against it. Several batches of grids being run for IHC had their films torn because of this, making it impossible to image the sections on the grid. We needed to figure out ways to improve our IHC process if we wanted to improve the rate of grid survival beyond what we had at the time.

A common method for staining TEM grids for IHC is to float each grid on a droplet of reagent or to drop the reagent directly onto the grid (Morphew et al., 2008). In the former method, the face-down section makes direct contact with whatever solutions you are using throughout the process (Figure 13). This method works well for situations in which you have very few grids to stain, but quickly becomes unwieldy with each additional grid. Since each grid must be picked up and set down using forceps, great care must be taken as to not puncture the film. During grid staining, this results in the user having to take a great deal of time to carefully position each grid and creates a disparity between incubation times across grids. Another disadvantage of this method is that the grids tend to sink into the droplet rather than staying afloat on top. We found that unless we were extremely precise with our grid placements, they would easily break the surface tension of the solution and fall to the bottom of the well. In addition to mechanical stress from this falling action, the solution now comes into contact with both sides of the grid. This proves to be an issue in that if this happens, as materials in the solution such as salts or antibodies can dry onto the back side of the grid. To deal with this, the user must rinse both sides of the grid if it falls into the droplet during any step of the IHC protocol. Not only is this an additional time-consuming step, but it further increases the amount of mechanical stress on the grid.

After several weeks of mixed results using this method, we decided to explore other alternatives. While the drop method is a common protocol for doing IHC on TEM sections, other methods do exist (Edén et al., 1979; Forsdyke, 1979; Håkonsen et al., 1984; Shi et al., 1990). Tools such as a grid stick use a metal rod to hold grids vertically inside a small tube. Solutions are then drawn up into the grid stick,

allowing the grids inside to come in contact with the solution without having to pick up each one after each step. However, commercially available grid sticks contain metal that can interfere with IHC. Another downside is that it uses a large volume of solution for each step, which we wanted to minimize. We came up with a modified version of the grid stick by cutting off the tips of plastic transfer pipets and connecting them together (Figure 13). The uppermost pipet tip was then connected to a syringe, and the lowermost tip was left open to draw up solutions. One grid was placed into each section of pipet and was aligned vertically by applying pressure with forceps to push it slightly into the plastic. This pipet tip method not only solved the problem of metal with the grid stick method, but also used a much smaller volume of solution.

While we had high hopes for this setup, it proved to have too many flaws to be a viable solution in the long run. We first found out that due to the small size in each pipet chamber, bubbles would often form in between the grid and the wall of the pipet. These bubbles did not have enough space to be pushed out and could only be removed by vigorously tapping the device, which sometimes broke the pipet chambers apart. Because the bubbles prevented the sections on the grid from being in contact with the solution, we found that some grids were not being labeled by our primary antibodies. Another flaw of this method was the mechanical force of the solution passing through the pipet chambers. Although we aligned the grids vertically in the chambers to minimize this force, some films still broke as a result. To solve this problem, we tested used a syringe pump to draw up and discharge our solutions at a constant speed that was much gentler than doing so by hand (Figure 13). Doing so solved some of the problems with this method, but other issues persisted.

Because we needed access to each pipet chamber after the IHC protocol was completed, we could not fasten each chamber together using permanent adhesive. Instead, we relied on friction between each chamber to hold the device together throughout the protocol, which did not always work. We found that when handling the device, sometimes the pipet chambers would fall apart and cause the solution to flow

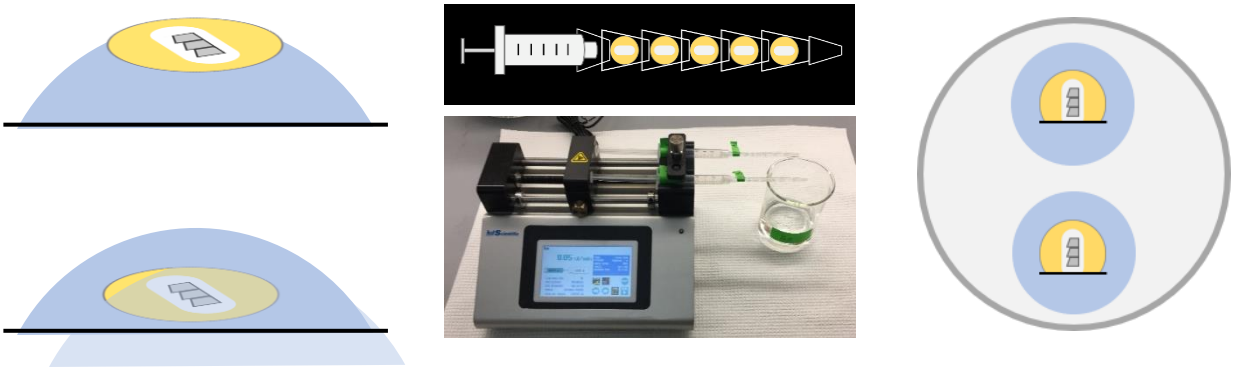

Figure 13. Grid staining techniques. *Top Left:* Floating method. Grids are placed section-side down onto droplets. *Bottom Left:* Illustration of a common issue with the floating method. Note that once a grid has fallen into the droplet, it must be rinsed on both sides for the remainder of the IHC process. *Top Middle:* Pipet tip method. Grids are placed into sections of pipet tips connected to a syringe. *Bottom Middle:* Pipet tip method using syringe pump. Note that the pump automatically draws in and pushes out reagent at a set speed or volume, reducing mechanical stress on the grids. *Right:* Petri dish method. Grids are placed vertically into slots cut into either paraffin wax or agarose. Note that for this method, both sides of the grid are in contact with the reagent during all steps of the protocol.

out. In addition, since we could not permanently attach each grid to its pipet chamber, we had to rely again on friction to hold it in place. To do so, we had to wedge the grids into the tapered ends of the pipets using forceps that would sometimes slip and tear the grid film. After the IHC was completed, removing the grids presented a similar challenge in having to generate enough force to pull each one out. All in all, this method proved to be too time consuming and have too high of a rate of grid failure to continue using it.

As a result, we went back to the drawing board to find a better way to stain our grids for IHC. We tested an adapted version of the grid staining device from Håkonsen et al., 1984, placing the grids vertically in small notches in a semi-malleable material at the bottom of petri dishes (Figure 13). This method minimized the volume of primary antibody solutions used by being able to pipet a single drop onto the front face of each grid. During the rinsing steps, the entire dish could be quickly filled with buffer that could then be dumped out. We tested this method with two materials holding our grids: wax and agarose. We found that using wax was not the easiest method since we had to melt it down and re-cut the grid notches for each IHC batch. Since these notches held the grids in place, they had to be small

enough to prevent the grid from moving back and forth during the protocol. We used a scalpel to make the notches and forceps to insert and remove the grids. After removing the grids, the notches would be slightly too big to hold a new grid snugly in place.

The second material we used was agarose. We found that this method worked much better for us, since the agarose did not change shape when inserting or removing grids. However, this method still required us to push each grid into something using forceps, and we found that some of our films continued to break due to this mechanical stress. We found that despite these drawbacks, this method worked the best for us and gave us the most reliable results out of the methods we tested. Images of grids stained with Qdots can be seen in Figures 11 and 12. Once we had the grid staining protocol sorted out, we started to notice another set of problems that needed to be solved.

2.8 IF IHC and Imaging

Throughout the TEM IHC experiments, we noticed inconsistent labeling patterns of our antibodies. We decided that to draw any meaningful conclusions from our results, we needed to make sure that our primary antibodies were working in the first place. Due to the high number of uncontrollable variables alongside the time-intensive nature of doing IHC on TEM grids, we decided to test our antibodies using immunofluorescence. We reasoned that doing so would provide faster results regarding the efficacy of the antibodies and would thus allow us to continue with serial multiplexed labeling using the TEM. Additionally, any antibody that would not work at the light-resolution level had little chance of working at the EM level. For quantification, we could measure the signal-to-noise ratio of labeled sections, which would indicate whether the antibodies worked (Figure 14).

Our IF antibody testing experiments began by mounting sections 100 to 500nm in thickness onto subbed slides. In addition to the challenges regarding slide mounting discussed in §2.5, slide mounting sections for IF IHC presented its own set of unforeseen problems to work out. For the best possible

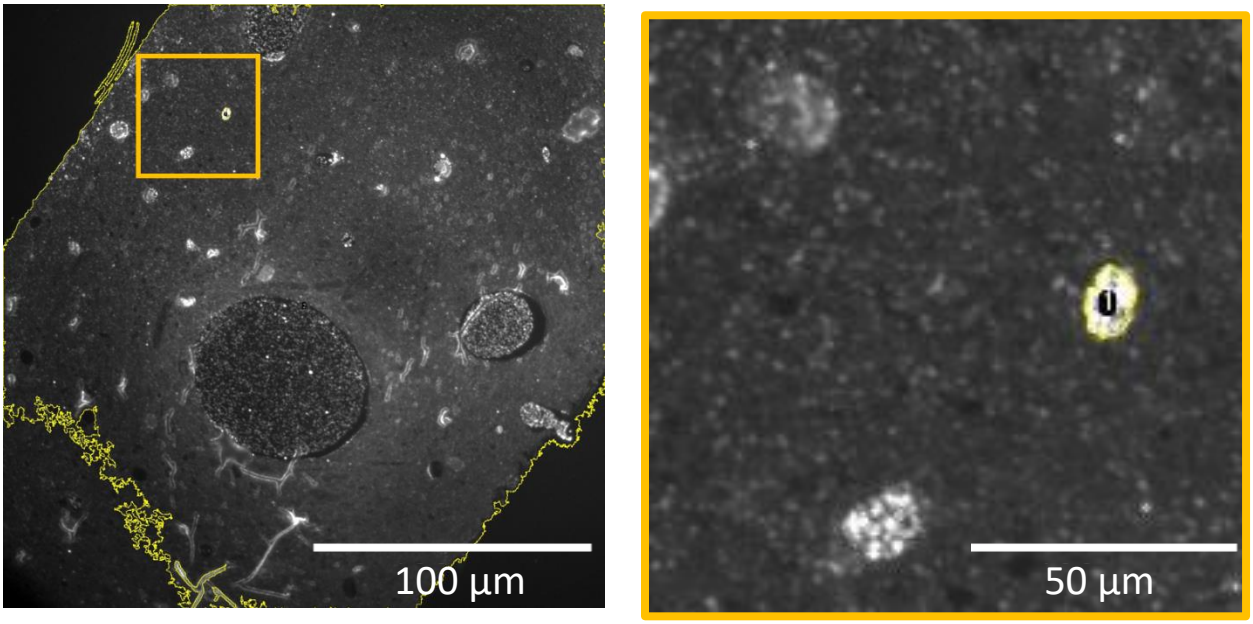

Figure 14. Methods for quantifying IF results. *Left:* High magnification image of tissue labeled for calbindin. Yellow outline marks wand tool-denoted boundaries to measure noise intensity. *Right:* Enlarged view of orange area from image on left. Labeled cell body traced in yellow is used to measure signal intensity.

resolution in the LM, slide-mounted sections should be as flat as possible. If they are not, the section will have wrinkles that attract antibodies and make it difficult to see. We did not know this when we began this experiment, so many of our first batches turned out to have too many wrinkles to be viable. We found out that using eyelash tools tended to warp the sections so much that they would not lay flat on the slide, and that the perfect loop produced flatter sections overall. In addition to this, other sectioning-related issues cropped up during this experiment that we did not account for when we started.

To validate the efficacy of our antibodies, serial sections had to be obtained so that we could compare labeling patterns across adjacent sections. Because non-serial sections are easier to obtain, we started off doing this and switched to serial sections halfway through the project. However, gathering reliable serial sections turned out to be a much greater challenge than we ever expected given the limited number of resins that we could use. We tested LRW, K4M, and MBA for IF IHC, and each had their own unique challenges to overcome. Because our LRW blocks were embedded into rounded gelatin capsules,

the sections do not easily form ribbons in the boat. Although part of this issue was mitigated through various trimming techniques discussed in §2.5, it remained incredibly difficult to gather a fully intact and structurally sound ribbon of LRW sections in the knife boat.

If sections do not have a ribbon to hold them together, they will simply float around on the water surface in the knife boat. In the case of LRW, which is a hydrophilic resin, the sections come flying off the knife edge the moment the block passes over it, making it nearly impossible to gather serial sections one at a time. To solve this, we took two different approaches. Our first solution was to cut only a few sections at a time and to keep track of the serial order of the sections in the boat carefully. Due to the size of the sections, this was only possible with up to four at a time. We therefore started cutting sets of three to four serial sections at a time with pauses in the microtome process in between each set. Using an eyelash tool, we kept track of the order of the sections as they came off the knife, and then picked them up and mounted them on slides in the same order. This method worked to a certain extent but had some downsides to it. Because the microtome is paused in between each set of sections, the first section in each set has a different thickness than the rest of the sections due to minor changes in the microtome's position during the pause. Not only was this method extremely time-intensive, but it produced sections that were not all the same thickness.

The other approach we took towards solving this challenge was to use an adhesive to hold the sections together into a ribbon. We tested a variety of cocktails of off-the-shelf rubber cement diluted in toluene which we then dipped our blocks into. We theorized that the adhesive properties of the rubber cement on the face of the block would hold the sides of the sections together in the knife boat, but we were not able to get this to work. Because of the challenges with LRW, we tried sectioning K4M in hopes that this would be an easier route. However, due to issues previously discussed, this also did not work very well for us. In most cases, blocks of K4M were unable to cut properly thick sections for myriad reasons. Most frequently, we noticed K4M crumbling under the mechanical stress of the knife pressing

into the resin, resulting in usable sections that could not be rescued. In rare instances where the resin was able to cut, the sections easily formed structurally sound ribbons in the knife boat, but this was inconsistent.

Due to these setbacks, we decided to adjust our sectioning protocols regarding LRW. We reasoned that we could collect a batch of non-consecutive serial sections on slides and then order the sections digitally based on their images. In doing so, we could circumvent the issue of LRW being unable to form ribbons in the knife boat. Because we were cutting our samples so thin and we would be basing our results from labeled cell nuclei, we could pick up sections from a sample volume as deep as a cell body in any order. To do this, we let the microtome run until the knife boat would fill up with sections, and then picked them up onto slides. We found that this method worked the best for us out the section pickup procedures discussed thus far, but it too came with some limitations. Notably, the size of the knife dictates the number of serial sections that can be attained by this method. If the user is looking to acquire a large set, the boat must be large enough to hold more sections in it than if the user were collecting a small set. In addition, the sections must be imaged in a precise way to ensure the ability for serial alignment. After learning about the merits of MBA, we decided to test it out for IF IHC. We found MBA to be one of the easier resins to cut on the microtome and that it showed promising IHC results (Figures 19 – 20).

After refining our serial sectioning protocols, we started testing several different antibodies. We started with SMI-312, a cocktail of antibodies that labels axons (Figure 15). We then moved on to GABA (Figures 16, 19), CalB (Figures 18, 22 – 29), CalR (Figures 21, 34 – 37), CGRP (Figures 30 – 33), PV (Figures 17, 20, 38 – 40), and VGlut1 (Figure 18). At the beginning of the experiment, we did not know what dilution of primary antibodies to use, so we tested a variety of dilutions for all of them. We wanted to use the smallest possible amount of antibody to reduce costs while still producing reliable labeling. As a result, we ran several batches of IHC using dilutions of primary antibodies that we later decided were too diluted

to pinpoint any signal in the images. After increasing the concentration of our primaries, we began seeing results that were closer to what we expected. These results can be seen throughout Figures 17 – 40.

The goal for this portion of the project is illustrated in Figure 17. Here we see the same field from two serial sections stained for parvalbumin. In these images we can clearly resolve labeled nuclei based on consistent staining across sections. While we hoped to be able to do this for all our samples, we ran into several issues along the way that we did not account for. Towards the beginning of the project, we found that we were using too much hydrophobic pen around the sections and that it was interfering with the imaging process. Since there was too much material on the slide, the coverslip did not sit flat on the slide and impeded the ability to achieve in-focus images. In addition to this, our cover-slipping protocol at the beginning of the experiment turned out to be causing problems. We added too much cover-slipping media to the slides, which resulted in a similar problem to the hydrophobic pen. Unfortunately, it was not until after many batches of IHC that we found out we were doing things the wrong way. Once we had all these issues ironed out, however, we were ready to begin full-scale antibody testing as we sought out to do. Unfortunately, we ran out of time before we could complete this part of the project.

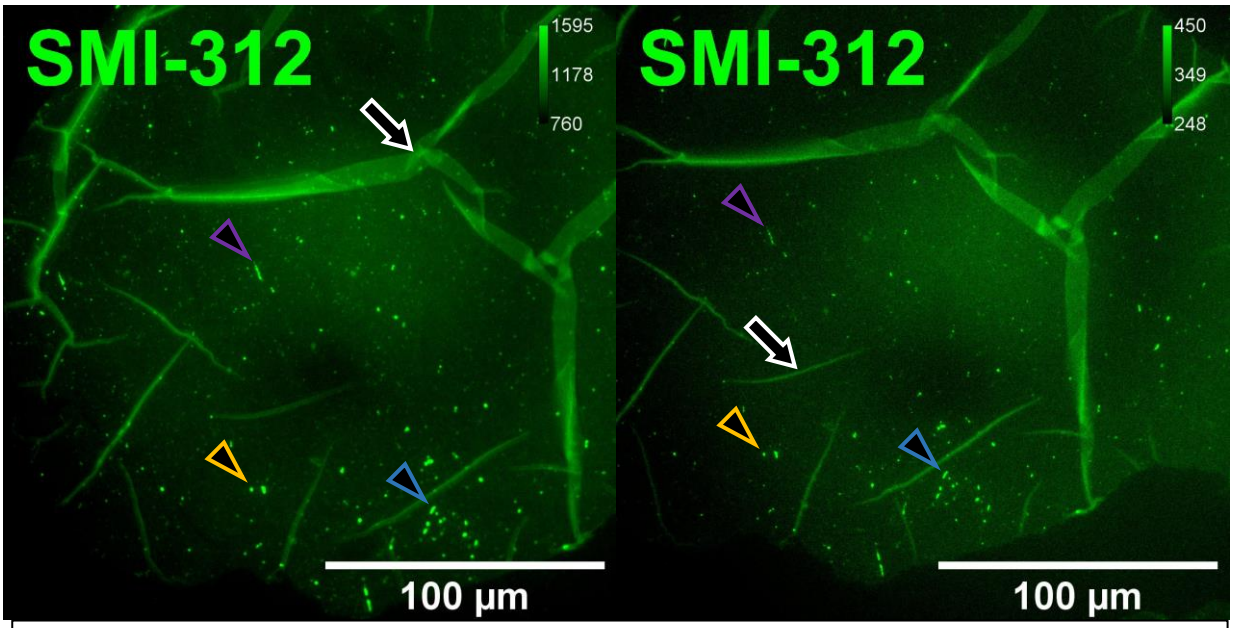

Figure 15. 60X IF images of two non-consecutive serial sections stained for SMI-312 at a dilution of 1:200. This tissue was embedded in LRW prior to being sectioned at 250nm. A control condition was run alongside this batch but was unable to be imaged in time. Arrows indicate wrinkles in the tissue that cause non-specific labeling, arrowheads indicate consistently labeled structures across sections.

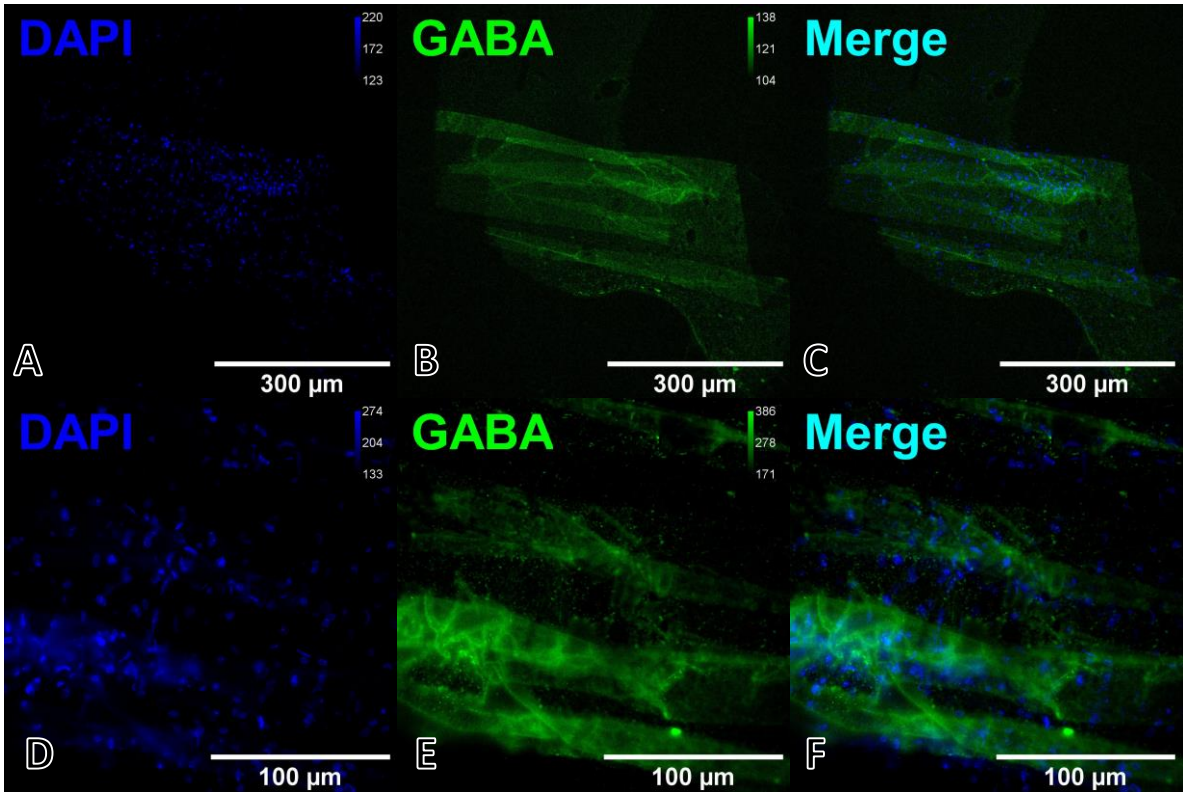

Figure 16. IF images of F.12.01G.1.P.b stained for GABA (1:5000) at 20X (*A – C*) and 60X (*D – F*). This sample was fixed with 0.1% glutaraldehyde/4% PFA in 0.1M PB and was frozen without any fillers prior to being embedded in LRW and sectioned at 250nm. A control condition stained without primary antibody was run alongside this batch but was unable to be imaged in time. Note that GABA^{+} nuclei cannot be resolved due to high intensity values of non-specific labeling of wrinkles. Imaging credit: Ethan Gasteyer.

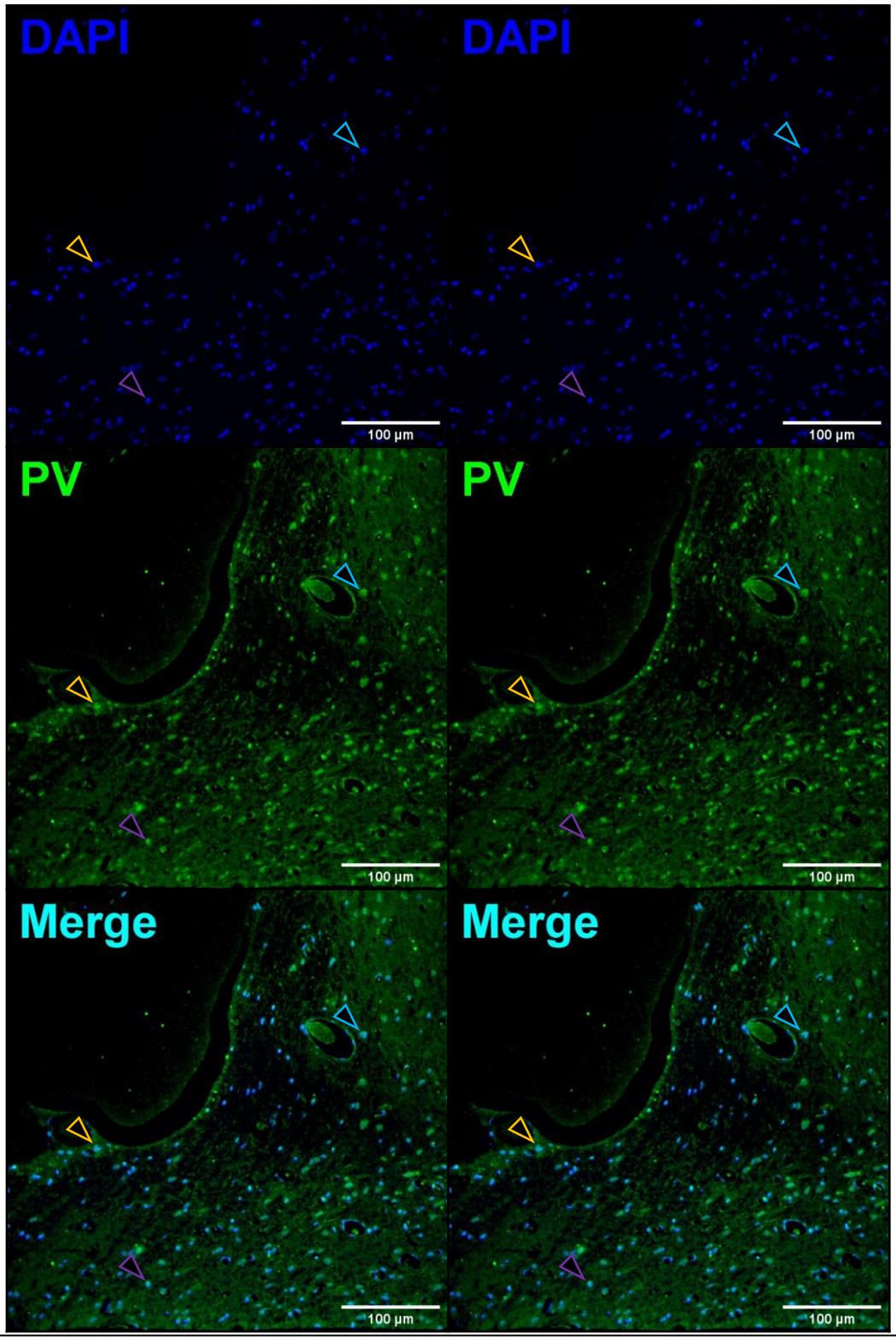

Figure 17. IF images of F.12.01G.1.P.b stained for parvalbumin (1:50) on two serial sections (*A – C*; *D – F*). This sample was fixed with 0.1% glutaraldehyde/4% PFA in 0.1M PB and was frozen without any fillers prior to being embedded in LRW and sectioned at 250nm. These sections were kept on subbed slides at -20°C for 12 days prior to IHC. A control condition was run alongside this batch but was unable to be imaged in time. Color coded arrowheads indicate putative PV^{+} nuclei labeled across sections.

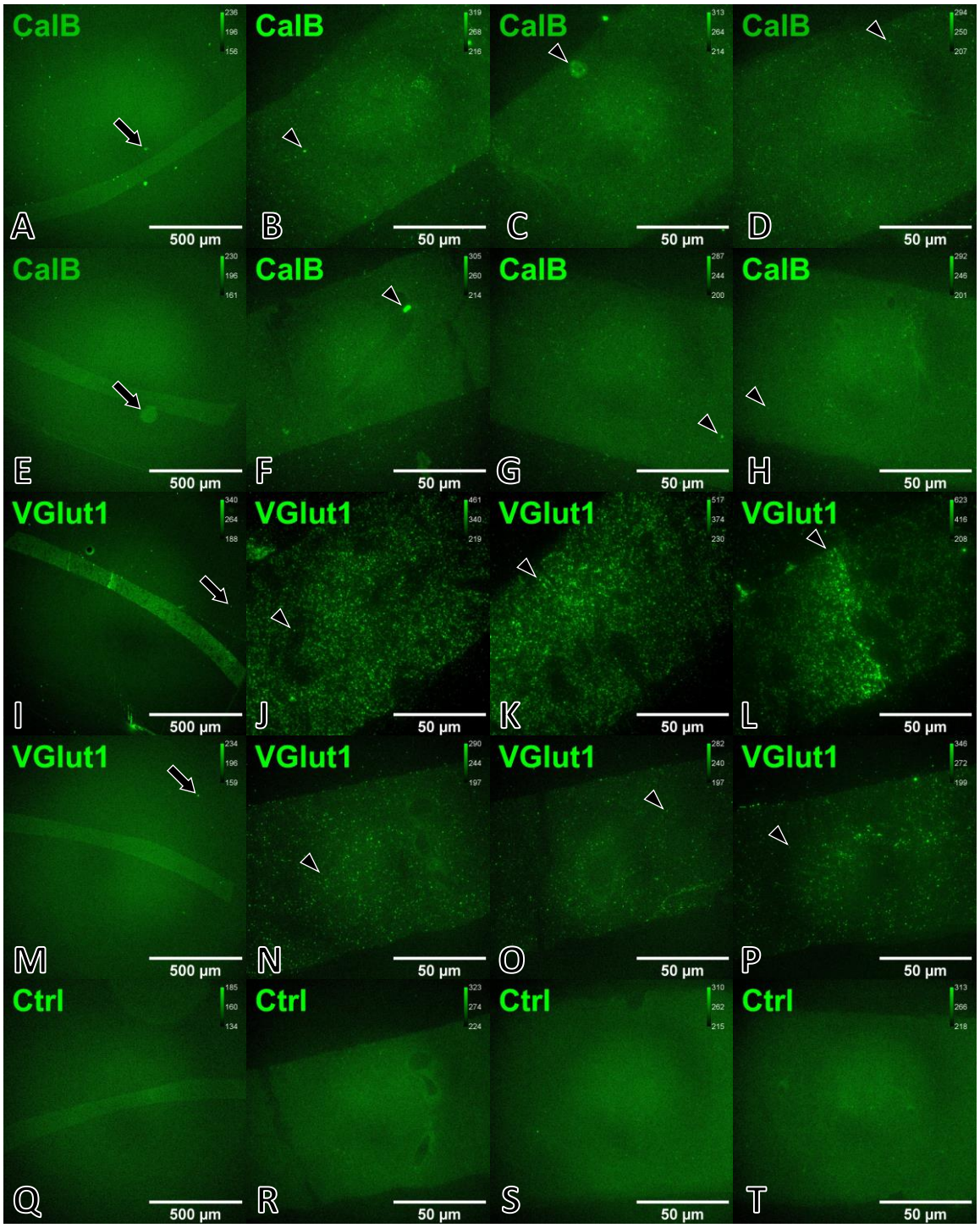

Figure 18. IF images of F.01.01G.1.L.e stained for Calbindin (1:4000, *A – D*; 1:6000, *E – H*) and VGlut1 (1:100, *I – L*; 1:5000, *M – P*) alongside a control condition stained without primary antibody (*Q – T*). This sample was perfused with 0.1% glutaraldehyde/4% PFA in 0.1M PB and was frozen with 20% BSA and hexadecene prior to being embedded in K4M and sectioned at 100nm. Arrows indicate background labeling of resin without tissue, arrowheads indicate non-specific labeling on resin embedded tissue.

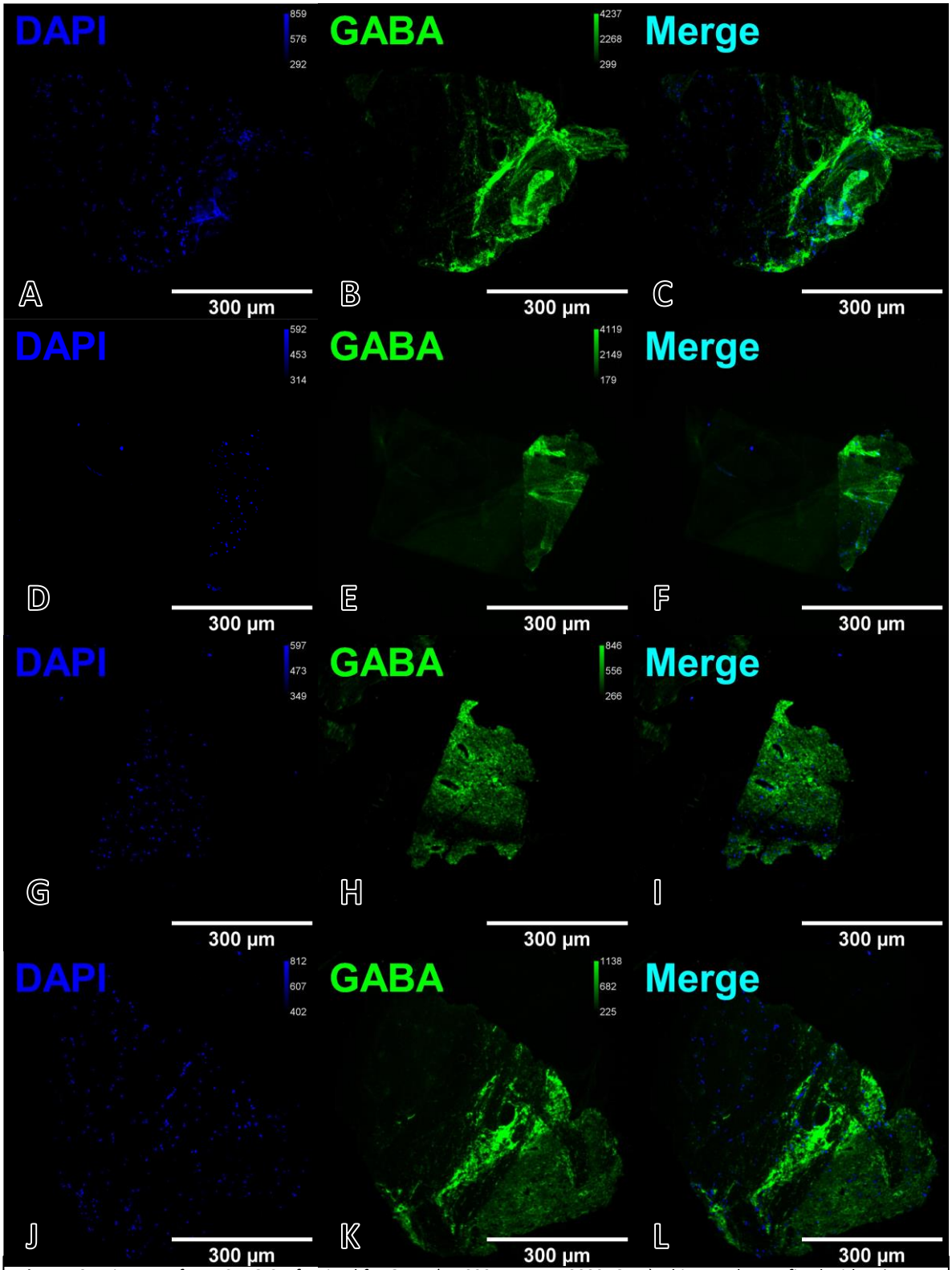

Figure 19. IF images of F.11.2PBQ.2.L.f stained for GABA (1:1000, *A – F*; 1:10000, *G – L*). This sample was fixed with 1% (saturated) parabenzoquinone/0.5% glutaraldehyde/4% PFA in 0.1M PB and was frozen with 20% BSA and hexadecene prior to being embedded in MBA and sectioned at 100nm. A control condition stained without primary antibody was run alongside this batch but was unable to be imaged in time. Note that $GABA^{+}$ nuclei cannot be resolved due to high intensity values of non-specific labeling.

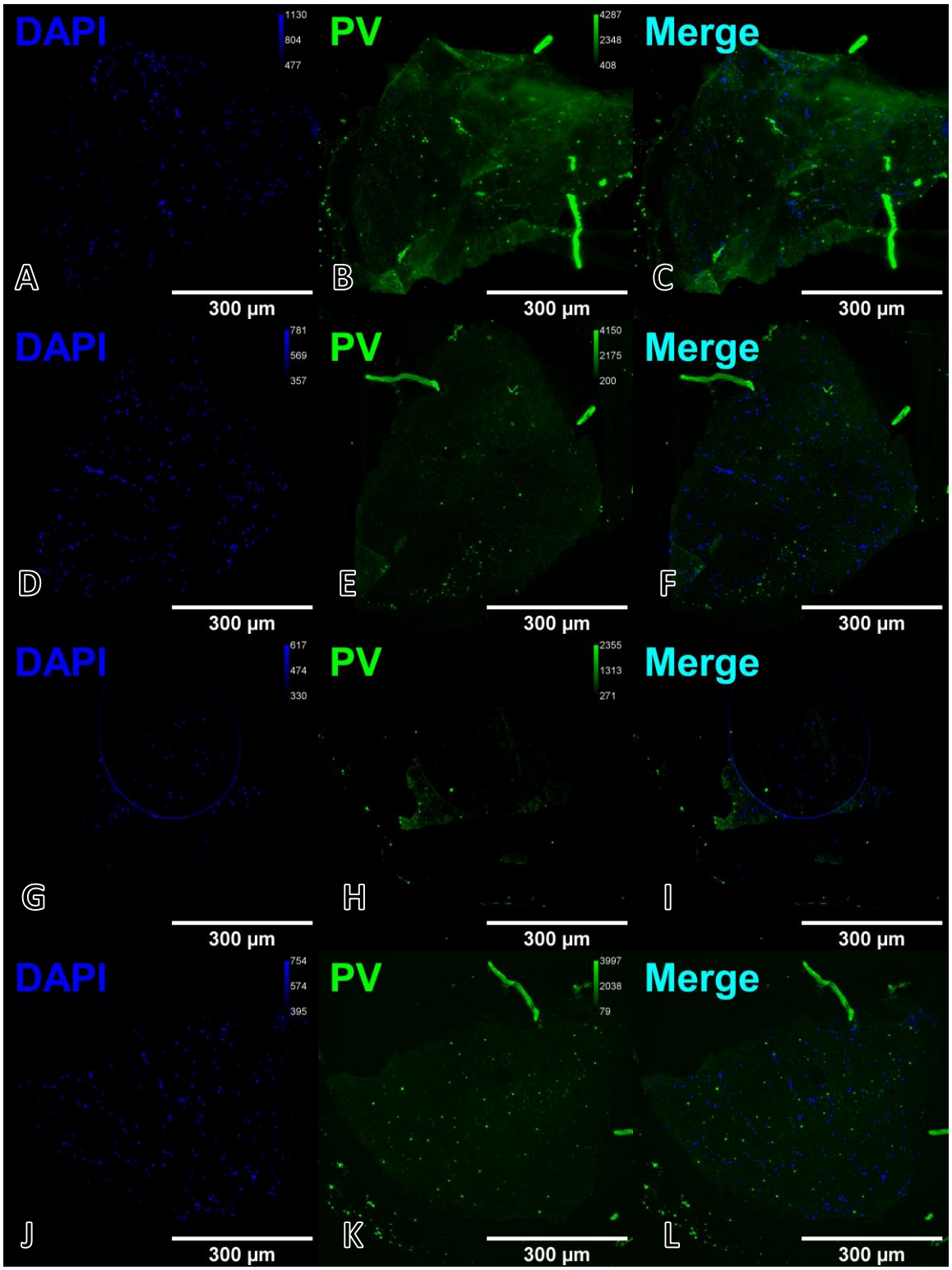

Figure 20. IF images of F.11.2PBQ.2.L.f stained for parvalbumin (1:50) to test the effects of acetone rinsing prior to IHC on immunogenicity. This sample was fixed with 1% (saturated) parabenzoquinone/0.5% glutaraldehyde/4% PFA in 0.1M PB and was frozen with 20% BSA and hexadecene prior to being embedded in MBA and sectioned at 100nm. Sections in panels *A – F* were treated with 100% acetone for 10 minutes prior to IHC; sections in panels *G – L* received no acetone treatment. Note that PV^+ nuclei cannot be resolved due to high intensity values for the PV images.

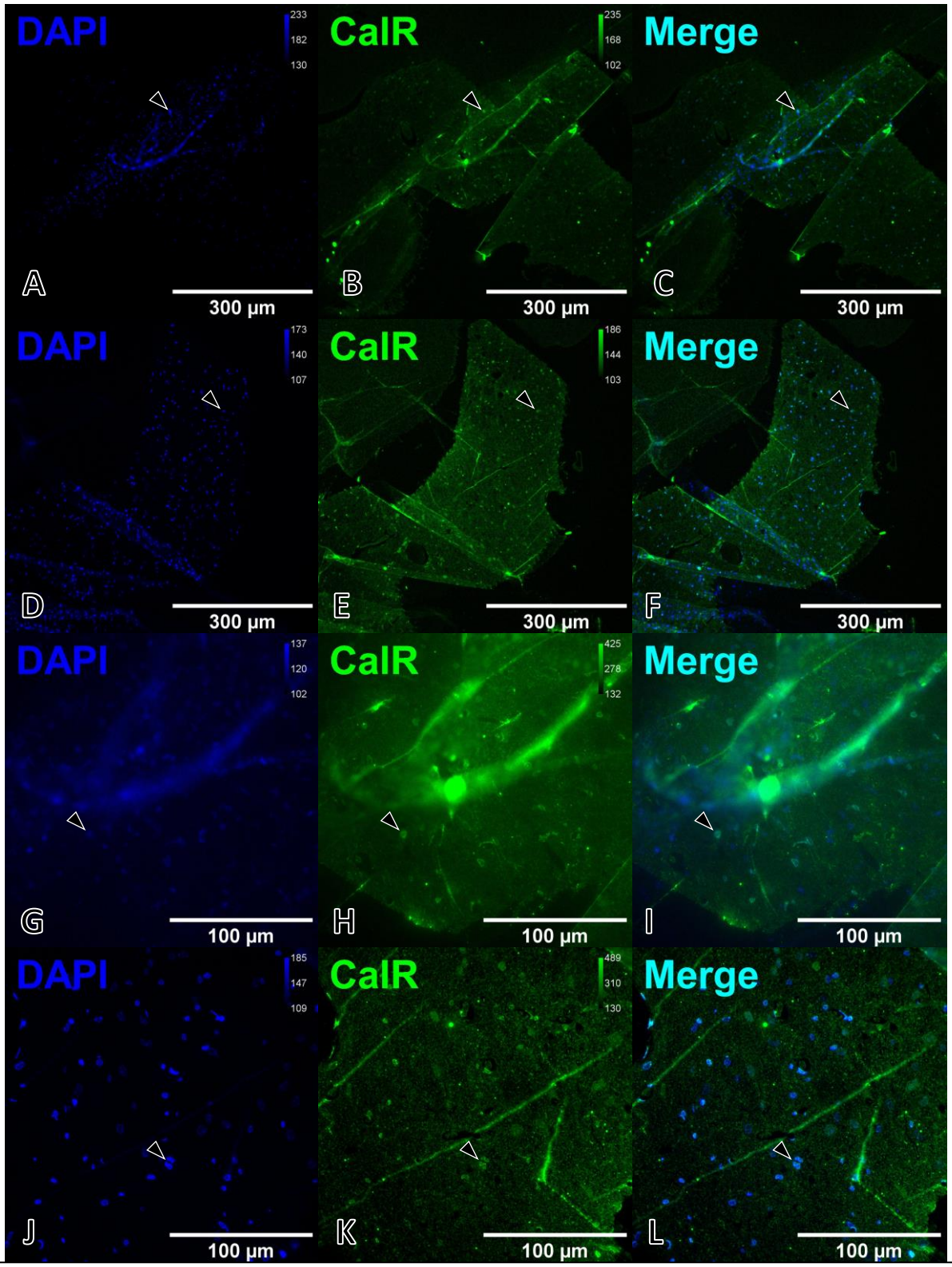

Figure 21. IF images of F.12.01G.1.P.b stained for calretinin (1:50) at 20X (*A – F*) and 60X (*G – L*). This sample was fixed with 0.1% glutaraldehyde/4% PFA in 0.1M PB and was frozen without any fillers prior to being embedded in LRW and sectioned at 250nm. A control condition stained without primary antibody was run alongside this batch but was unable to be imaged in time. Arrowheads indicate putative CalR^{+} nuclei. Imaging credit: Ethan Gasteyer.

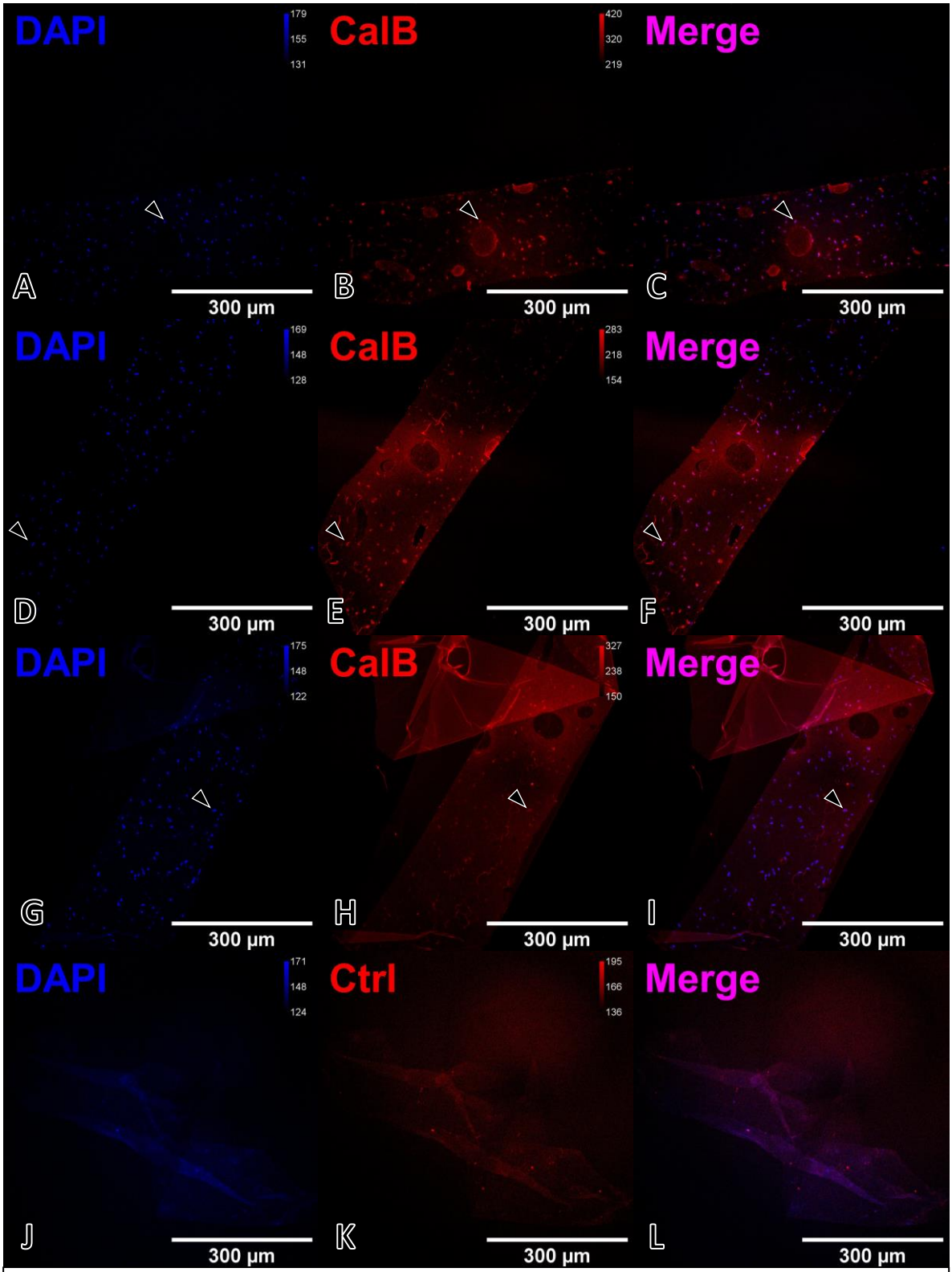

Figure 22. IF images of MGM-PIN 2 stained for calbindin (1:1000, *A – F*; 1:5000, *G – I*) compared to a control condition stained without primary antibody (*J – L*). This sample was micro-dissected and embedded into agarose prior to being embedded in LRW and sectioned at 250nm. Arrowheads indicate putative CalB^{+} nuclei. Imaging credit: Alison Chase.

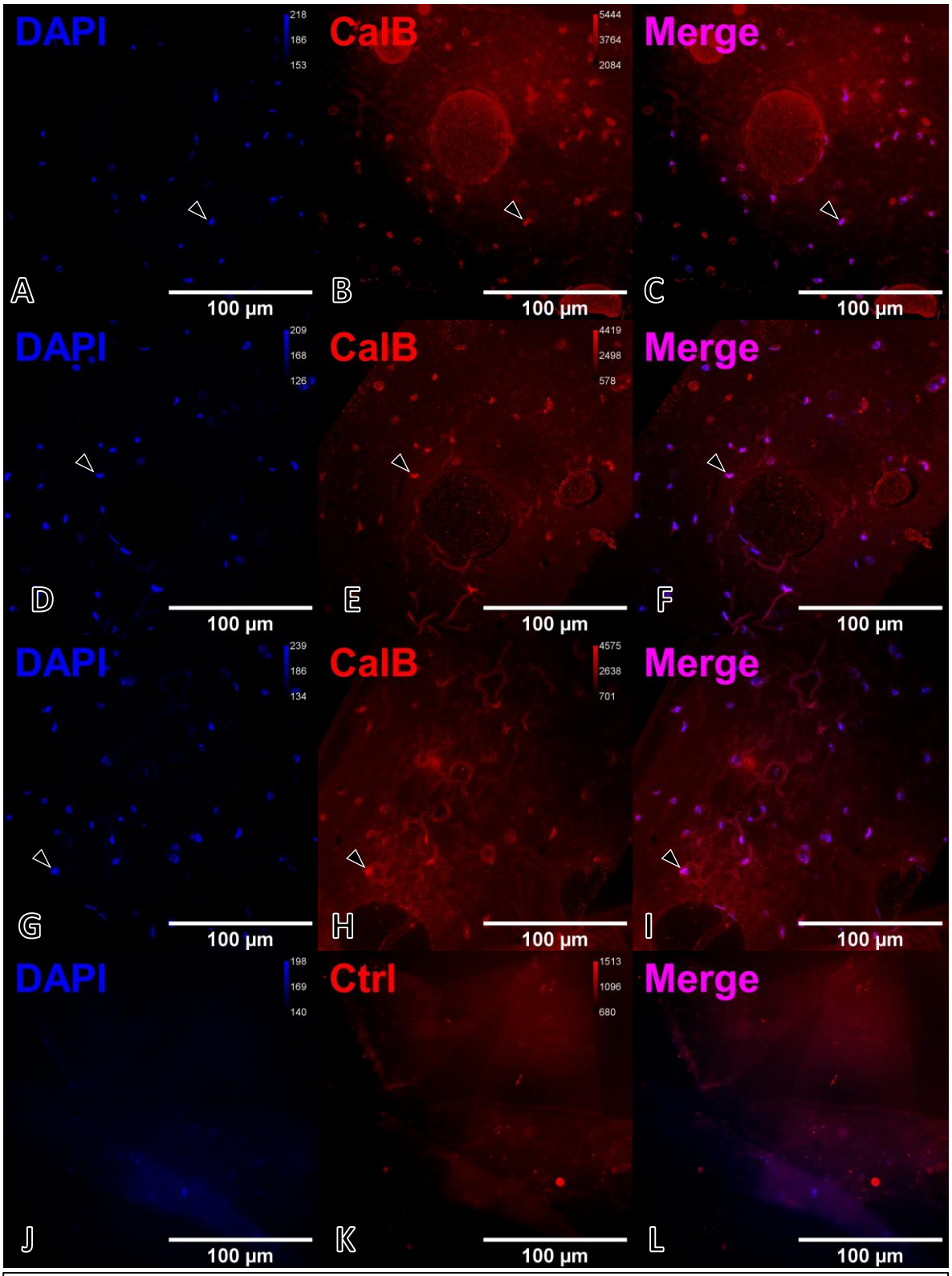

Figure 23. IF images of MGM-PIN 2 stained for calbindin (1:1000, *A – F*; 1:5000, *G – I*) compared to a control condition stained without primary antibody (*J – L*). This sample was micro-dissected and embedded into agarose prior to being embedded in LRW and sectioned at 250nm. Arrowheads indicate putative CalB^{+} nuclei. Imaging credit: Alison Chase.

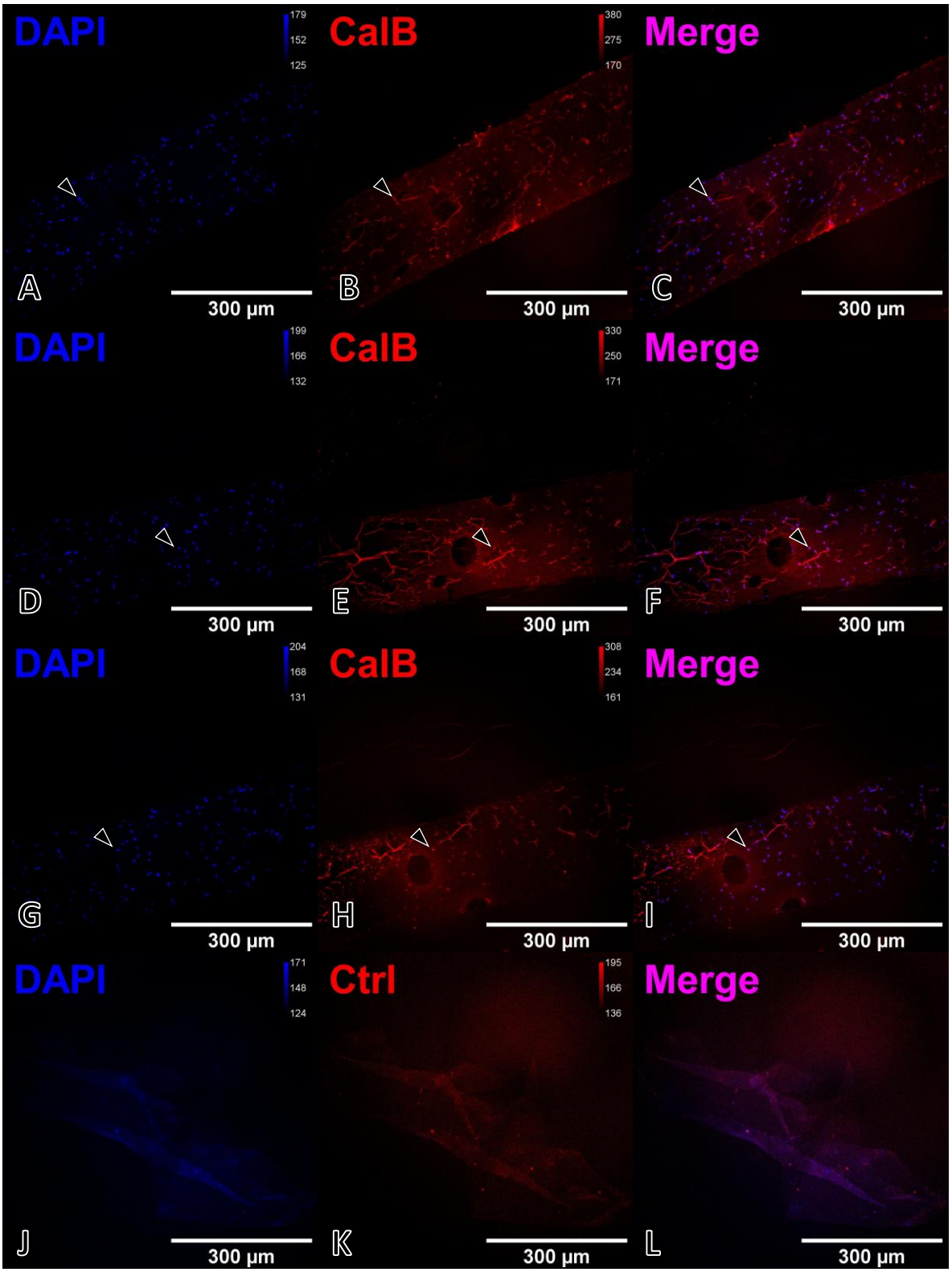

Figure 24. IF images of MGM-PIN 2 stained for calbindin (1:50, *A – C*; 1:500, *D – I*) compared to a control condition stained without primary antibody (*J – L*). This sample was micro-dissected and embedded into agarose prior to being embedded in LRW and sectioned at 250nm. Arrowheads indicate putative CalB^{+} nuclei. Imaging credit: Alison Chase.

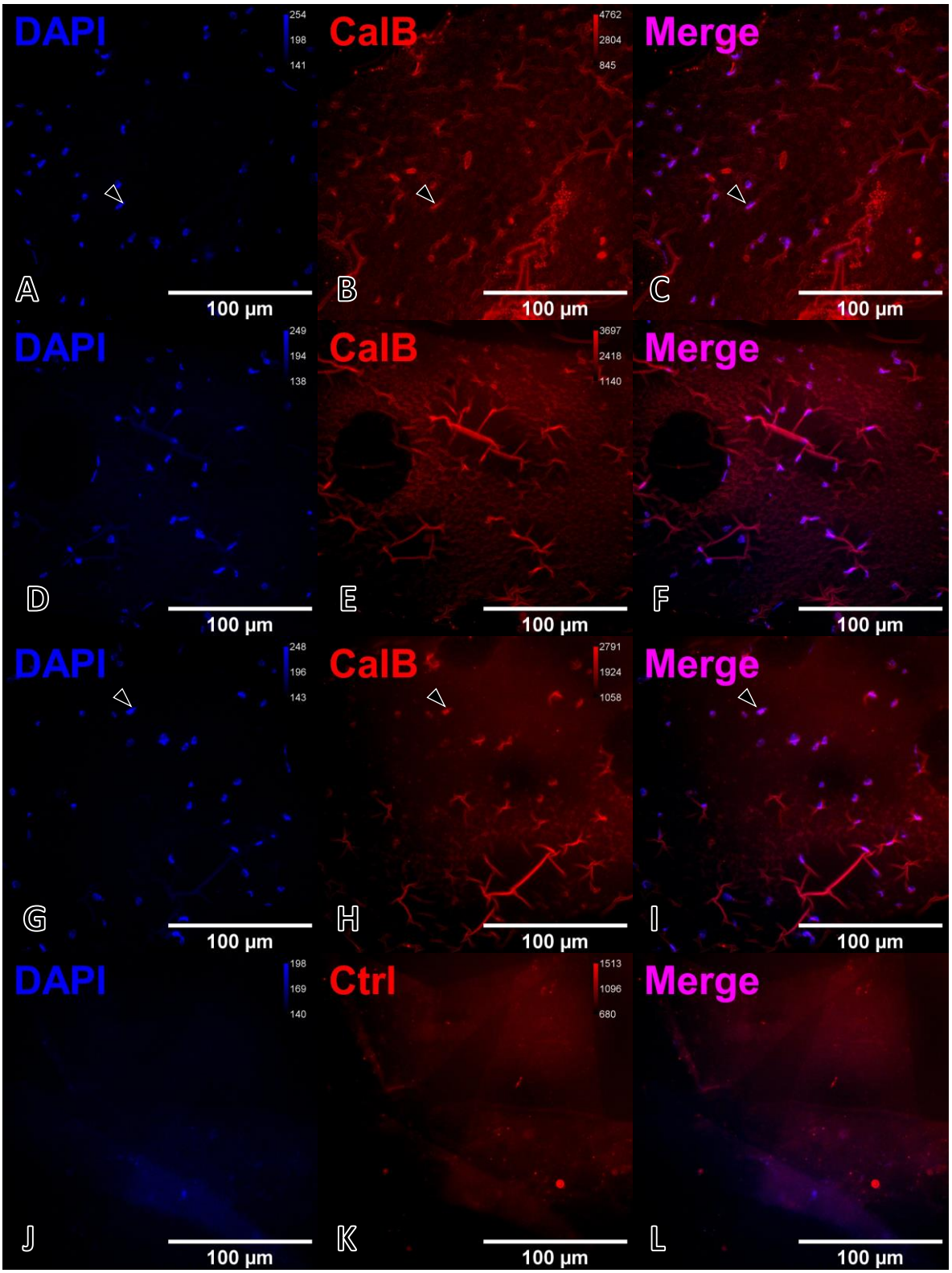

Figure 25. IF images of MGM-PIN 2 stained for calbindin (1:50, *A – C*; 1:500, *D – I*) compared to a control condition stained without primary antibody (*J – L*). This sample was micro-dissected and embedded into agarose prior to being embedded in LRW and sectioned at 250nm. Arrowheads indicate putative CalB^{+} nuclei. Note that we cannot determine strongly labeled nuclei in the second row due to wrinkle-induced non-specific binding. Imaging credit: Alison Chase.

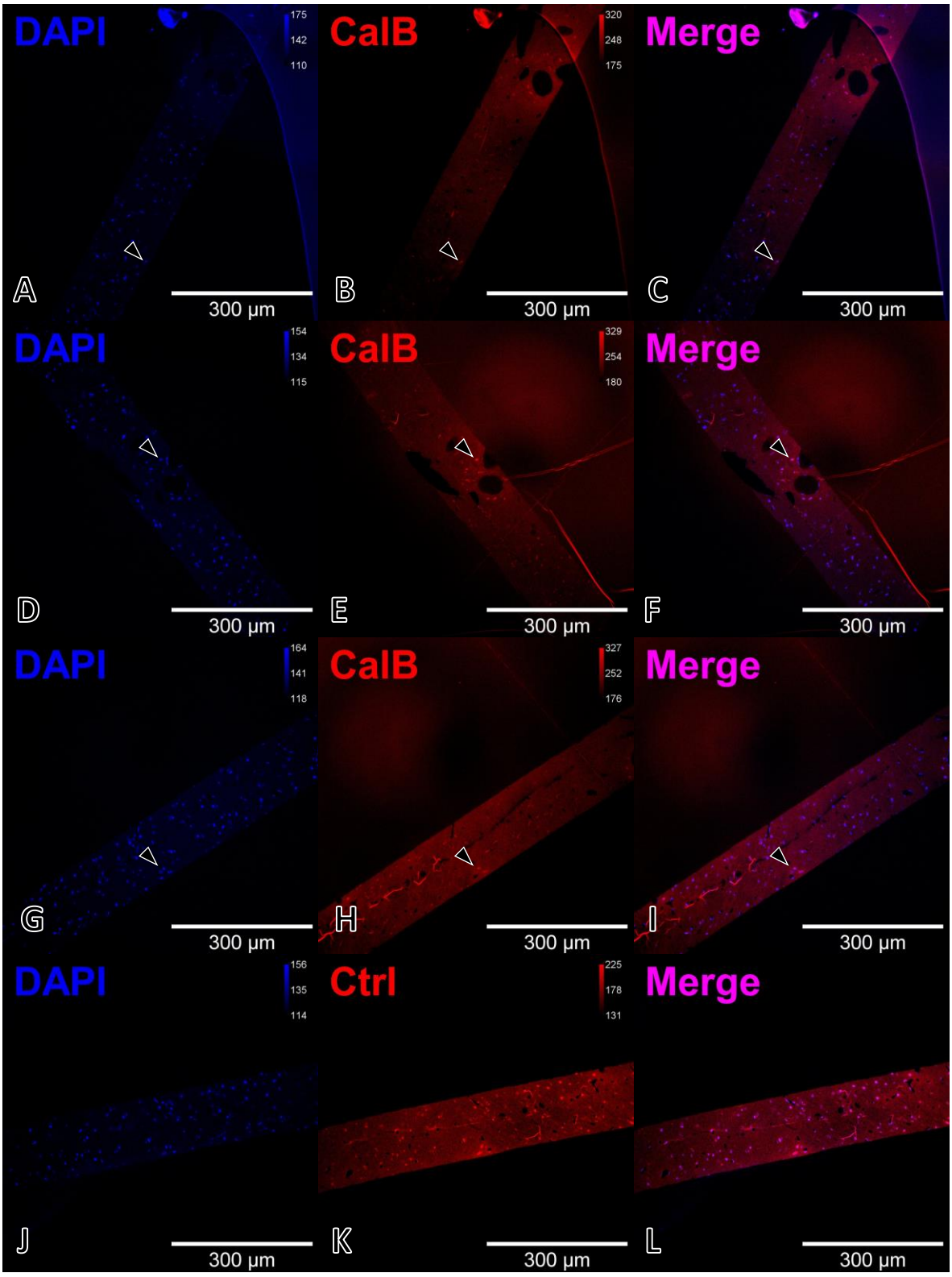

Figure 26. IF images of MGM-PIN 3 stained for calbindin (1:6000, *A – I*) compared to a control condition stained without primary antibody (*J – L*). This sample was micro-dissected and embedded into agarose prior to being embedded in LRW and sectioned at 250nm. Arrowheads indicate putative CalB^{+} nuclei. Imaging credit: Alison Chase.

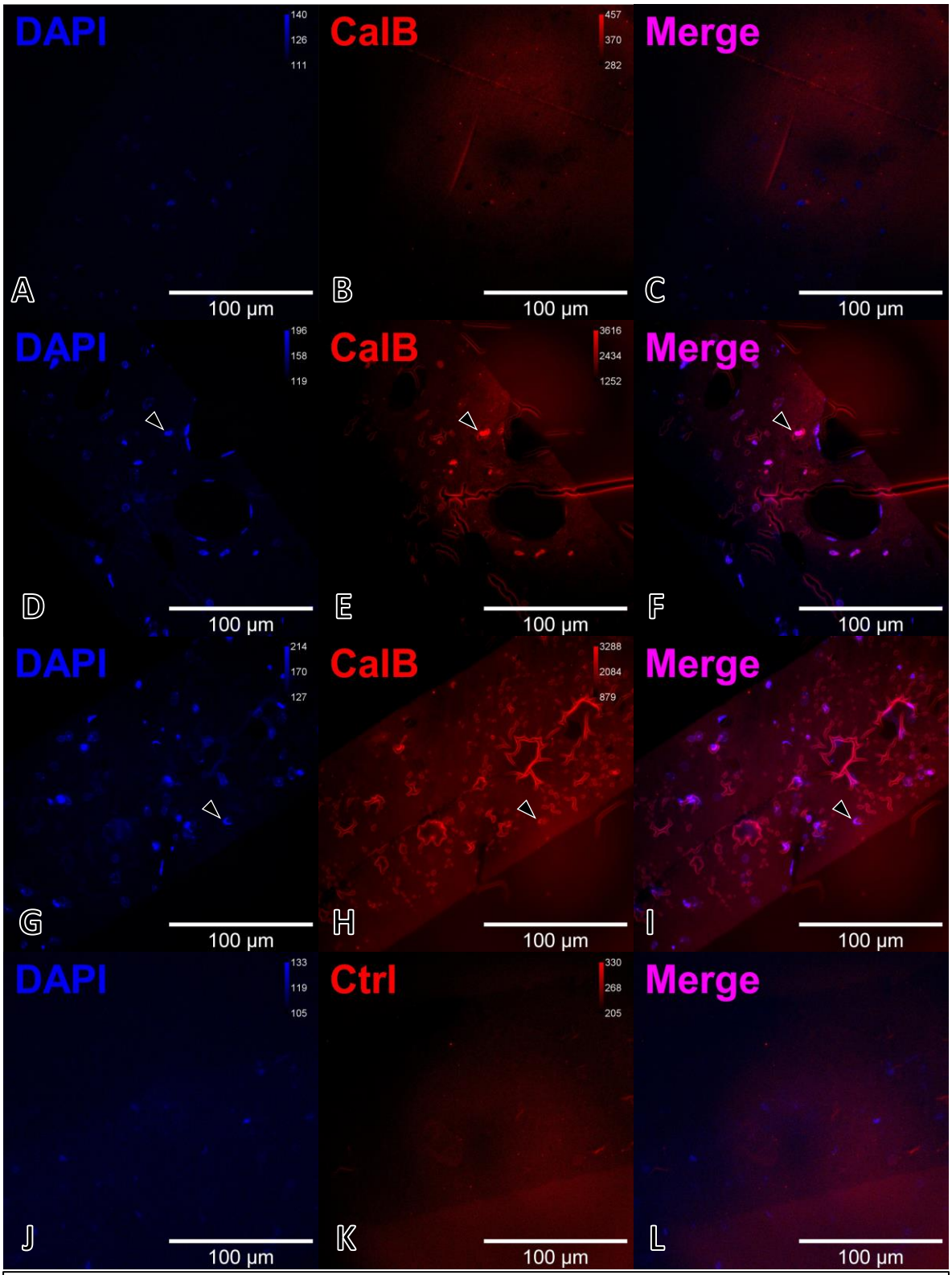

Figure 27. IF images of MGM-PIN 3 stained for calbindin (1:6000, *A – I*) compared to a control condition stained without primary antibody (*J – L*). This sample was micro-dissected and embedded into agarose prior to being embedded in LRW and sectioned at 250nm. Arrowheads indicate putative CalB^{+} nuclei. Note that we do not see any strongly labeled nuclei in the top row. Imaging credit: Alison Chase.

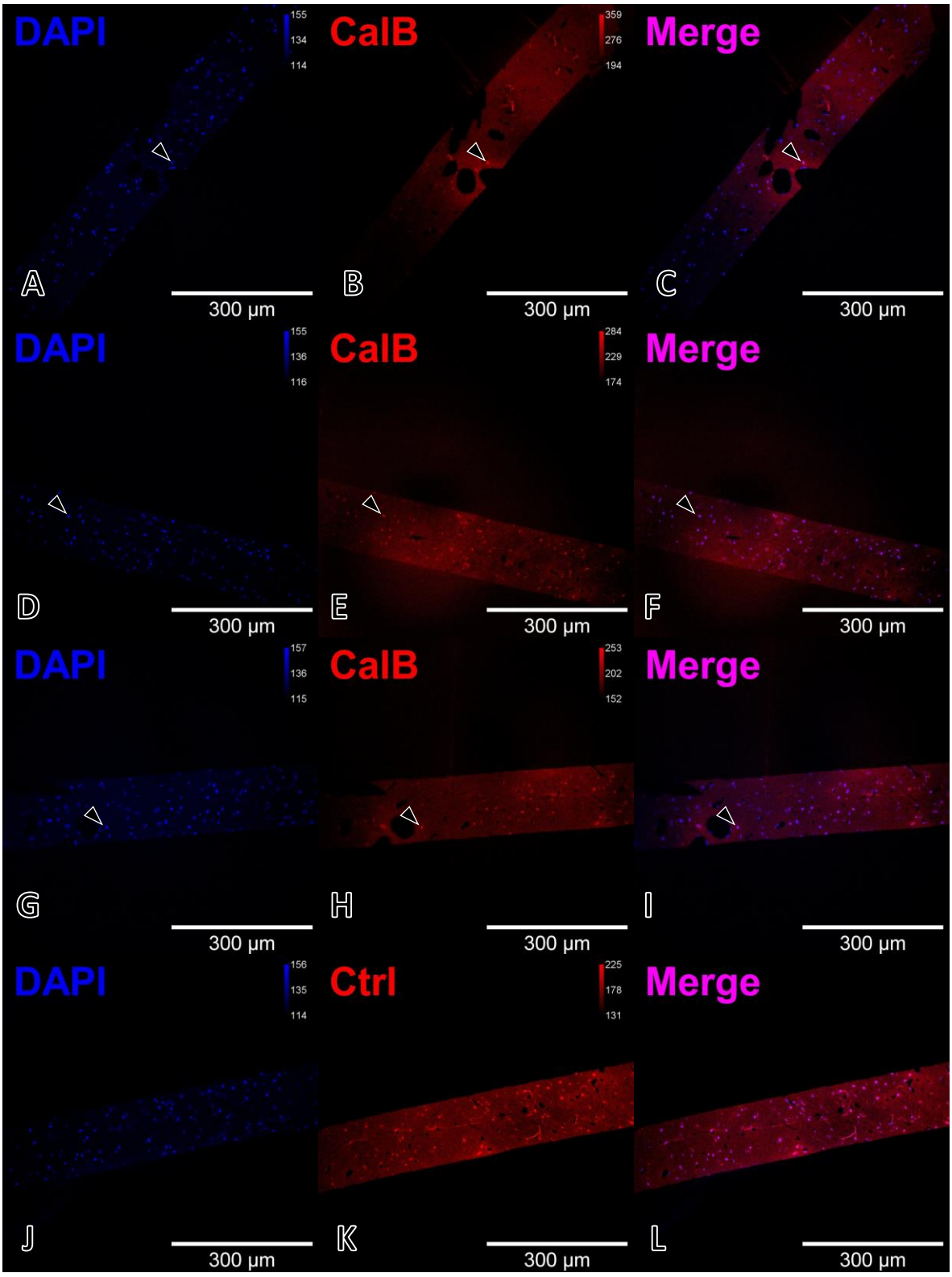

Figure 28. IF images of MGM-PIN 3 stained for calbindin (1:4000, *A – I*) compared to a control condition stained without primary antibody (*J – L*). This sample was micro-dissected and embedded into agarose prior to being embedded in LRW and sectioned at 250nm. Arrowheads indicate putative $CalB^{+}$ nuclei. Imaging credit: Alison Chase.

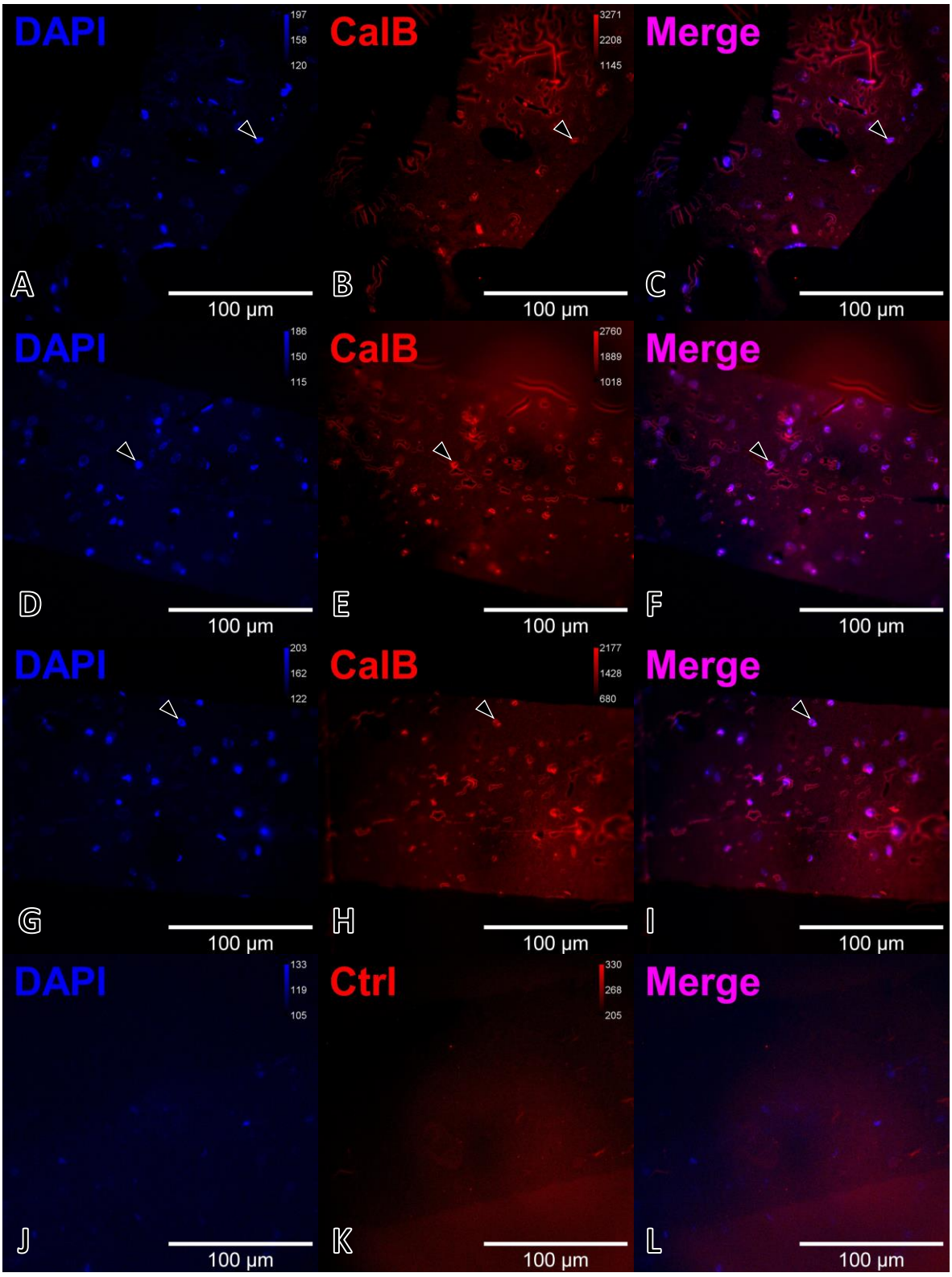

Figure 29. IF images of MGM-PIN 3 stained for calbindin (1:4000, *A – I*) compared to a control condition stained without primary antibody (*J – L*). This sample was micro-dissected and embedded into agarose prior to being embedded in LRW and sectioned at 250nm. Arrowheads indicate putative CalB^{+} nuclei. Imaging credit: Alison Chase.

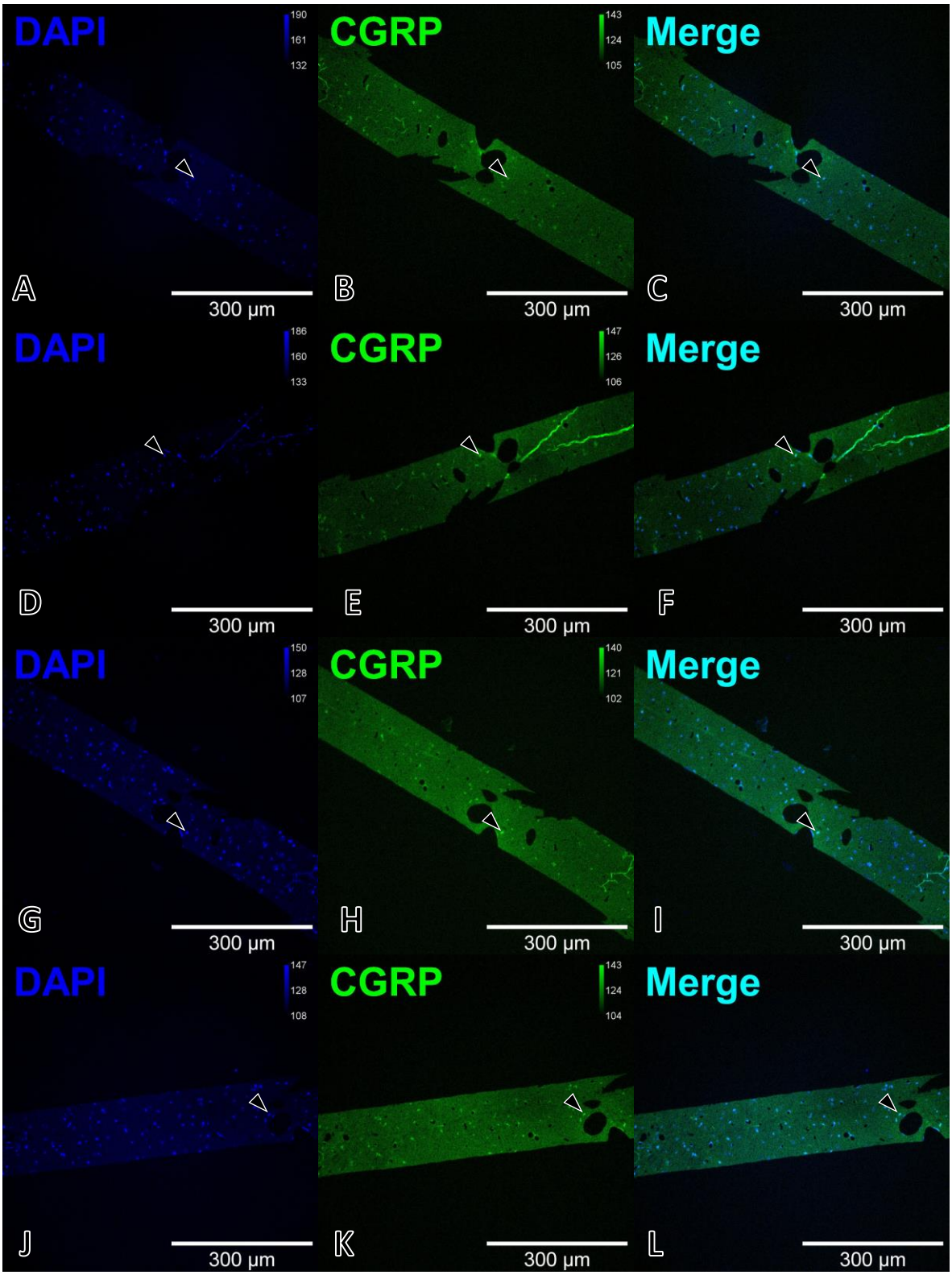

Figure 30. IF images of MGM-PIN 3 stained for CGRP (1:1000) on four non-consecutive serial sections (*A – C*; *D – F*; *G – I*; *J – L*). This sample was micro-dissected and embedded into agarose prior to being embedded in LRW and sectioned at 250nm. A control condition stained without primary antibody was run alongside this batch but was unable to be imaged in time. Arrowheads indicate putative CGRP$^+$ nuclei. Imaging credit: Alison Chase.

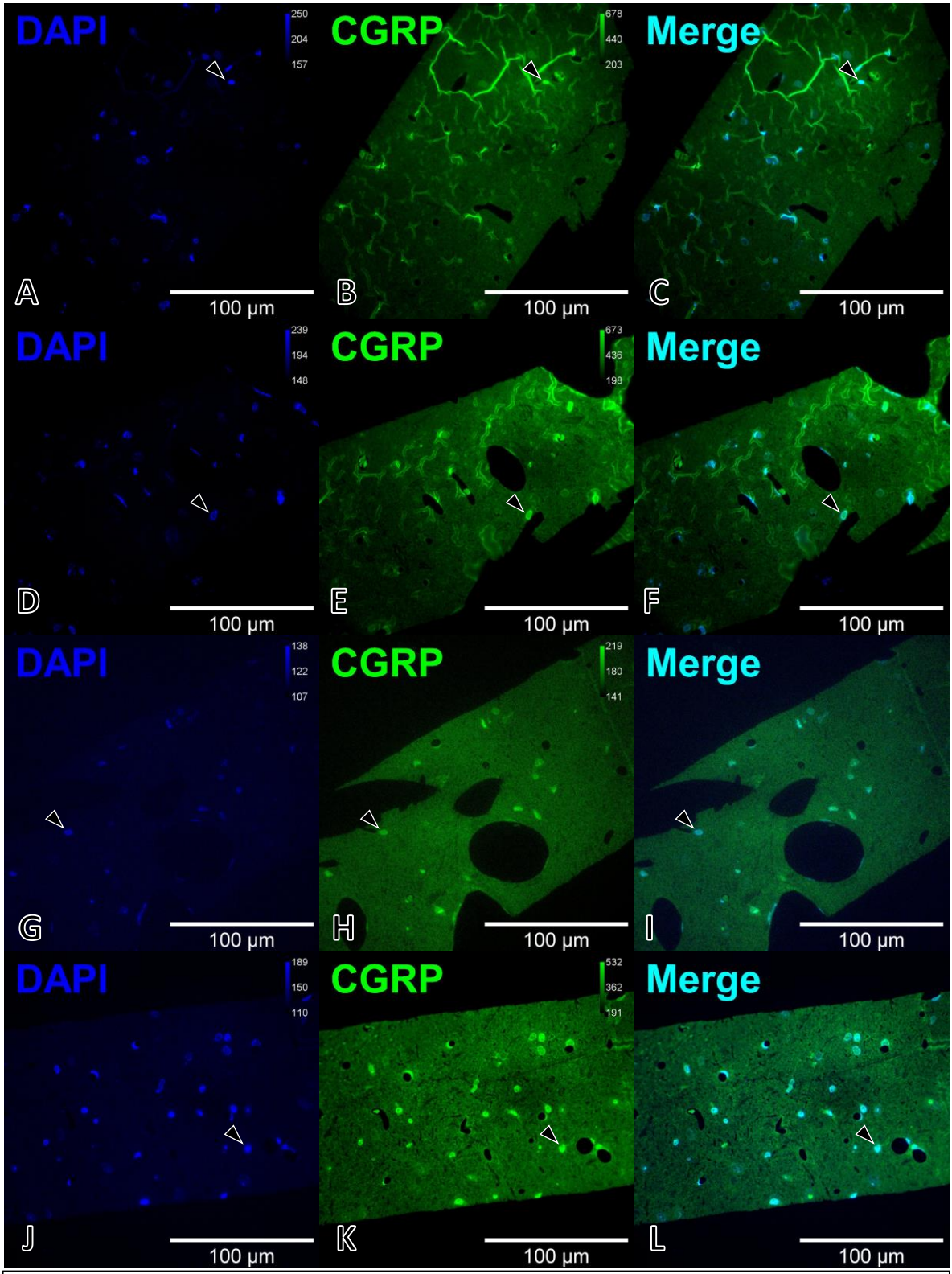

Figure 31. IF images of MGM-PIN 3 stained for CGRP (1:1000) on four non-consecutive serial sections (*A – C*; *D – F*; *G – I*; *J – L*). This sample was micro-dissected and embedded into agarose prior to being embedded in LRW and sectioned at 250nm. A control condition stained without primary antibody was run alongside this batch but was unable to be imaged in time. Arrowheads indicate putative $CGRP^{+}$ nuclei. Imaging credit: Alison Chase.

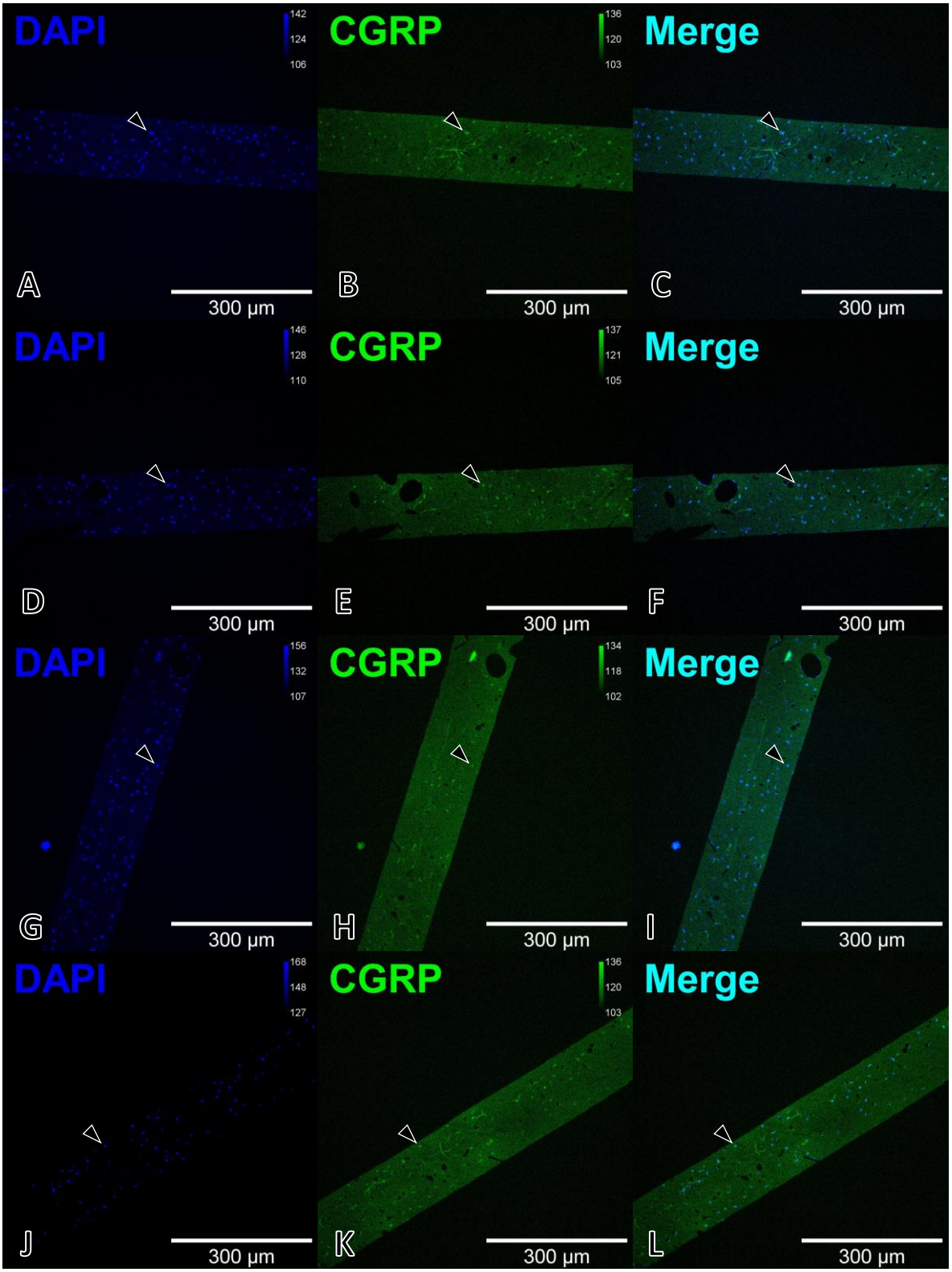

Figure 32. IF images of MGM-PIN 3 stained for CGRP (1:1000) on four non-consecutive serial sections (*A – C*; *D – F*; *G – I*; *J – L*). This sample was micro-dissected and embedded into agarose prior to being embedded in LRW and sectioned at 250nm. A control condition stained without primary antibody was run alongside this batch but was unable to be imaged in time. Arrowheads indicate putative $CGRP^{+}$ nuclei. Imaging credit: Alison Chase.

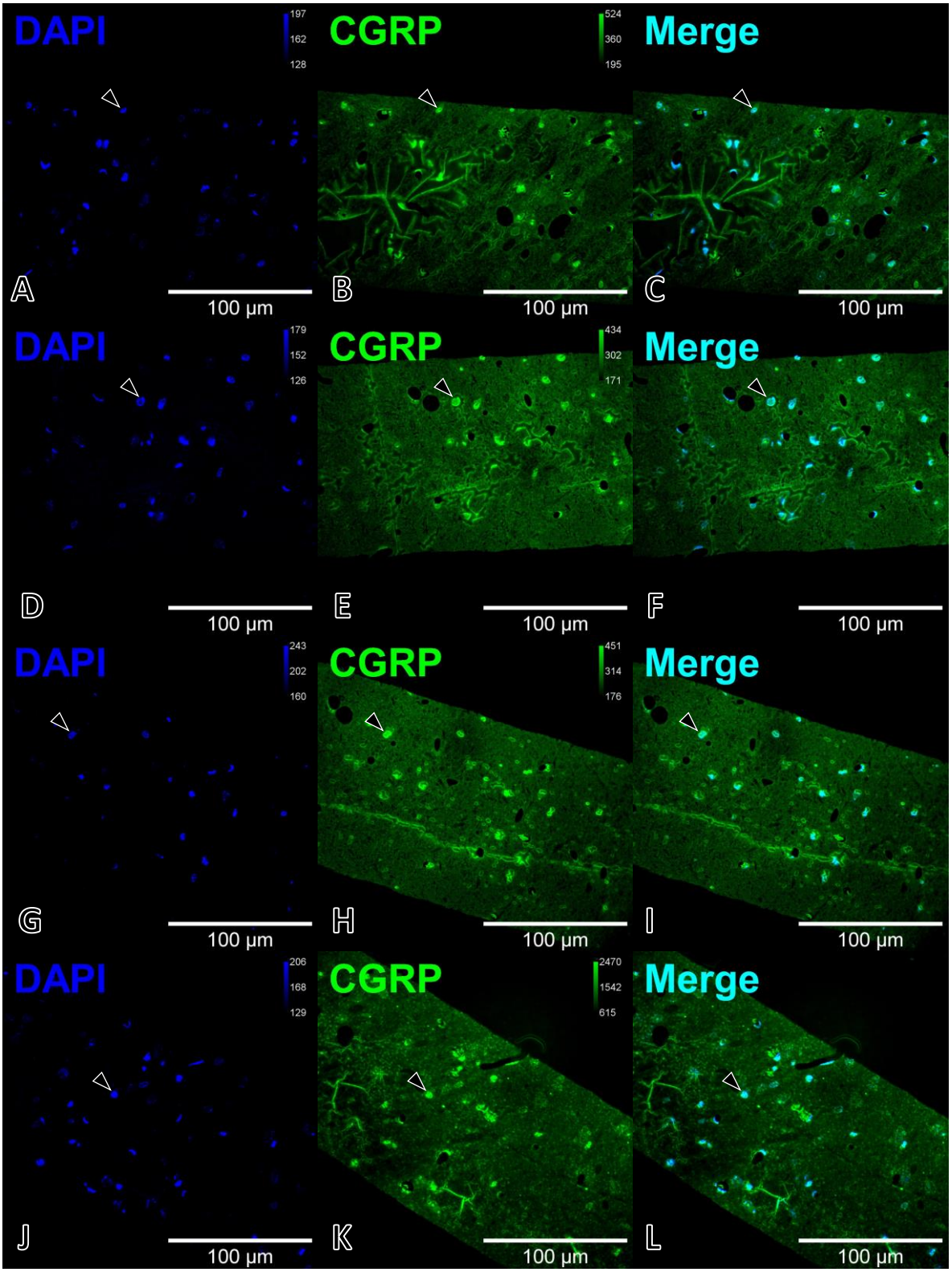

Figure 33. IF images of MGM-PIN 3 stained for CGRP (1:1000) on four non-consecutive serial sections (*A – C*; *D – F*; *G – I*; *J – L*). This sample was micro-dissected and embedded into agarose prior to being embedded in LRW and sectioned at 250nm. A control condition stained without primary antibody was run alongside this batch but was unable to be imaged in time. Arrowheads indicate putative $CGRP^{+}$ nuclei. Imaging credit: Alison Chase.

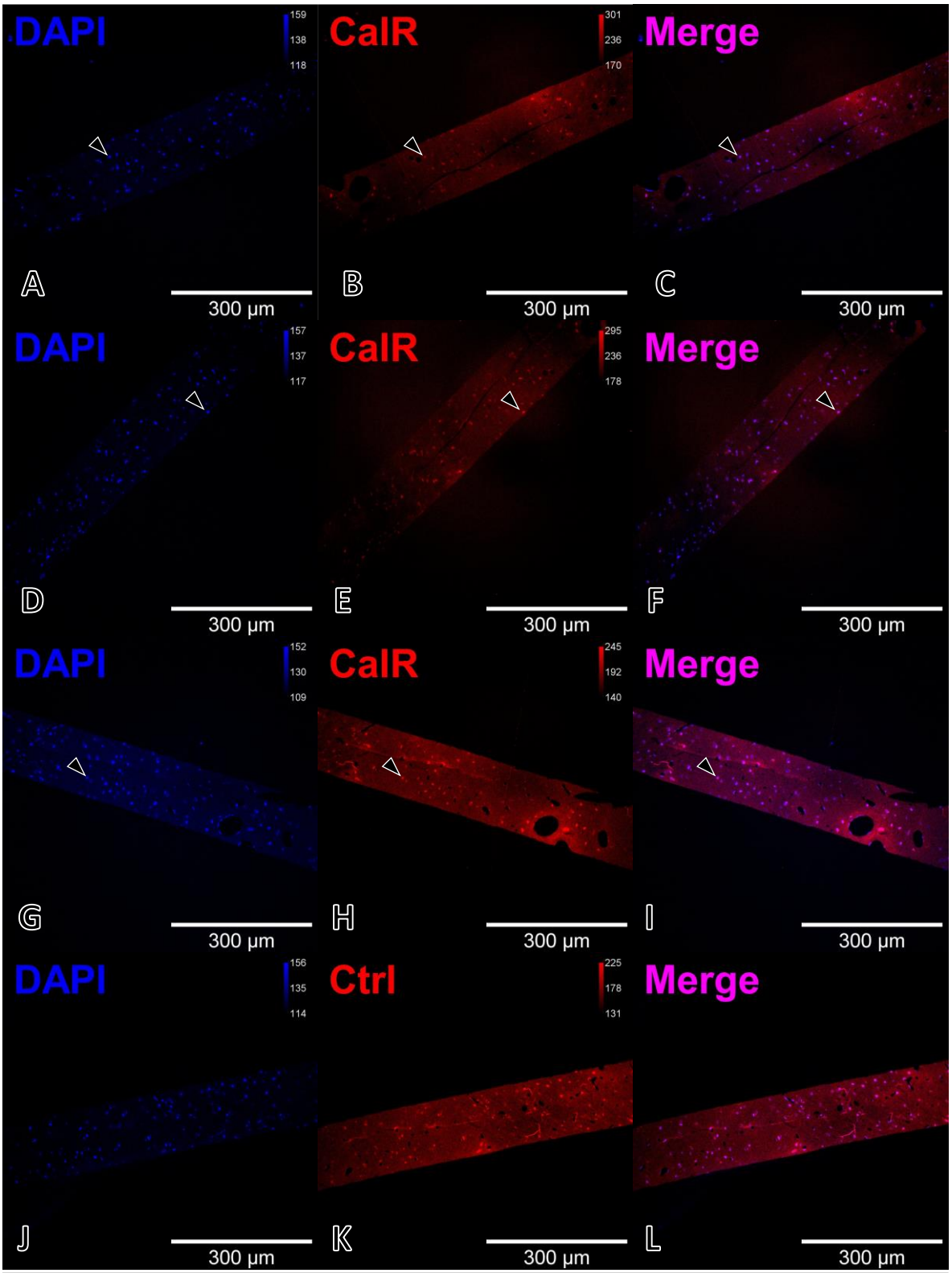

Figure 34. IF images of MGM-PIN 3 stained for calretinin (1:5000, *A – I*) compared to a control condition stained without primary antibody (*J – L*). This sample was micro-dissected and embedded into agarose prior to being embedded in LRW and sectioned at 250nm. Arrowheads indicate putative CalR^{+} nuclei. Imaging credit: Alison Chase.

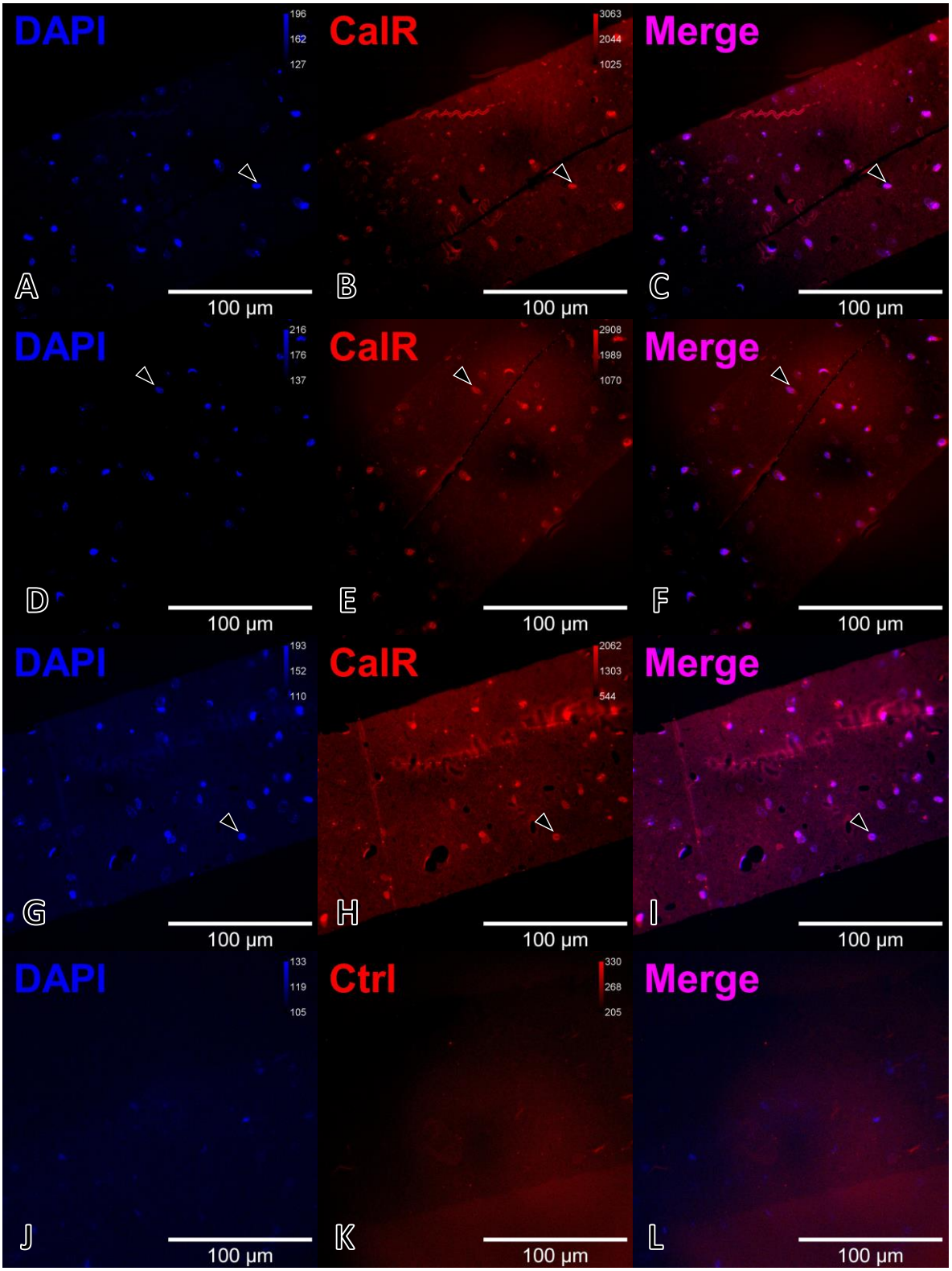

Figure 35. IF images of MGM-PIN 3 stained for calretinin (1:5000, *A – I*) compared to a control condition stained without primary antibody (*J – L*). This sample was micro-dissected and embedded into agarose prior to being embedded in LRW and sectioned at 250nm. Arrowheads indicate putative CalR^{+} nuclei. Imaging credit: Alison Chase.

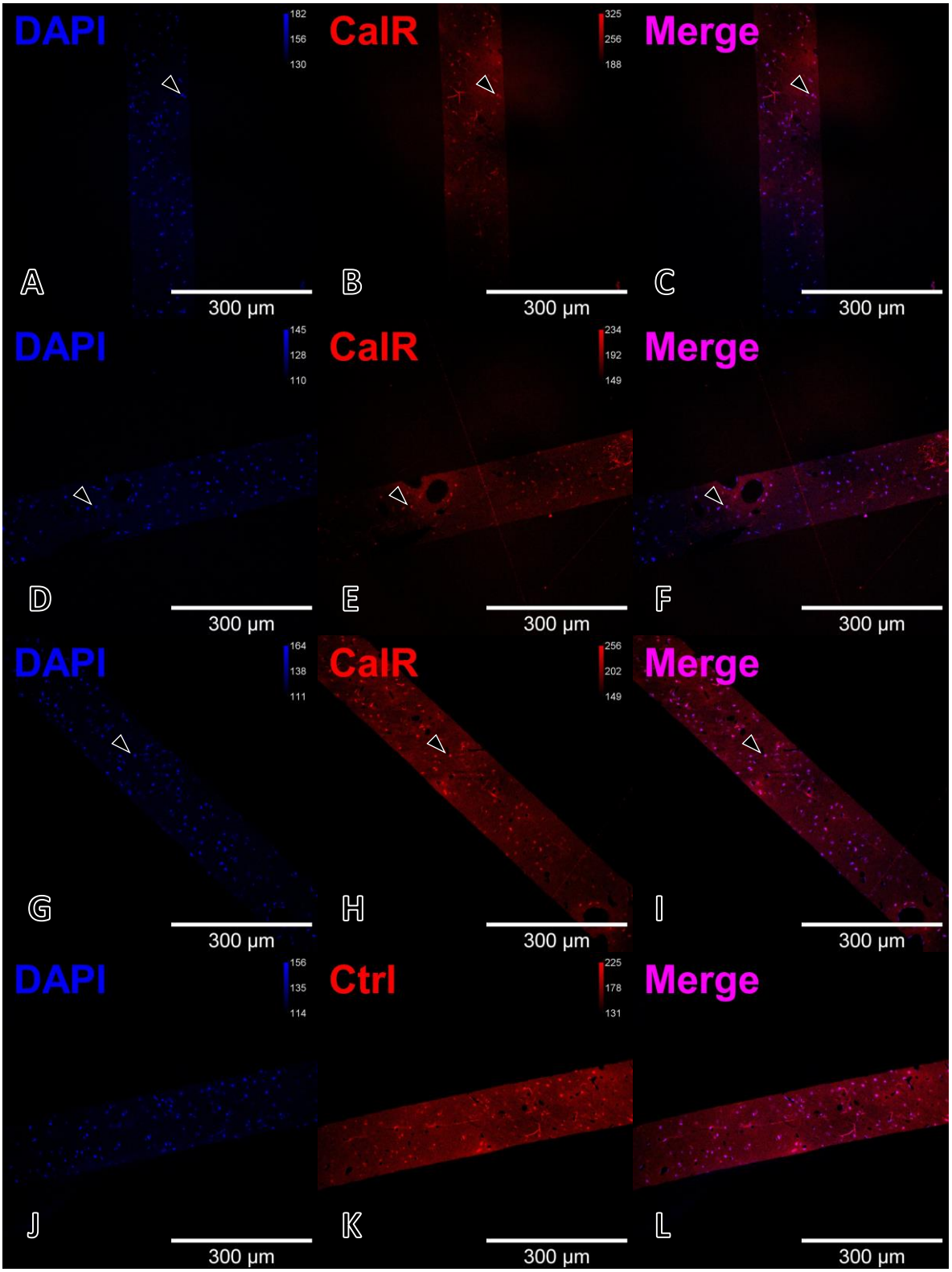

Figure 36. IF images of MGM-PIN 3 stained for calretinin (1:2500, *A – I*) compared to a control condition stained without primary antibody (*J – L*). This sample was micro-dissected and embedded into agarose prior to being embedded in LRW and sectioned at 250nm. Arrowheads indicate putative CalR^{+} nuclei. Imaging credit: Alison Chase.

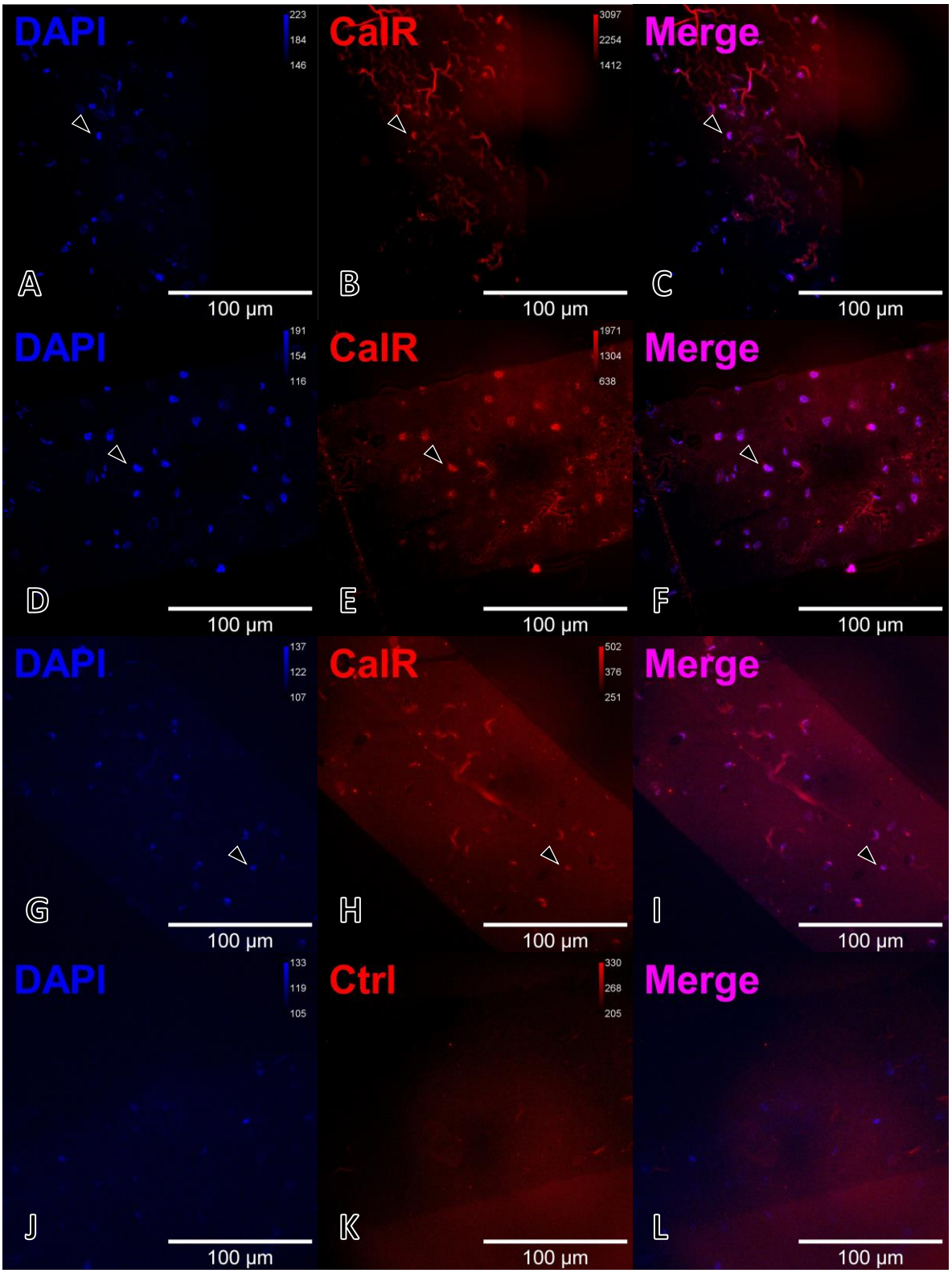

Figure 37. IF images of MGM-PIN 3 stained for calretinin (1:2500, *A – I*) compared to a control condition stained without primary antibody (*J – L*). This sample was micro-dissected and embedded into agarose prior to being embedded in LRW and sectioned at 250nm. Arrowheads indicate putative CalR^{+} nuclei. Imaging credit: Alison Chase.

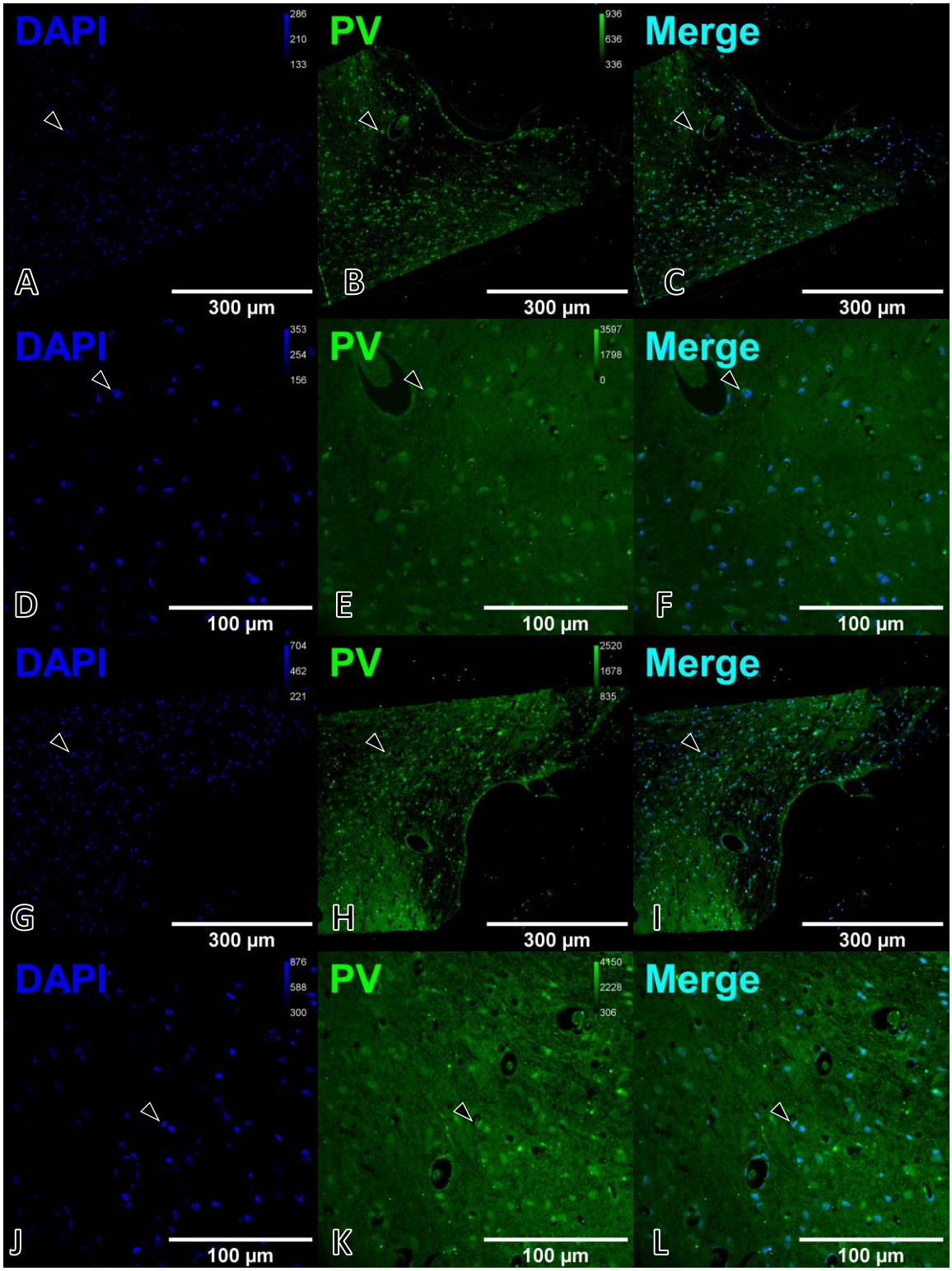

Figure 38. IF images of F.12.01G.1.P.b stained for parvalbumin (1:50) on two non-consecutive serial sections (*A – F*; *G – L*). This sample was fixed with 0.1% glutaraldehyde/4% PFA in 0.1M PB and was frozen without any fillers prior to being embedded in LRW and sectioned at 250nm. These sections were kept on subbed slides at -20°C for 12 days prior to IHC. A control condition stained without primary antibody was run alongside this batch but was unable to be imaged in time. Arrowheads indicate putative PV^{+} nuclei. Note that the top two rows label the same nuclei at different magnifications.

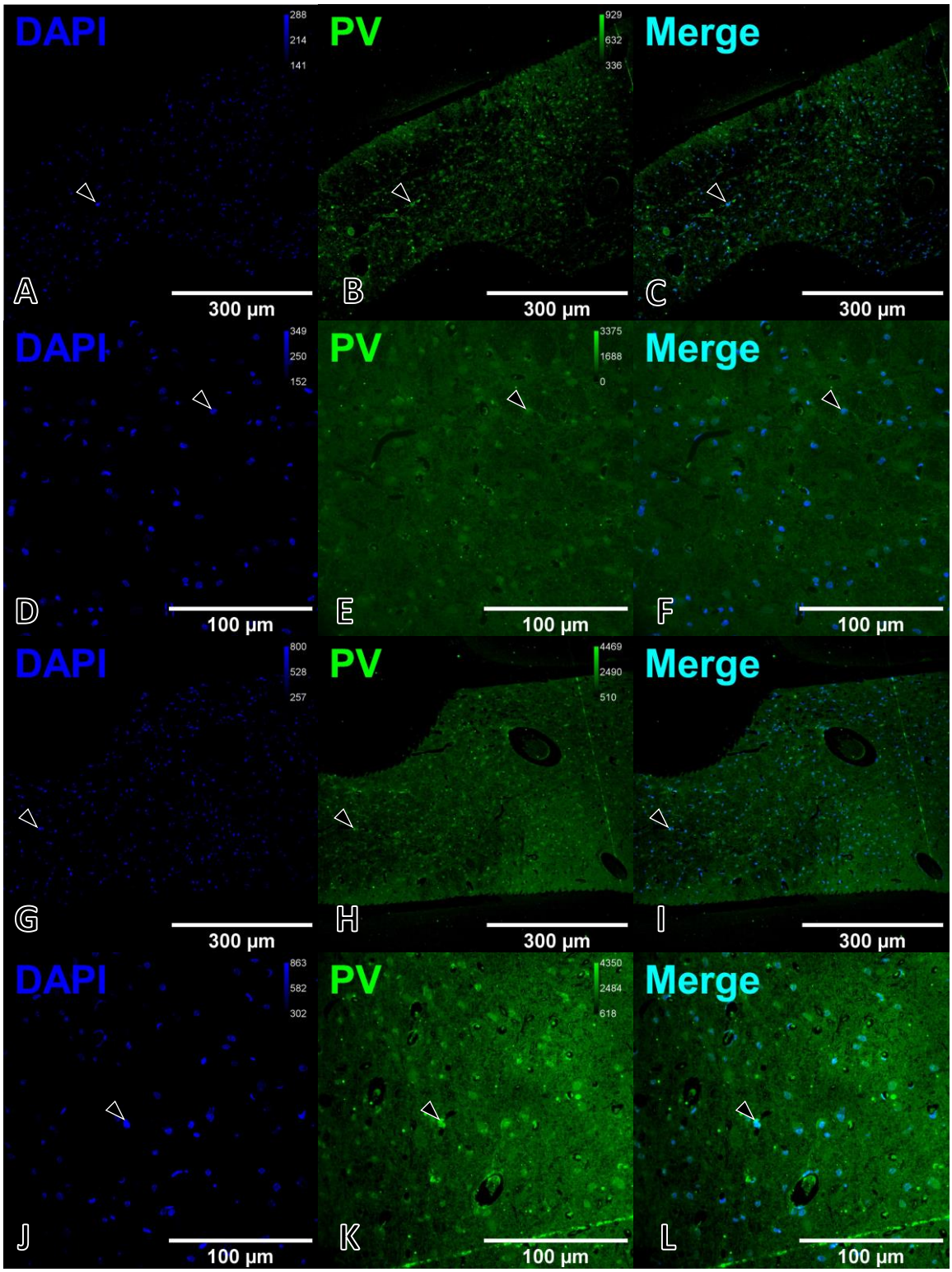

Figure 39. IF images of F.12.01G.1.P.b stained for parvalbumin (1:50) on two non-consecutive serial sections (*A – F*; *G – L*). This sample was fixed with 0.1% glutaraldehyde/4% PFA in 0.1M PB and was frozen without any fillers prior to being embedded in LRW and sectioned at 250nm. These sections were kept on subbed slides at -20°C for 12 days prior to IHC. A control condition stained without primary antibody was run alongside this batch but was unable to be imaged in time. Arrowheads indicate putative PV^{+} nuclei.

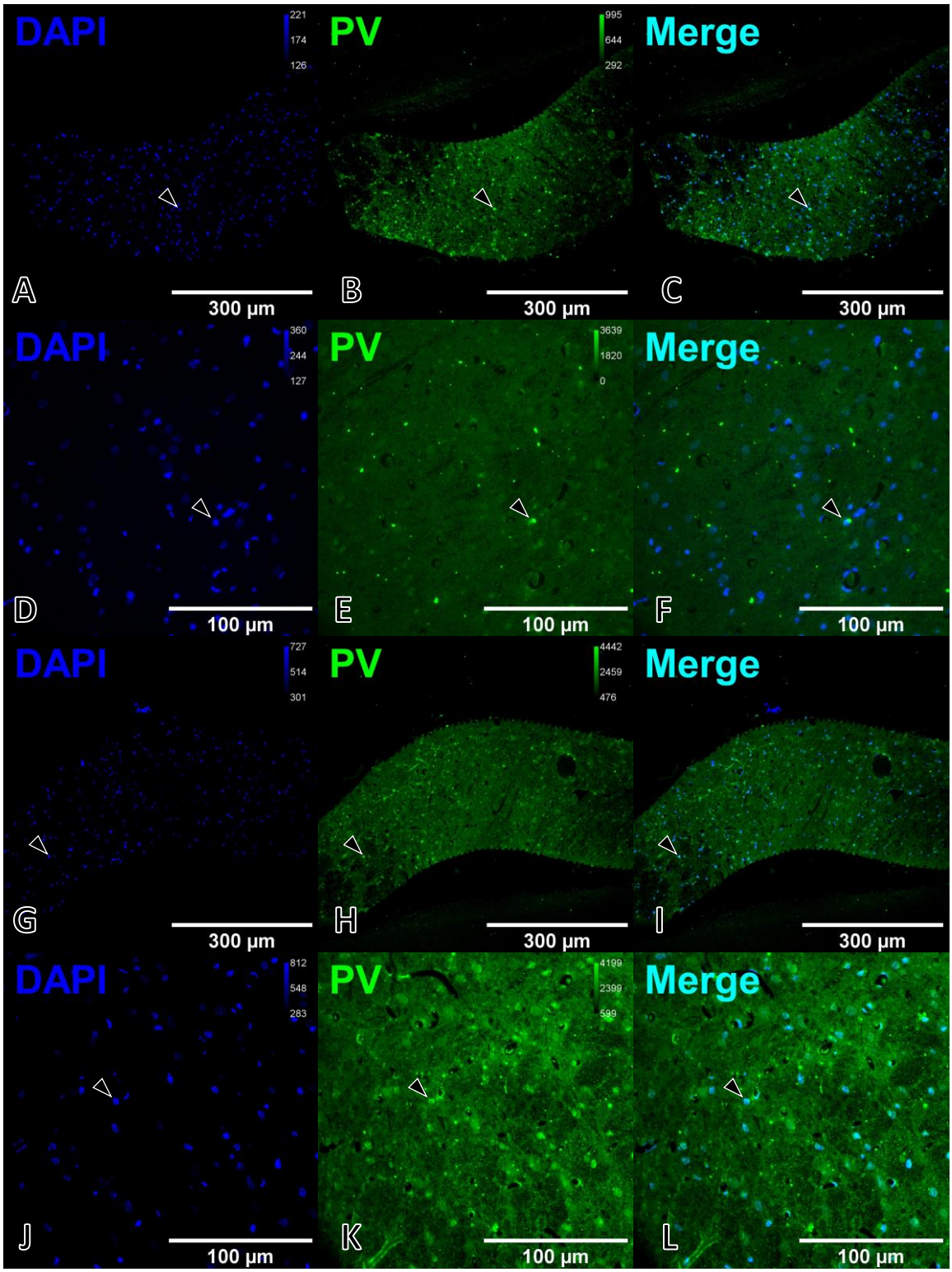

Figure 40. IF images of F.12.01G.1.P.b stained for parvalbumin (1:50) on two non-consecutive serial sections (*A – F*; *G – L*). This sample was fixed with 0.1% glutaraldehyde/4% PFA in 0.1M PB and was frozen without any fillers prior to being embedded in LRW and sectioned at 250nm. These sections were kept on subbed slides at -20°C for 12 days prior to IHC. A control condition stained without primary antibody was run alongside this batch but was unable to be imaged in time. Arrowheads indicate putative PV^{+} nuclei. Note that the top two rows label the same nuclei at different magnifications.

Part 3: Discussion

3.1 Summary of Findings

After testing the efficacy and practicality of the methods involved in processing samples for serial multiplexed electron microscopy labeling, we can draw some preliminary conclusions about what we have found. Beginning with fixation chemistry, we can see from our results that some fixatives work better than others at both structural and functional information preservation. We found that some of the more exotic fixatives, such as PBQ or acrolein, tended to produce sub-par results in terms of morphological preservation. However, we did find DMS to produce fixed tissue with intact membranes and well-preserved subcellular structures. It is difficult to say at this point whether DMS appears to be a superior fixative to the more traditional glutaraldehyde – PFA combinations, but it shows the most promise out of all the alternative fixes that we tested. Though we would have liked to test IHC on DMS fixed tissue and compare it directly to glutaraldehyde fixed tissue, we were not able to do so at the time of this writing.

We found high-pressure freezing to be an invaluable technique throughout this project, as it allowed us to collect many samples in a single day and store them indefinitely. From the HPF hat filling experiments, we found that using PVP without any BSA or other hydrocarbon produced the best results for us. We found that some samples would fracture at some point during post-HPF storage. By filling most of the space in the storage cryotube with a frozen organic solvent, we were able to mitigate this by reducing the volume in which the sample can move throughout.

A large portion of the time spent working on this project went towards working with the AFS for cryo-substitution and resins. We found that we achieved the best substitution results using samples contained within permeable baskets placed into a dish. Using this method, we were able to avoid physical contact between the pipet and the sample, while allowing the samples to move about freely in response to fluid currents. Although this requires an extra step when transitioning to resin embedding, we believe the advantages outweigh the downsides. We were able to achieve the best results from resin embedding

by using flat-embedding molds in conjunction with HM20. Though we only recently started testing MBA as a resin, we are optimistic about this as a possible substitution for LRW. MBA appeared to have the best sectioning properties out of the resins that we tested and showed promising IHC results. Though we were unable to achieve large amounts of serial sections for IHC, we tested several antibodies on different resins and on tissue preserved using different fixatives. From these results, we can conclude that some antibodies work better than others under different conditions including resin and fixative.

3.2 Future Directions

The framework discussed throughout this manuscript leaves several options available for future research to build upon. One unfinished area, antigen retrieval, appears to be a promising method. Antigen retrieval has been shown to rescue the immunogenicity of soluble and membrane-bound proteins in fixed tissue for electron microscopy (Brorson, 1998; Yamashita et al., 2009). We attempted similar methods with some of our samples but ran out of time before we could draw any meaningful conclusions. If we had more time, further exploring antigen retrieval could prove to be a fruitful endeavor given the current state of our IHC results. Another possible future direction includes utilizing electron energy loss spectroscopy (EELS) and energy dispersive X-ray spectroscopy (EDS). These methods allow the user to generate an elemental map of a sample based on differential energy levels of emitted electrons in response to the incident electron beam (Barfels et al., 1998). By doing so, one can generate pseudo-colorized images, showing localization of elements amongst the neuropil (Pirozzi et al., 2018; Scotuzzi et al., 2016) (Figure 41). This opens a wide array of opportunities and could possibly allow for the development of element-based labeling techniques in the future. We were able to perform EDS imaging for one of our samples, but the technology requires specialized instruments that are oftentimes unavailable or otherwise unusable. However, this technique remains one such area we would have liked to spend more time investigating, given additional time to do so.

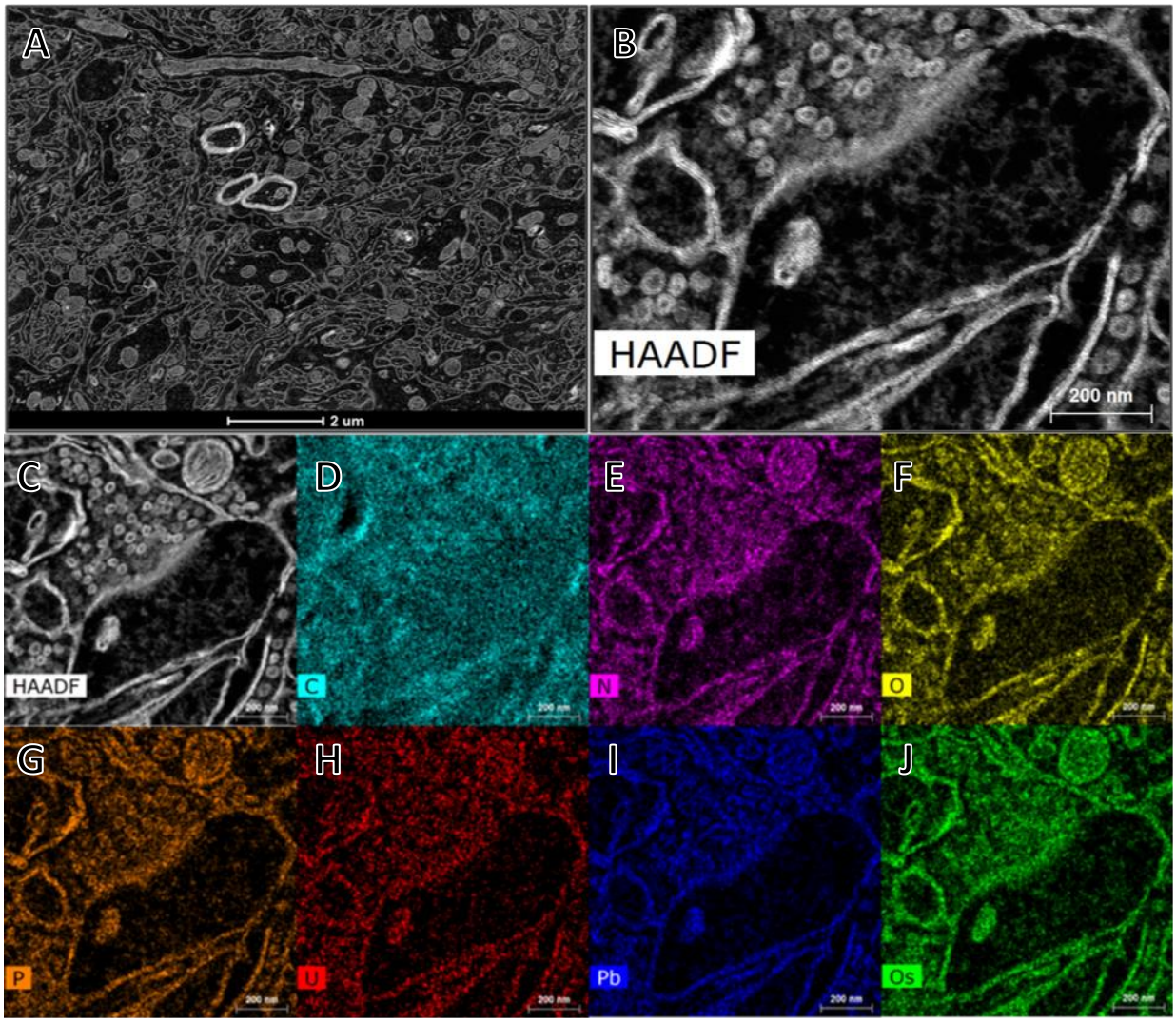

Figure 41. EDS Imaging of osmium-stained tissue. *A – C:* High Angle Annular Dark Field (HAADF) images. *D – J:* Elemental mapping of the same field from *C.* Note the element being shown in the lower left hand corner of each panel.

Lastly, there are some more immediate steps in the horizon for the results from this project. To achieve a truly serial multiplex labeled volume of brain tissue, the samples must be rotated in the TEM sample chamber using a rotational holder specimen rod. This rough aligns the sections to one another across multiple grids, thereby decreasing the amount of time spent digitally aligning them later. We were able to set up a rotational holder for our TEM and were able to verify that it works as expected by rotating a grid in the chamber. Given additional time, this would have been used for imaging with all our samples destined for volume reconstruction. After imaging, the next step to take is to use an image segmentation

software such as Reconstruct or VAST Lite to trace structures across serial sections and generate 3D volume reconstructions. By doing so, this would allow us to visualize ultrastructural information such as synaptic connections between cells (Figure 42). Several other possibilities are ripe for further experiments to be performed, and we are excited to see what other directions may be explored.

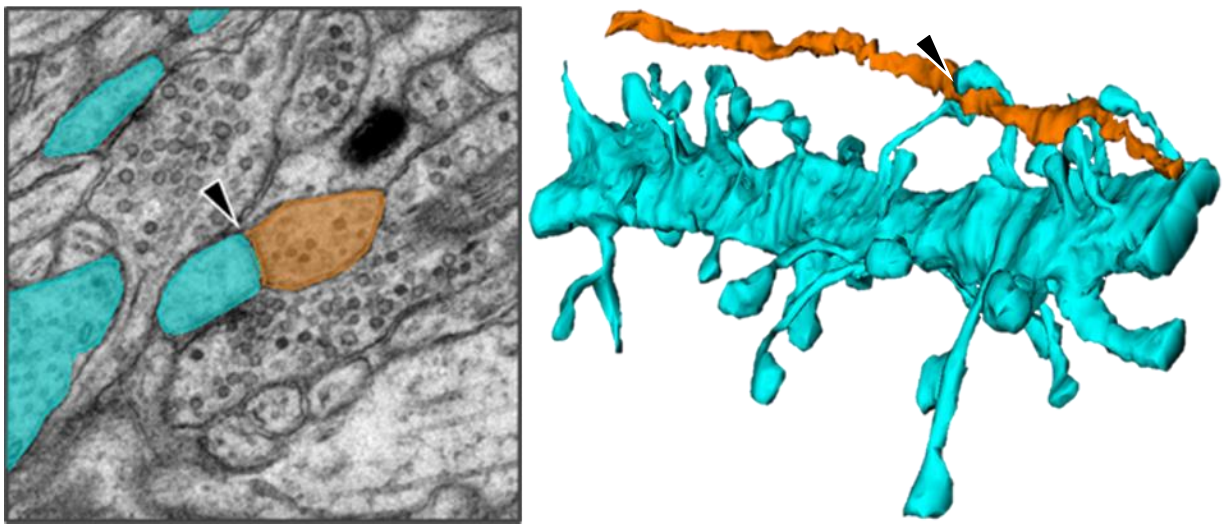

Figure 42. Future directions using Reconstruct. *Left:* A TEM image of a section of tissue in Reconstruct. Arrowhead indicates a synapse between a dendrite, shown in blue, with an axon, shown in orange. *Right:* A 3D volume reconstruction of serial sections in Reconstruct. Arrowhead indicates the same synapse shown on the left.

Part 4: Methods

4.1 Perfusion, Fixation, and Dissection

Animals discussed throughout this manuscript were Sprague-Dawley rats sourced from Hilltop and were roughly eight weeks old. All images displayed were from samples gathered from male rats. For fixative tests, some animals were females, though none of these samples were used for downstream processing. All perfusions were done via intracardial injection by Zachary Deane. Animals were perfused with one of the following fixatives: 0.1% glutaraldehyde/4% PFA 0.1M PB (n=6); 0.1% glutaraldehyde/4% PFA 0.1M PIPES (n=2); 2.5% glutaraldehyde/4% PFA 0.1M PB (n=3); 2.5% glutaraldehyde/4% PFA 0.1M PIPES (n=2); 2.5% glutaraldehyde/ 4% PFA in 0.1M Cacodylate buffer with 2mM CaCl2 & 4mM MgCl2

(n=3); 4% PFA in 0.1M Cacodylate buffer with 2mM CaCl2 & 4mM MgCl2 (n=2); 3.8% acrolein/2% PFA 0.1M PIPES with 2mM CaCl2 & 4mM MgCl2 (50mL); 2% PFA 0.1M PIPES with 2mM CaCl2 & 4mM MgCl2 (250mL) (n=12); 1.0% acrolein/0.5% glutaraldehyde/4% PFA (n=10); 3.8% acrolein/2% PFA 0.1M PB (n=1); 0.2% picric acid/0.5% glutaraldehyde/4% PFA 0.1M PB (n=2); 2% picric acid/4% PFA/0.05% glutaraldehyde 0.1M PB (n=1); 2% lysine/0.37% PFA/0.3% sodium periodate (n=2); 2% lysine/0.37% PFA/0.3% sodium periodate with glutaraldehyde (n=1); 0.5% Dimethyl suberimidate/4% PFA in 0.1M PB (n=2); or Saturated (<1%) Parabenzoquinone/4% PFA in 0.1M PB (n=3).

After perfusion, brains were dissected and placed in perfusate for 1-2h. Some brains were further processed on the same day as perfusion and some were left overnight in the buffer solution used in the perfusate. Brains were cut on a Leica vibratome at 100-200µm. Sections cut on the vibratome were placed in respective buffer solutions throughout additional tissue processing. Regions of interest were dissected out of vibratome sections using 2mm and 4mm biopsy punches and were then notched using a scalpel to aid in sample orientation. Some samples were then micro-dissected into thin strips of tissue using a scalpel blade and embedded at a specific thickness into low melting temperature agarose. These samples were then dissected out of the surrounding agarose using a biopsy punch.

4.2 High-Pressure Freezing and Sample Storage

High-pressure freezing of 100-200µm thick biopsy punched samples was performed using an HPF Compact 03 machine using factory settings. Samples were placed into aluminum dishes from Wohlwend prior to being inserted into the machine using a sample rod. Samples were frozen with one of the following conditions: 20% BSA with hexadecene (n=324); 20% BSA with isooctane (n=65); 20% Ficoll with hexadecene (n=6); 20% PVP with hexadecene (n=51); 20% PVP (n=30); hexadecene only (n=2); or without any fillers (n=21). Immediately after freezing, samples were transferred to liquid nitrogen where the dishes were removed from each other. The majority of samples were then stored in cryotubes filled with

liquid nitrogen and were kept in dewars for long term storage. Some samples were stored in cryotubes containing either 100% ethanol (frozen) or 100% acetone (frozen). A small number of samples were not stored in liquid nitrogen and were processed immediately after freezing.

4.3 Substitution, Infiltration, and Embedding

All samples were substituted using a Leica EM AFS-2 for 48-68 hours at -90°C. Samples were substituted using one of the following conditions: 1% uranyl acetate in acetone (n=109); 100% ethanol (n=39); 100% acetone (n=7); 1% tannic acid in acetone (n=4); or 0.1% tannic acid in acetone (n=2). After substitution, samples were warmed to one of the following temperatures at 5°C/h for infiltration: -55°C for HM20 and K11M (n=57); 22°C for LRW and MBA (n=39); or -30°C for K4M (n=55). Substitution media were removed from the samples prior to infiltration using a series of 3-7 rinses in 100% acetone or 100% ethanol. Resins were then made following protocols established by Electron Microscopy Sciences.

For HM20, samples were infiltrated for 3 hours in a 1:1 mixture of HM20 to acetone followed by 3 hours in a 2:1 mixture of HM20 to acetone and then overnight in 100% HM20. The following day, samples were infiltrated for 1 hour in freshly made 100% HM20 prior to embedding. For K4M, samples were infiltrated for 3 hours in a 1:1 mixture of K4M to acetone followed by 3 hours in a 2:1 mixture of k4M to acetone and then overnight in 100% K4M. The following day, samples were infiltrated for 1 hour in freshly made K4M prior to embedding. For K11M, samples were infiltrated for 3 hours in a 1:1 mixture of K11M to acetone followed by 3 hours in a 2:1 mixture of K11M to acetone and then overnight in 100% K11M. The following day, samples were infiltrated for 1 hour in freshly made 100% K11M prior to embedding. For LR White, some samples were infiltrated for 1 hour in a 1:1 mixture of LRW to ethanol followed by 1 hour in a 2:1 mixture of LRW to ethanol and then 1 hour in 100% LRW prior to embedding. Some samples were infiltrated in a Pelco microwave and some were infiltrated at RT. For MBA, samples were infiltrated in a Pelco microwave.

Next, samples were embedded into their appropriate resins based on what was used during the infiltration process. HM20 samples were UV cured in the AFS for 48 hours at -55°C, then raised to 22°C over 14 hours followed by 72 hours at 22°C. K11M samples were UV cured in the AFS using the same protocol for HM20. K4M samples were UV cured in the AFS for 48 hours at -30°C then raised to 22°C over 14 hours followed by 72 hours at 22°C. LR White samples were embedded in 100% LRW and cured in an oven set to hold at 65°C for 48 hours. MBA samples were embedded in 100% MBA and UV cured in the AFS for 48 hours at 4°C. LR White and MBA samples were embedded in gelatin capsules. HM20, K4M, and K11M samples were embedded in either flat-embedding molds or flow-through tubes. When using flat-embedding molds, an Aclar cover was fitted and cut to prevent air from reaching the samples. Samples embedded in flat-embedding molds were infiltrated in either cryotubes or mesh baskets. Samples embedded in flow-through tubes were infiltrated in flow-through tubes. Samples embedded in gelatin capsules were infiltrated in either cryotubes or glass shell vials.

4.4 Sectioning and Grid Handling

Post-embedded sectioning was done using either a Leica UC-7 ultramicrotome or a Leica UCT ultramicrotome. Rough trimming of blocks was done by hand using a single edge razor. Fine trimming for serial sectioning was done using the ultramicrotome and a diamond trim tool supplied by DiATOME. Thick sections were cut using glass knives made from glass supplied by Electron Microscopy Sciences. Thin sections were cut using Histo- or Ultra-quality diamond knives supplied from DiATOME. Diamond knives and glass knives used for section pickup had boats attached to them. Knife boats held one of the following: 100% RO water; 100% RO water with 1% Photo-Flo; 100% RO water with 0.1% Tween-20; or 100% RO water with 0.01% Tween-20. Sections were cut at 0.9 – 1.4 mm/s depending on the resin.

Sections were picked up using eyelash tools or cat whisker tools made on site or by perfect loop tools supplied by Electron Microscopy Sciences. Sections stained for Toluidine Blue or Methylene Blue –

Azure II were cut between 100 – 500nm thickness and stained on either gelatin coated slides, plain glass slides, or plasma cleaned slides. Sections stained for IF imaging were picked up on gelatin coated slides or plasma cleaned slides and were cut between 100 – 250nm in thickness. Sections viewed in the EM and stained using EM IHC protocols were cut between 40 – 50nm in thickness. These were picked up on either copper mesh grids or gold slot grids coated with either pioloform or polystyrene. Grids coated with polystyrene were plasma cleaned for 10 sections at low power using a plasma cleaner. Mesh grids and slot grids coated with pioloform were not plasma cleaned.

Mesh grids and bare slot grids were supplied by Electron Microscopy Sciences. Slot grids were coated with either pioloform or polystyrene using a film caster supplied by Electron Microscopy Sciences. A 1% solution of pioloform in chloroform or a 1% solution of polystyrene in toluene were prepared several days prior to being used in the film caster. Some Fisher SuperFrost and GoldSeal slides were plasma cleaned and some were not before having the film applied to them. Silicon wafers obtained from University Wafer Incorporated were also used. Using a razor blade, coated slides and wafers were scored before being submerged into 100% RO water. Grids were then placed notch side up onto floating films and then collected onto parafilm-covered SuperFrost slides for storage.

4.5 Immunohistochemistry

Immunohistochemistry for light microscopy was performed on gelatin coated slides or plasma cleaned subbed slides. Sections were surrounded with a hydrophobic barrier prior to performing IHC. Sections were blocked for 45 minutes in a 1% BSA solution with 0.1% Tween-20 in 0.1M PBS at pH 7.4 with gentle agitation. After blocking, slides were rinsed in 3 changes of 0.1M PBS for 3-5 minutes each. Primary antibodies supplied by Synaptic Systems were diluted to varying degrees in 1% BSA with 0.1% Tween-20 in 0.1M PBS. Primary incubations lasted either 1.5-2 hours with gentle agitation or overnight in a sealed humid chamber at 4°C. Slides were rinsed prior to being incubated with secondary antibodies. Fluorescent

secondary antibodies provided by Invitrogen were diluted to 1:200 in 1% BSA solution with 0.1% Tween-20 in 0.1M PBS and applied to the sections for 45 minutes in darkness with gentle agitation. Slides were then rinsed in PBS and cover-slipped using Prolong Gold before being stored for imaging.

IHC for electron microscopy was performed on grids either in petri dishes, floating on droplets, or in pipet tips. Grids were etched with 1% sodium metaperiodate, rinsed in water, then etched with 1 minute then 1% periodic acid for 1 minute before another rinse with water. A blocking buffer consisting of 0.0M Tris base, 0.009 g/mL NaCl, 0.1% Tween-20, 1% BSA, 0.05% melted cold water fish skin gelatin (CWFSG), and 0.05M glycine in water was applied for 30-60 minutes. Grids were then rinsed in 3 changes of incubation buffer consisting of 0.0M Tris base, 0.009 g/mL NaCl, 0.1% Tween-20 and 1% BSA in water for 5 minutes each. Next, a primary antibody incubation of primary antibodies provided by Synaptic Systems at varying dilutions was in blocking buffer without the glycine was applied. Primary incubations were done either for 1-2 hours with gentle agitation at room temperature, or overnight in a sealed humid chamber at 4°C. Grids were then rinsed in incubation buffer.

A tris buffer was made consisting of 0.05M Tris base and 0.009 g/mL NaCl in water and was set to a pH of 7.4. Biotinylated secondary antibodies obtained from Thermo Scientific were diluted to 1:200 to in incubation buffer with 0.05% CWFSG. After rinsing in incubation buffer, streptavidin-conjugated quantum dots obtained from Thermo Scientific were diluted to 1:400 in incubation buffer and applied for 30-45 minutes at room temperature with gentle agitation. After a rinse in incubation buffer, Tris buffer, and PBS, some grids underwent an antigen retrieval step of 2% glutaraldehyde in 0.1M PBS being diluted into 0.1M PB applied for 10 minutes. Next, grids were rinsed in PBS and then in water. Grids that did not undergo the antigen retrieval step were rinsed in water. Grids were then either imaged or stained for enhanced contrast. Grids that underwent this staining were stained with 2% aqueous uranyl acetate for 3-5 minutes in darkness at room temperature. After 3 5-minute rinses in water, they were then stained

with aqueous lead citrate and sodium hydroxide for 5 minutes. Following several rinses in water, these grids would then be stored and imaged.

4.6 Imaging

All transmission electron microscopy was done using a JEOL JEM 1400 TEM on site or an FEI Talos TEM for EDS imaging. Images were taken using an AMT camera for the JEOL microscope. Prior to TEM imaging on the JEOL, electron beam alignment would be performed by the user. Grids were placed sample side up into the sample rod before being inserted into the vacuum chamber. Most of the samples imaged using TEM were stored for at least one hour after final IHC rinses and before imaging. All IF images shown were imaged on an Andor-IQ system using Nikon optics. Slides were placed cover-slip side down after being cleaned with 70% ethanol and water. Most of the samples imaged using IF were stored for at least one day after cover-slipping and before imaging. Images stained for Toluidine Blue and Methylene Blue – Azure II were imaged on a compound microscope using an attached DSLR camera. These slides were not cover-slipped and were imaged immediately after sectioning.

Conclusions

This manuscript explains the application and refinement of a variety of EM methods required for performing serial multiplexed immunolabeling of brain tissue for electron microscopy. We found that certain methods work better than others, and that some techniques are not worth pursuing. We discussed our experience with fine-tuning most of the steps involved in this process, beginning with testing alternative fixatives, and finishing with testing antibodies under varying conditions. We showed promising results from some lesser-known fixatives and resins, and showed that some antibodies will only work on some resins. Throughout this project, we found sample orientation to be much more important than we originally thought at the beginning. Though this slowed the pace of our progress down, we were able to

design protocols to address this issue. Given circumstances beyond our control, we were not able to collect as much data as we had hoped for. However, we realize that the work shown here reflects only a relatively short period of time. As a result, many future directions remain open for the results of this project. With further optimizations and tweaks to the protocols discussed here, we are confident that serial multiplex labeling will allow for the acquisition of a highly annotated volume reconstruction of brain tissue in the near future.

References

Barfels, M.M., Jiang, X., Heng, Y.M., Arsenault, A.L., & Ottensmeyer, F.P. (1998). Low energy loss electron microscopy of chromophores. *Micron, 29*(2-3), 97-104. https://doi.org/10.1016/s0968-4328(98)00009-2

Birrell, G.B., Hedberg, K.K., & Griffith, O.H. (1987). Pitfalls of immunogold labeling: analysis by light microscopy, transmission electron microscopy, and photoelectron microscopy. *The Journal of Histochemistry and Cytochemistry, 35*(8), 843-853. https://doi.org/10.1177/35.8.2439584

Boatman, J.A., & Kim, J.J. (2006). A thalamo-cortico-amygdala pathway mediates auditory fear conditioning in the intact brain. *The European Journal of Neuroscience, 24*(3), 894-900. https://doi.org/10.1111/j.1460-9568.2006.04965.x

Bonn, M., Schmitt, A., Lesch, K.P., Van Bockstaele, E.J., & Asan, E. (2013). Serotonergic innervation and serotonin receptor expression of NPY-producing neurons in the rat lateral and basolateral amygdaloid nuclei. *Brain Structure and Function, 218*(2), 421-435. https://doi.org/10.1007/s00429-012-0406-5

Briggman, K.L., & Bock, D.D. (2012). Volume electron microscopy for neuronal circuit reconstruction. *Current Opinion in Neurobiology, 22*(1), 154-161. https://doi.org/10.1016/j.conb.2011.10.022

Brorson, S.H. (1998). The combination of high-accelerator epoxy resin and antigen retrieval to obtain more intense immunolabeling on epoxy sections than on LR-white sections for large proteins. *Micron, 29*(2-3), 89-95. https://doi.org/10.1016/s0968-4328(98)00010-9

Buccino, A.P., Ness, T.V., Einevoll, G.T., Cauwenberghs, G., & Hafliger, P.D. (2018). A Deep Learning Approach for the Classification of Neuronal Cell Types. *Annual International Conference of the IEEE Engineering in Medicine and Biology Society, 2018*, 999-1002. https://doi.org/10.1109/EMBC.2018.8512498

Bu'Lock, A.J., Vaillant, C., Dockray, G.J., & Bu'Lock, J.D. (1982). A rational approach to the fixation of peptidergic nerve cell bodies in the gut using parabenzoquinone. *Histochemistry, 74*(1), 49-55. https://doi.org/10.1007/bf00495051

Buser, C., & Walther, P. (2008). Freeze-substitution: the addition of water to polar solvents enhances the retention of structure and acts at temperatures around -60°C. *Journal of Microscopy, 230*(Pt 2), 268-277. https://doi.org/10.1111/j.1365-2818.2008.01984.x

Butler, R.K., White, L.C., Frederick-Duus, D., Kaigler, K.F., Fadel, J.R., & Wilson, M.A. (2012). Comparison of the activation of somatostatin- and neuropeptide Y-containing neuronal populations of the rat amygdala following two different anxiogenic stressors. *Experimental Neurology, 238*(1), 52-63. https://doi.org/10.1016/j.expneurol.2012.08.002

Chung, L., & Moore, S.D. (2007). Cholecystokinin enhances GABAergic inhibitory transmission in basolateral amygdala. *Neuropeptides, 41*(6), 453-463. https://doi.org/10.1016/j.npep.2007.08.001

Chung, L., & Moore, S.D. (2009a). Cholecystokinin excites interneurons in rat basolateral amygdala. *Journal of Neurophysiology, 102*(1), 272-284. https://doi.org/10.1152/jn.90769.2008

Chung, L., & Moore, S.D. (2009b). Neuropeptides modulate compound postsynaptic potentials in basolateral amygdala. *Neuroscience, 164*(4), 1389-1397. https://doi.org/10.1016/j.neuroscience.2009.09.061

Corcoran, D., & Walker, R.A. (1990). Post embedding immunoelectron microscopy of human breast cancer: a comparison of three acrylic resins. *The Histochemical Journal, 22*(5), 291-298.

De Roe, C., Courtoy, P.J., & Baudhuin, P. (1987). A Model of Protein-Colloidal Gold Interactions. *The Journal of Histochemistry and Cytochemistry, 35*(11), 1191-1198. https://doi.org/10.1177/35.11.3655323

Edén, U.M., Olson, L.W., & Barr, C. (1979). A simple device for staining many single-hole grids without individual manipulation. *Stain Technology, 54*(6), 345-347. https://doi.org/10.3109/10520297909110695

Forsdyke, J.B. (1979). A simple apparatus for staining and washing a batch of grids. *Journal of Microscopy, 117*(3), 437-440. https://doi.org/10.1111/j.1365-2818.1979.tb04701.x

Giddings, T.H. (2003). Freeze-substitution protocols for improved visualization of membranes in high-pressure frozen samples. *Journal of Microscopy, 212*(Pt 2), 53-61. https://doi.org/10.1046/j.1365-2818.2003.01228.x

Håkonsen, M.B., Grøthe, A.G., & Jørgensen, L. (1984). A simple device for staining electron microscopy grids. *Ultrastructural Pathology, 7*(4), 335-337. https://doi.org/10.3109/01913128409141493

Hess, M.W., Vogel, G.F., Yordanov, T.E., Witting, B., Gutleben, K., Ebner, H.L., de Araujo, M.E.G., Filipek, P.A., & Huber, L.A. (2018). Combining high-pressure freezing with pre-embedding immunogold electron microscopy and tomography. *Traffic, 19*(8), 639-649. https://doi.org/10.1111/tra.12575

Hopwood, D. Cell and tissue fixation, 1972-1982. (1985). *The Histochemical Journal, 17*(4), 389-442. https://doi.org/10.1007/bf01003203

Horowitz, R.A., & Woodcock, C.L. (1992). Alternative staining methods for Lowicryl sections. *The Journal of Histochemistry and Cytochemistry, 40*(1), 123-133. https://doi.org/10.1177/40.1.1370308

Jiménez, N., Vocking, K., van Donselaar, E.G., Humbel, B.M., Post, J.A., & Verkleij, A.J. (2009). Tannic acid-mediated osmium impregnation after freeze-substitution: a strategy to enhance membrane contrast for electron tomography. *Journal of Structural Biology, 166*(1), 103-106. https://doi.org/10.1016/j.jsb.2008.12.009

Johansen, J.P., Cain, C.K., Ostroff, L.E., & LeDoux, J.E. (2011). Molecular mechanisms of fear learning and memory. *Cell, 147*(3), 509-524. https://doi.org/10.1016/j.cell.2011.10.009

Jüngling, K., Lange, M.D., Szkudlarek, H.J., Lesting, J., Erdmann, F.S., Doengi, M., Kügler, S., & Pape, H.C. (2015). Increased GABAergic Efficacy of Central Amygdala Projections to Neuropeptide S Neurons in the Brainstem During Fear Memory Retrieval. *Neuropsychopharmacology, 40*(12), 2753-2763. https://doi.org/10.1038/npp.2015.125

Kasthuri, N., Hayworth, K.J., Berger, D.R., Schalek, R.L., Concello, J.A., Knowles-Barley, S., Lee, D., Vázquez-Reina, A., Kaynig, V., Jones, T.R., Roberts, M., Morgan, J.L., Tapia, J.C., Seung, H.S., Roncal, W.G., Vogelstein, J.T., Burns, R., Sussman, D.L., Priebe, C.E., … Lichtman, J.W. (2015). Saturated Reconstruction of a Volume of Neocortex. *Cell, 162*(3), 648-661. https://doi.org/10.1016/j.cell.2015.06.054

Kemppainen, S., & Pitkänen, A. (2000). Distribution of parvalbumin, calretinin, and calbindin-D(28k) immunoreactivity in the rat amygdaloid complex and colocalization with gamma-aminobutyric acid. *Journal of Comparative Neurology, 426*(3), 441-467. https://doi.org/10.1002/1096-9861(20001023)426:3%3C441::aid-cne8%3E3.0.co;2-7

Killingsworth, M.C., Lai, K., Wu, X., Yong, J.L., & Lee, C.S. (2012). Quantum dot immunocytochemical localization of somatostatin in somatostatinoma by Widefield Epifluorescence, super-resolution light, and immunoelectron microscopy. *Journal of Histochemistry & Cytochemistry, 60*(11), 832-843. https://doi.org/10.1369/0022155412459856

Kneissler, U., Harendza, S., & Helmchen, U. (2003). Support film in transmission electron microscopy: experiences with polyvinyl butyral Pioloform BM 18. *Journal of Electron Microscopy, 52*(3), 355-357. https://doi.org/10.1093/jmicro/52.3.355

Kocorowski, L.H., & Helmstetter, F.J. (2001). Calcitonin gene-related peptide released within the amygdala is involved in Pavlovian auditory fear conditioning. *Neurobiology of Learning and Memory, 75*(2), 149-163. https://doi.org/10.1006/nlme.2000.3963

Krabbe, S., Gründemann, J., & Lüthi, A. (2018). Amygdala Inhibitory Circuits Regulate Associative Fear Conditioning. *Biological Psychiatry, 83*(10), 800-809. https://doi.org/10.1016/j.biopsych.2017.10.006

LeDoux, J.E. (2000). Emotion circuits in the brain. *Annual review of neuroscience, 23*, 155-184. https://doi.org/10.1146/annurev.neuro.23.1.155

LeDoux, J.E., Farb, C.R., & Milner, T.A. (1991). Ultrastructure and synaptic associations of auditory thalamo-amygdala projections in the rat. *Experimental Brain Research, 85*(3), 577-586. https://doi.org/10.1007/bf00231742

LeDoux, J.E., Farb, C.R., & Ruggiero, D.A. (1990). Topographic organization of neurons in the acoustic thalamus that project to the amygdala. *Journal of Neuroscience, 10*(4), 1043-1054. https://dx.doi.org/10.1523%2FJNEUROSCI.10-04-01043.1990

Linke, R., Braune, G., & Schwegler, H. (2000). Differential projection of the posterior paralaminar thalamic nuclei to the amygdaloid complex in the rat. *Experimental Brain Research, 134*(4), 520-532. https://doi.org/10.1007/s002210000475

Linke, R., & Schwegler, H. (2000). Convergent and complementary projections of the caudal paralaminar thalamic nuclei to rat temporal and insular cortex. *Cerebral Cortex, 10*(8), 753-771. https://doi.org/10.1093/cercor/10.8.753

Lu, Y.C., Chen, Y.Z., Wei, Y.Y., He, X.T., Li, X., Hu, W., Yanagawa, Y., Wang, W., Wu, S.X., & Dong, Y.L. (2015). Neurochemical properties of the synapses between the parabrachial nucleus-derived CGRP-positive axonal terminals and the GABAergic neurons in the lateral capsular division of central nucleus of amygdala. *Molecular Neurobiology, 51*(1), 105-118. https://doi.org/10.1007/s12035-014-8713-x

Maren, S. (2001). Neurobiology of Pavlovian fear conditioning. *Annual Review of Neuroscience, 24*, 897-931. https://doi.org/10.1146/annurev.neuro.24.1.897

Markram, H. (2006). The blue brain project. *Nature Reviews of Neuroscience, 7*(2), 153-60. https://doi.org/10.1038/nrn1848

Markram, H., Muller, E., Ramaswamy, S., Reimann, M.W., Abdellah, M., Sanchez, C.A., Ailamaki, A., Alonso-Nanclares, L., Antille, N., Arsever, S., Kahou, G.A., Berger, T.K., Bilgili, A., Buncic, N., Chalimourda, A., Chindemi, G., Courcol, J.D., Delalondre, F., Delattre, V., … Schürmann, F. (2015). Reconstruction and Simulation of Neocortical Microcircuitry. *Cell, 163*(2), 456-492. https://doi.org/10.1016/j.cell.2015.09.029

Mascagni, F., & McDonald, A.J. (2003). Immunohistochemical characterization of cholecystokinin containing neurons in the rat basolateral amygdala. *Brain Research, 976*(2), 171-184. https://doi.org/10.1016/s0006-8993(03)02625-8

McDonald, A.J. (1982)a. Cytoarchitecture of the central amygdaloid nucleus of the rat. *Journal of Comparative Neurology, 208*(4), 401-418. https://doi.org/10.1002/cne.902080409

McDonald, A.J. (1982)b. Neurons of the lateral and basolateral amygdaloid nuclei: a Golgi study in the rat. *Journal of Comparative Neurology, 212*(3), 293-312. https://doi.org/10.1002/cne.902120307

McDonald, A.J. (1985). Morphology of peptide-containing neurons in the rat basolateral amygdaloid nucleus. *Brain Research, 338*(1), 186-191. https://doi.org/10.1016/0006-8993(85)90266-5

McDonald, A.J. (1989). Coexistence of somatostatin with neuropeptide Y, but not with cholecystokinin or vasoactive intestinal peptide, in neurons of the rat amygdala. *Brain Research, 500*(1-2), 37-45. https://doi.org/10.1016/0006-8993(89)90297-7

McDonald, A.J. (1997). Calbindin-D28k immunoreactivity in the rat amygdala. *Journal of Comparative Neurology, 383*(2), 231-244. https://doi.org/10.1002/(SICI)1096-9861(19970630)383:2%3C231::AID-CNE9%3E3.0.CO;2-1

McDonald, A.J., & Mascagni, F. (2001). Colocalization of calcium-binding proteins and GABA in neurons of the rat basolateral amygdala. *Neuroscience, 105*(3), 681-693. https://doi.org/10.1016/s0306-4522(01)00214-7

McDonald, A.J., & Mascagni, F. (2002). Immunohistochemical characterization of somatostatin containing interneurons in the rat basolateral amygdala. *Brain Research, 943*(2), 237-244. https://doi.org/10.1016/S0006-8993(02)02650-1

McDonald, A.J., & Mascagni, F. (2004). Parvalbumin-containing interneurons in the basolateral amygdala express high levels of the alpha1 subunit of the GABAA receptor. *Journal of Comparative Neurology, 473*(1), 137-146. https://doi.org/10.1002/cne.20101

McDonald, A.J., Mascagni, F., & Augustine, J.R. (1995). Neuropeptide Y and somatostatin-like immunoreactivity in neurons of the monkey amygdala. *Neuroscience, 66*(4), 959-982. https://doi.org/10.1016/0306-4522(94)00629-j

McDonald, A.J., Muller, J.F., & Mascagni, F. (2011). Postsynaptic targets of GABAergic basal forebrain projections to the basolateral amygdala. *Neuroscience, 183*, 144-159. https://doi.org/10.1016/j.neuroscience.2011.03.027

McDonald, A.J., & Pearson, J.C. (1989). Coexistence of GABA and peptide immunoreactivity in non-pyramidal neurons of the basolateral amygdala. *Neuroscience Letters, 100*(1-3), 53-58. https://doi.org/10.1016/0304-3940(89)90659-9

McDonald, A.J., & Zaric, V. (2015a). Extrinsic origins of the somatostatin and neuropeptide Y innervation of the rat basolateral amygdala. *Neuroscience, 294*, 82-100. https://doi.org/10.1016/j.neuroscience.2015.03.004

McDonald, A.J., & Zaric, V. (2015b). GABAergic somatostatin-immunoreactive neurons in the amygdala project to the entorhinal cortex. *Neuroscience, 290*(227-242). https://doi.org/10.1016/j.neuroscience.2015.01.028

McDonald, K. (1999). High-pressure freezing for preservation of high resolution fine structure and antigenicity for immunolabeling. *Methods in Molecular Biology, 117*, 77-97. https://doi.org/10.1385/1-59259-201-5:77

McDonald, K.L. (2014). Rapid embedding methods into epoxy and LR White resins for morphological and immunological analysis of cryofixed biological specimens. *Microscopy and Microanalysis, 20*(1), 152-163. https://doi.org/10.1017/S1431927613013846

McDonald, K., Schwarz, H., Müller-Reichert, T., Webb, R., Buser, C., & Morphew, M. (2010). "Tips and tricks" for high-pressure freezing of model systems. *Methods in Cell Biology, 96*, 671-693. https://doi.org/10.1016/S0091-679X(10)96028-7

McDonald, K.L., & Webb, R.I. (2011). Freeze substitution in 3 hours or less. *Journal of Microscopy, 243*(3), 227-233. https://doi.org/10.1111/j.1365-2818.2011.03526.x

Meredith, G.E., & Wouterlood, F.G. (1993). Identification of synaptic interactions of intracellularly injected neurons in fixed brain slices by means of dual-label electron microscopy. *Microscopy Research and Technique, 24*(1), 31-42. https://doi.org/10.1002/jemt.1070240105

Moreno-Ruiz, P., Wik Leiss, L., Mezheyeuski, A., & Ehnman, M. (2019). Double Immunohistochemistry and Digital Image Analysis. *Methods in Molecular Biology, 1913*, 3-11. https://doi.org/10.1007/978-1-4939-8979-9_1

Morphew, M., He, W., Bjorkman, P.J., McIntosh, J.R. (2008). Silver enhancement of Nanogold particles during freeze substitution for electron microscopy. *Journal of Microscopy, 230*(Pt 2), 263-267. https://doi.org/10.1111/j.1365-2818.2008.01983.x

Muller, J.F., Mascagni, F., & McDonald, A.J. (2007). Postsynaptic targets of somatostatin-containing interneurons in the rat basolateral amygdala. *Journal of Comparative Neurology, 500*(3), 513-529. https://doi.org/10.1002/cne.21185

Neugebauer, V., Mazzitelli, M., Cragg, B., Ji, G., Navratilova, E., & Porreca, F. (2020). Amygdala, neuropeptides, and chronic pain-related affective behaviors. *Neuropharmacology, 170*. https://doi.org/10.1016/j.neuropharm.2020.108052

Nisman, R., Dellaire, G., Ren, Y., Li, R., & Bazett-Jones, D.P. (2004). Application of quantum dots as probes for correlative fluorescence, conventional, and energy-filtered transmission electron microscopy. *The Journal of Histochemistry and Cytochemistry, 52*(1), 13-18. https://doi.org/10.1177/002215540405200102

Ota, K.T., Monsey, M.S., Wu, M.S., & Schafe, G.E. (2010). Synaptic plasticity and NO-cGMP-PKG signaling regulate pre- and postsynaptic alterations at rat lateral amygdala synapses following fear conditioning. *PLoS One, 5*(6), e11236. https://doi.org/10.1371/journal.pone.0011236

Parani, S., Pandian, K., & Oluwafemi, O.S. (2018). Gelatin stabilization of quantum dots for improved stability and biocompatibility. *International Journal of Biological Macromolecules, 107*(Pt A), 635-641). https://doi.org/10.1016/j.ijbiomac.2017.09.039

Pease, D.C., & Porter, K.R. (1981). Electron microscopy and ultramicrotomy. *The Journal of Cell Biology, 91*(3 Pt 2), 287s-292s. https://doi.org/10.1083/jcb.91.3.287s

Pelletier, G., Guy, J., Allen, Y.S., & Polak, J.M. (1984). Electron microscope immunocytochemical localization of neuropeptide Y (NPY) in the rat brain. *Neuropeptides, 4*(4), 319-324. https://doi.org/10.1016/0143-4179(84)90006-4

Peng, Q., Zhang, M., Richter, H.P., & Bock, R. (1993). A new technique for post-embedding immunogold localization of vasopressin in the rat median eminence. *Acta Histochemica, 95*(1), 75-78. https://doi.org/10.1016/S0065-1281(11)80392-2

Pieri, L., Sassoli, C., Romagnoli, P., & Domenici, L. (2002). Use of periodate-lysine-paraformaldehyde for the fixation of multiple antigens in human skin biopsies. *European Journal of Histochemistry, 46*(4), 365-375. https://doi.org/10.4081/1749

Pirozzi, N.M., Hoogenboom, J.P., & Giepmans, B.N.G. (2018). ColorEM: analytical electron microscopy for element-guided identification and imaging of the building blocks of life. *Histochemistry and Cell Biology, 150*(5), 509-520. https://doi.org/10.1007/s00418-018-1707-4

Regev, A., Teichmann, S.A., Lander, E.S., Amit, I., Benoist, C., Birney, E., Bodenmiller, B., Campbell, P., Carninci, P., Clatworthy, M., Clevers, H., Deplancke, B., Dunham, I., Eberwine, J., Eils, R., Enard, W., Farmer, A., Fugger, L., Göttgens, B., … Yosef, N. (2017). The Human Cell Atlas. *Elife, 6*(e27041). https://doi.org/10.7554/eLife.27041

Roberts, G.W., Woodhams, P.L., Polak, J.M., & Crow, T.J. (1982). Distribution of neuropeptides in the limbic system of the rat: the amygdaloid complex. *Neuroscience, 7*(1), 99-131. https://doi.org/10.1016/0306-4522(82)90156-7

Rogan, M.T., Stäubli, U.V., & LeDoux, J.E. (1997). Fear conditioning induces associative long-term potentiation in the amygdala. *Nature, 390*(6660), 604-607. https://doi.org/10.1038/37601

Roholl, P.J., Leene, W., Kapsenberg, M.L., & Vos, J.G. (1981). The use of tannic acid fixation for the electron microscope visualization of fluorochrome-labelled antibodies attached to cell surface antigens. *Journal of Immunological Methods, 42*(3), 285-289. https://doi.org/10.1016/0022-1759(81)90157-5

Rostkowski, A.B., Teppen, T.L., Peterson, D.A., & Urban, J.H. (2009). Cell-specific expression of neuropeptide Y Y1 receptor immunoreactivity in the rat basolateral amygdala. *Journal of Comparative Neurology, 517*(2), 166-176. https://doi.org/10.1002/cne.22143

Rovira-Esteban, L., Gunduz-Cinar, O., Bukalo, O., Limoges, A., Brockway, E., Müller, K., Fenmo, L., Kim, Y.S., Ramakrishnan, C., Andrási, T., Deisseroth, K., Holmes, A., & Hájos, N. (2019). Excitation of Diverse Classes of Cholecystokinin Interneurons in the Basal Amygdala Facilitates Fear Extinction. *eNeuro, 6*(6). https://doi.org/10.1523/ENEURO.0220-19.2019

Równiak, M., Kolenkiewicz, M., & Kozłowska, A. (2017). Parvalbumin, but not calretinin, neurons express high levels of α1-containing $GABA_A$ receptors, α7-containing nicotinic acetylcholine receptors and D2-dopamine receptors in the basolateral amygdala of the rat. *Journal of Chemical Neuroanatomy, 86*, 41-51. https://doi.org/10.1016/j.jchemneu.2017.08.002

Schafe, G.E., & LeDoux, J.E. (2000). Memory consolidation of auditory pavlovian fear conditioning requires protein synthesis and protein kinase A in the amygdala. *Journal of Neuroscience, 20*(18). https://doi.org/10.1523/JNEUROSCI.20-18-j0003.2000

Schwarz, H., & Humbel, B.M. (1989). Influence of fixatives and embedding media on immunolabelling of freeze-substituted cells. *Scanning Microscopy Supplement, 3*, 57-64.

Scotuzzi, M., Kuipers, J., Wensveen, D.I., de Boer, P., Hagen, K.C., Hoogenboom, J.P., & Giepmans, B.N. Multi-color electron microscopy by element-guided identification of cells, organelles, and molecules. *Scientific Reports, 7*, 45970. https://doi.org/10.1038/srep45970

Shahidi, R., Williams, E.A., Conzelmann, M., Asadulina, A., Verasztó, C., Jasek, S., Bezares-Calderón, L.A., & Jékely, G. (2015). A serial multiplex immunogold labeling method for identifying peptidergic neurons in connectomes. *Elife, 4*. https://doi.org/10.7554/eLife.11147

Shi, H.B., Zhou, Z.B., & Wu, Z.B. (1990). A highly efficient method for staining ultrathin sections. *Journal of Tongji Medical University, 10*(2), 88-90. https://doi.org/10.1007/bf02887867

Somogyi, P., & Takagi, H. (1982). A note on the use of picric acid-paraformaldehyde-glutaraldehyde fixative for correlated light and electron microscopic immunocytochemistry. *Neuroscience, 7*(7), 1779-1783. https://doi.org/10.1016/0306-4522(82)90035-5

Steinbrecht, R.A. (1993). Freeze-Substitution for Morphological and Immunocytochemical Studies in Insects. *Microscopy Research and Technique, 24*(6), 488-504. https://doi.org/10.1002/jemt.1070240605

Szymanski, C.J., Yi, H., Liu, J.L., Wright, E.R., & Payne, C.K. (2013). Imaging intracellular quantum dots: fluorescence microscopy and transmission electron microscopy. *Methods in Molecular Biology, 1026*, 21-33. https://doi.org/10.1007/978-1-62703-468-5_2

Tasan, R.O., Verma, D., Wood, J., Lach, G., Hörmer, B., de Lima, T.C.M., Herzog, H., & Sperk, G. (2016). The role of Neuropeptide Y in fear conditioning and extinction. *Neuropeptides, 55,* 111-126. https://doi.org/10.1016/j.npep.2015.09.007

Thijssen, M.H., Van Went, J.L., & Van Aelst, A.C. (1998). Heptane and isooctane as embedding fluids for high-pressure freezing of *Petunia* ovules followed by freeze-substitution. *Journal of Microscopy, 192*(Pt 3), 228-235.

Unal, G., Paré, J.F., Smith, Y., & Paré, D. (2014). Cortical inputs innervate calbindin-immunoreactive interneurons of the rat basolateral amygdaloid complex. *Journal of Comparative Neurology, 522*(8), 1915-1928. https://doi.org/10.1002/cne.23511

Walther, P., & Ziegler, A. (2002). Freeze substitution of high-pressure frozen samples: the visibility of biological membranes is improved when the substitution medium contains water. *Journal of Microscopy, 208*(Pt 1), 3-10. https://doi.org/10.1046/j.1365-2818.2002.01064.x

Wild, P., Schraner, E.M., Adler, H., & Humbel, B.M. (2001). Enhanced resolution of membranes in cultured cells by cryoimmobilization and freeze-substitution. *Microscopy Research and Techniques, 53*(4), 313-321. https://doi.org/10.1002/jemt.1098

Wood, J., Verma, D., Lach, G., Bonaventure, P., Herzog, H., Sperk, G., & Tasan, R.O. (2016). Structure and function of the amygdaloid NPY system: NPY Y2 receptors regulate excitatory and inhibitory

synaptic transmission in the centromedial amygdala. *Brain Structure and Function, 221*(7), 3373-3391. https://doi.org/10.1007/s00429-015-1107-7

Woodson, W., Farb, C.R., & Ledoux, J.E. (2000). Afferents from the auditory thalamus synapse on inhibitory interneurons in the lateral nucleus of the amygdala. *Synapse, 38*(2), 124-137. https://doi.org/10.1002/1098-2396(200011)38:2%3C124::AID-SYN3%3E3.0.CO;2-N

Wolff, S.B., Gründemann, J., Tovote, P., Krabbe, S., Jacobson, G.A., Müller, C., Herry, C., Ehrlich, I., Friedrich, R.W., Letzkus, J.J., & Lüthi, A. (2014). Amygdala interneuron subtypes control fear learning through disinhibition. *Nature, 509*(7501), 453-458. https://doi.org/10.1038/nature13258

Yamashita, S., Katsumata, O., & Okada, Y. (2009). Establishment of a standardized post-embedding method for immunoelectron microscopy by applying heat-induced antigen retrieval. *Journal of Electron Microscopy, 58*(4), 267-279. https://doi.org/10.1093/jmicro/dfp017

Yamashita, S., & Okada, Y. (2014). Heat-induced Antigen Retrieval in Conventionally Processed Epon-embedded Specimens: Procedures and Mechanisms. *The Journal of Histochemistry and Cytochemistry, 62*(8), 584-597. https://doi.org/10.1369/0022155414537899

Yasui, Y., Saper, C.B., & Cechetto, D.F. (1991). Calcitonin gene-related peptide (CGRP) immunoreactive projections from the thalamus to the striatum and amygdala in the rat. *Journal of Comparative Neurology, 308*(2), 293-310. https://doi.org/10.1002/cne.903080212